DISS. ETH NO. 29008

The Dynamical Tropopause Location as a Predictor for North Atlantic Tropical Cyclone Activity

A thesis submitted to attain the degree of

DOCTOR OF SCIENCES of ETH ZURICH

(Dr. sc. ETH Zurich)

presented by
BERNHARD ENZ
MSc ETH in Atmospheric and Climate Science
born on 29 November 1992
citizen of Switzerland

accepted on the recommendation of

Prof. Dr. Ulrike Lohmann, examiner
Dr. Michael Sprenger, co-examiner
Prof. Dr. Sarah Jones, co-examiner

2023

Abstract

Tropical cyclones are violent weather systems that can cause great damage to coastlines. Their successful prediction, on timescales ranging from a few days to the climate scale, has thus been a subject of scientific research for several decades. For the North Atlantic basin, seasonal and subseasonal forecasts are operationally produced by various agencies to aid in estimating the potential for damage caused throughout the season. The 2013 hurricane season was predicted to be above average in activity. In reality, only two category 1 hurricanes, and no major hurricane, occurred, which is far below average. Predictions of the total number of tropical cyclones were generally correct, which suggests that the intensification of tropical cyclones was impeded. It has since been argued that an abundance of Rossby wave breaking events in the North Atlantic basin caused an increase in vertical wind shear and a reduction in mid-tropospheric humidity, which would militate against intensification. Rossby wave breaking event frequency, along with other related metrics, has therefore been proposed as a predictor for tropical cyclone activity. This thesis explores the latitudinal position of the tropopause in the western North Atlantic region, which is intrinsically linked to Rossby wave breaking events, as a simplified and more powerful predictor for tropical cyclone activity.

The implementation of the tropopause latitude in predictions requires the use of numerical models. To assess whether the relation between the tropopause latitude and tropical cyclone activity is represented properly, tropical cyclones must be tracked. A tracking algorithm was thus developed for use with the ICON model. The tracking algorithm uses varying parameter thresholds to detect weaker systems and the comparatively weak tail ends of tropical cyclone tracks. It is shown that the algorithm can detect tropical cyclones during their formation stage, and can terminate them as they dissipate or transition into extratropical systems. False positives and other tracking issues are shown to not significantly impact the representation of the accumulated cyclone energy throughout a season. The tracking algorithm is thus capable of extracting full tropical cyclone tracks from the data, and adequately reflects tropical cyclone activity.

1980 to 2017 reanalysis data have been used in conjunction with observed tropical cyclone data to show strong correlation between the tropopause latitude on the 360 K isentropic surface in the western North Atlantic region and the accumulated cyclone energy throughout a hurricane season. The strong correlation is argued to be due to reduced vertical wind shear, and thus reduced ventilation of tropical cyclone inner cores, for more poleward tropopause positions. The tropopause location is also shown to be linked to changes in the genesis location, landfalling probability, and lifetime of tropical cyclones. The tropopause location thus shows strong potential to be of use as a predictor of tropical cyclone activity on a seasonal timescale.

The regional variant of the ICON atmosphere model has been used to produce ensemble simulations for the month of September in the years 1980 to 2021, with the aim of reproducing the results found in reanalysis and observational data. The simulations underestimate North Atlantic tropical cyclone activity and place the mean tropopause latitude on the 360 K isentropic surface slightly too far equatorwards. However, the simulations succeed in reproducing the link between September mean tropopause latitude in the western North Atlantic region and September accumulated cyclone energy in the North Atlantic basin.

This thesis demonstrates that the September mean tropopause latitude in the western North Atlantic region is linked to tropical cyclone activity on a seasonal and subseasonal scale, both in observational and reanalysis data as well as in numerical simulation data. The tropopause latitude shows potential for use as a predictor in seasonal tropical cyclone forecasting.

Zusammenfassung

Tropische Zyklonen sind gewaltige Wettersysteme die grossen Schaden in Küstengebieten verursachen können. Ihre erfolgreiche Vorhersage, auf Zeitskalen von ein paar Tagen bis zum Klima, ist daher seit mehreren Jahrzehnten ein Subjekt der wissenschaftlichen Forschung. Für das Nordatlantische Becken werden von verschiedenen Stellen saisonale und subsaisonale Vorhersagen operationell produziert, um Abschätzungen des Schadenspotentials innerhalb der Saison zu unterstützen. Die Hurrikan Saison 2013 wurde als überdurchschnittlich aktiv vorhergesagt. In der Realität traten nur zwei Kategorie 1 Hurrikane, und kein Hurrikan der Kategorie 3 oder höher, auf, was weit unter dem Durchschnitt liegt. Vorhersagen für die Anzahl an tropischen Zyklonen waren generell korrekt, was darauf hindeutet, dass die Intensivierung der tropischen Zyklonen beeinträchtigt war. Seither wurde argumentiert, dass ein Überfluss an brechenden Rossby Wellen im Nordatlantik eine Erhöhung der vertikalen Windscherung und eine Reduktion der Mitteltroposphärischen Feuchte bewirkte, was die Intensivierung beeinträchtigt. Die Häufigkeit von brechenden Rossby Wellen, zusammen mit verwandten Metriken, wurden daher als Prädiktoren für die Aktivität von tropischen Zyklonen vorgeschlagen. Diese Arbeit erkundet den Breitengrad der Position der Tropopause in der Region des westlichen Nordatlantik, welche intrinsisch mit brechenden Rossby Wellen zusammenhängt, als vereinfachten und mächtigeren Prädiktor für die Aktivität von tropischen Zyklonen.

Die Implementierung des Breitengrades der Tropopause benötigt den Einsatz von numerischen Modellen. Um abzuschätzen, ob der Zusammenhang zwischen dem Breitengrad der Tropopause und der Aktivität von tropischen Zyklonen angemessen repräsentiert wird, müssen tropische Zyklonen und ihre Zugbahnen identifiziert werden. Ein entsprechender Algorithmus für den Gebrauch mit dem ICON Modell wurde daher entwickelt. Der Algorithmus benutzt variierende Parameterschwellenwerte, um schwächere Systeme und vergleichsweise schwache Endstücke von Zugbahnen der tropischen Zyklonen zu detektieren. Es wird gezeigt, dass der Algorithmus tropische Zyklonen in ihrem Formationsstadium detektieren kann, und sie, wenn sie sich auflösen oder in extratropische Zyklonen umwandeln, beenden kann. Es wird gezeigt, dass fehlerhafte Identifikation und andere Probleme keinen signifikanten Einfluss auf die Repräsentation der saisonalen akkumulierten Zyklonenenergie hat. Der Algorithmus ist daher dazu fähig, ganzheitliche Zugbahnen von tropischen Zyklonen aus den Daten zu extrahieren, und reflektiert die Aktivität der tropischen Zyklonen adäquat.

Reanalysedaten für die Jahre 1980 bis 2017 wurden zusammen mit Beobachtungsdaten verwendet, um eine starke Korrelation zwischen dem Breitengrad der Tropopause auf der 360 K isentropen Fläche im westlichen Nordatlantik und der akkumulierten Zyklonenenergie während einer Hurrikansaison aufzuzeigen. Es wird argumentiert, dass die starke Korrelation eine Folge von reduzierter Windscherung, und dadurch reduzierter Ventilation der inneren Kernregion von tropischen Zyklonen, bei Polnäheren Positionen der Tropopause ist. Ebenfalls wird gezeigt, dass die Position der Tropopause mit Änderungen des Entstehungsorts, der Wahrscheinlichkeit eines Landfalls und der Lebensdauer von tropischen Zyklonen verbunden ist. Die Position der Tropopause weist daher starkes Potenzial als Prädiktor für die Aktivität von tropischen Zyklonen auf einer saisonalen Zeitskala auf.

Die regionale Variante des ICON Atmosphärenmodells wurde benutzt, um Ensemblesimulationen für den September in den Jahren 1980 bis 2021 zu produzieren, mit der Absicht, die Resultate welche in Reanalyse- und Beobachtungsdaten gefunden wurden, zu reproduzieren. Die Simulationen unterschätzen die Aktivität der Nordatlantischen tropischen Zyklonen, und

platzieren den mittleren Breitengrad der Tropopause auf der 360 K isentropen Fläche etwas zu weit äquatorwärts. Die Simulationen reproduzieren jedoch erfolgreich die Verbindung zwischen dem mittleren Breitengrad der Tropopause im September, und der akkumulierten Zyklonenenergie im September im Nordatlantischen Becken.

Die vorliegende Arbeit demonstriert, dass der mittlere Breitengrad der Tropopause i der westlichen Nordatlantik Region im September mit der akkumulierten Zyklonenenergie verbunden ist, auf einer saisonalen und subsaisonalen Skala, und ich Reanalyse- und Beobachtungsdaten, sowie in numerisch simulierten Daten. Der Breitengrad der Tropopause weist Potenzial für den Gebrauch als Prädiktor in saisonalen Vorhersagen von tropischen Zyklonen auf.

Acknowledgments

I would like to thank all of my supervisors, both past and present, for their support and their belief in my ability to complete this thesis. Ulrike Lohmann, you have my deepest gratitude for mentoring me since my Bachelor's thesis in 2015, for not simply showing me the door during prolonged stretches of near zero productivity, and for, at times seemingly miraculously, believing that I am capable. Naturally, I would also like to apologize for not being the best student. My past supervisors, Tanja Stanelle and David Neubauer, I thank you for your valuable input and aid, which has helped me immensely. Michael Sprenger, I thank you not only for your valuable input, especially concerning atmospheric dynamics, but also for agreeing to be both my secondary advisor and the co-examiner at my defense very shortly before the end. Further, I thank Sarah Jones for being the external co-examiner of my defense, and Niki Gruber for chairing the defense.

The Wolke group in its entirety is, of course, deserving of my gratitude as well. Even though my topic is exotic here, I still receive valuable feedback, and have fruitful discussions. In particular, I would like to thank Nadia for explaining thermodynamics to me and for the drawing of Big Floofer, Nadja for sharing my frustration, Judith for convincing me to never plot anything without asking her about it first, Little Ulrike for motivating me to not work from home but from the office, David for talking about mental health, Colin for peer reviewing my dumb jokes, Zane for our discussions, both of scientific nature and not, and Rob for being an inspiration to me ever since he taught me about thunderstorms.

Sylvaine and Colombe, I am convinced that you are secretly techno-wizards. I thank you for your sorcery with ICON and NICAM, and somehow making the machines do what I need them to do. Without your help, I would be doing my modeling work by hand.

I would like to further thank Atsumu Ohmura, Ayako Abe-Ouchi and Masaki Satoh for their support in my literal journeys to distant lands, and figurative journey to improve my understanding of the atmosphere.

I wish to thank my family for their continued support. I thank my mother, Anna, as I maintain her first name is, for calling me every week to make sure that I eat real food, and my father, Werner, for inspiring me to become a doctor when I was still a small child, though I had medicine in mind at the time. Fortunately, pursuing a PhD in sciences technically still counts as an attempt to become a doctor, no matter what my 5-year old self has to say about the matter. I also thank my brothers Michael, Christoph, Lukas and Dominik for helping me develop into who I am now.

Contents

Chapter 1

Introduction

> "The tropical cyclone is a solitary creature of the tropical oceans accompanied by violent rotating winds and torrential rain."
>
> *(Ooyama, 1969)*

1.1 Tropical Cyclones

Tropical cyclones (TCs) are extreme weather systems originating over the tropical oceans (Gray, 1968). They are characterized by strong winds, spiraling rainbands, a warm core in the upper troposphere, an immense, outward-sloping cloud where the most intense winds are located, called the eyewall, and a central eye. The primary, cyclonic rotation of the system is maintained by the release of latent heat in the eyewall cloud. Ooyama (1969), using a numerical model, concluded that the source of this latent heat is the evaporation of warm ocean water into the planetary boundary layer, where the inflow carries it towards the eyewall. Emanuel (1986) proposed a model that explains TCs as a Carnot heat engine, where latent and sensible heat is gained from the ocean at the temperature of the planetary boundary layer, and ejected in the outflow near the tropopause at a temperature about 100 K colder than the surface. Rotunno and Emanuel (1987) then used this model to argue that surface fluxes can amplify an initial vortex even in the absence of an initial conditional instability, underlining the importance of boundary layer processes to TC intensification. TCs are therefore weather systems that extract energy from the tropical surface waters and move it upwards, and due to their motion also polewards.

A satellite image of hurricane Gilbert (1988) is shown in fig. 1.1. Gilbert is located south of Cuba, and has a clearly visible eye. The spiraling rainbands extending from the central cloud structure indicate the cyclonic rotation of the system. The secondary circulation is shown in fig. 1.2. The inflow within the boundary layer is roughly isothermal, as the ocean water has a heat capacity far exceeding that of the air above it, and is thus able to maintain the air temperature. Due to the evaporation of ocean water, the equivalent potential temperature increases towards the center. The higher the equivalent potential temperature becomes in the boundary layer, the higher the altitude of the outflow will be, as this determines at which height the ascending air becomes neutrally buoyant. The temperature difference between the surface and the outflow determines the efficiency of the Carnot cycle. Finally, the air subsides far away from the center, and can be reintroduced into the inflow, completing the cycle. The warm core is indicated by the strong increase of equivalent potential temperature towards the center.

1.1.1 Tropical Cyclogenesis

The genesis of a tropical cyclone is an event that requires a perfect storm of prerequisites. While not all prerequisites must be fulfilled for a TC to form, the likelihood of cyclogenesis is reduced

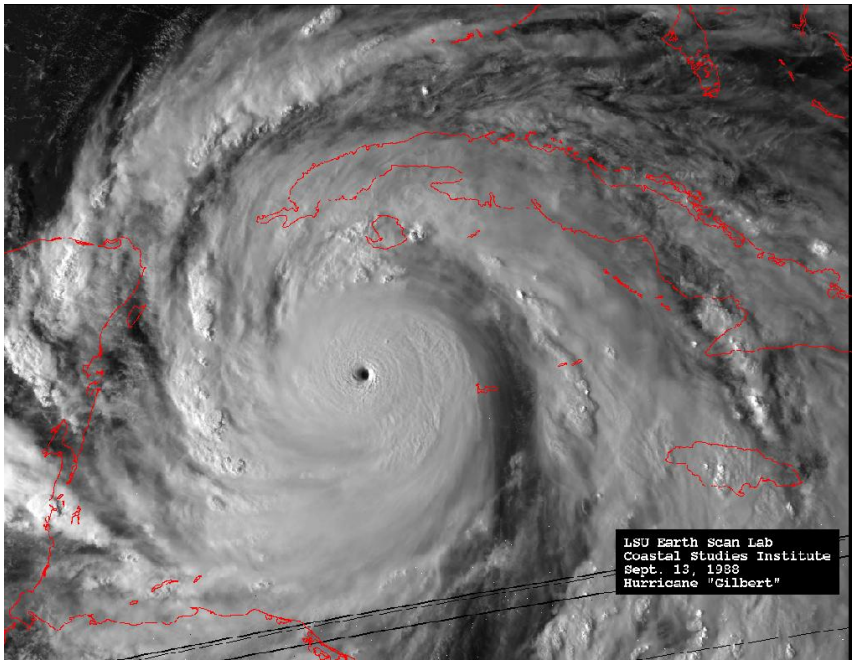

Figure 1.1: Satellite image of hurricane Gilbert (1988). Image downloaded from https://www.nhc.noaa.gov/outreach/history/ at 21:15 UTC on 17.11.2022

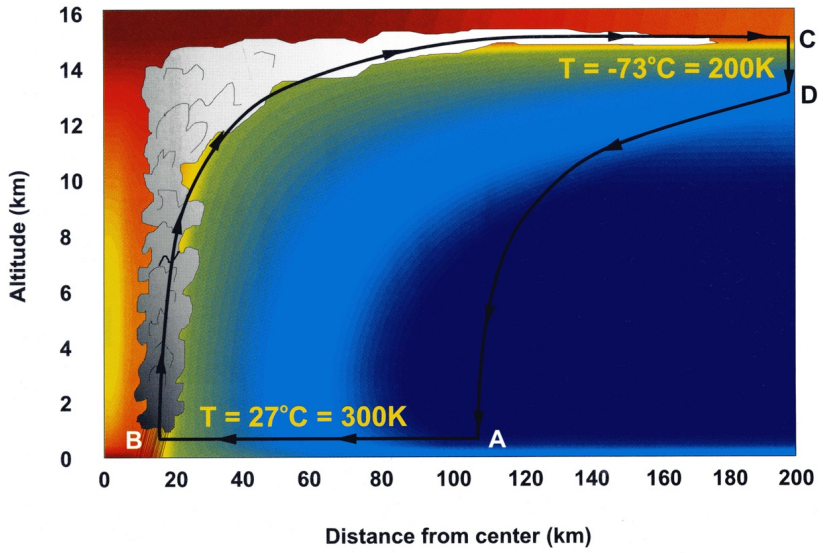

Figure 1.2: Figure 10.2 of Emanuel (2005), showing a schematic of an azimuthal mean TC, indicating the secondary circulation (black arrows) with typical inflow and outflow temperature values. Contours indicate equivalent potential temperature.

if this is the case.

Palmen (1948) recognized that for a tropical cyclone to form, there must be some vertical vorticity present. This pre-existing vorticity consists of a combination of vorticity relative to the planet's rotation (i.e. relative vertical vorticity, ζ), and vorticity due to the rotation of the planet (i.e. planetary vertical vorticity, commonly described by the Coriolis parameter f). For this reason, Palmen (1948) finds that tropical cyclones typically do not form within 5° latitude of the equator. However, being some distance away from the equator does not guarantee sufficient vorticity. In the North Atlantic basin, the majority of tropical cyclones form in a trough of an African easterly wave (AEW) (Pasch et al., 1998), which is characterized by a low pressure anomaly and cyclonic rotation.

As also noted by Palmen (1948), tropical cyclones require some vertical instability to form. This requires a warm sea surface temperature (SST), and Palmen (1948) gives a minimum value of 26 to 27 °C. McTaggart-Cowan et al. (2015) revisited this threshold, and argued that tropical cyclones forming by tropical transition, i.e. from an extratropical precursor cyclone that develops the structure of a tropical cyclone (Davis and Bosart, 2004), can form at lower SSTs. They go on to state that while for TCs not developing by tropical transition a 26.5 °C SST threshold can be used, this should be combined with a measure for static stability to better describe the potential for tropical cyclogenesis by tropical transition.

While SST is relevant for vertical stability, it is also indicative of ocean thermal energy. From

$$F_{q_v} = C_E |\mathbf{V}| \left(q_s - q_v\right) \tag{1.1}$$

where F_{q_v} is the surface latent heat flux, C_E is a transfer coefficient, $|\mathbf{V}|$ is the magnitude of the wind with the bold font denoting a vector, q_s is the saturation specific humidity and q_v is the specific humidity, it can be seen that a higher SST, and thus a higher temperature of the directly adjacent air and a resulting higher q_s, causes a higher latent heat flux into the atmosphere at a given wind speed. More energy is thus extracted from a warmer ocean. As tropical cyclones induce ocean mixing, and a high SST is highly favorable to tropical cyclogenesis, high temperatures should be present to a depth of 60 meters (Gray, 1975). Otherwise, cold water stirred up from beneath the surface can impede the latent heat transfer into the atmosphere.

Convection is a central element to the genesis of a tropical cyclone. This process uses the latent heat gained from the evaporation of ocean surface water to heat a convective column. However, this heating is reduced by entrainment of environmental air (Emanuel et al., 2004). Environmental air is more dense than convectively ascending air, either by being colder, being dryer, or as is typically the case, being both colder and dryer. Therefore, mixing environmental air into the updraft will reduce the density difference, and convection is hindered. Further, if the entrained air is sufficiently dry or a sufficient amount is entrained, evaporation of cloud hydrometeors can occur. This cools the updraft, making it more dense. To reduce the detrimental effect of entrainment, a humid mid-troposphere is required for tropical cyclogenesis. Gray (1975) finds that an environmental relative humidity below 40% is the least conducive to tropical cyclogenesis, while values above 70% seem to have no additional benefit to the likelihood of tropical cyclogenesis.

The magnitude of entrainment heavily depends on vertical wind shear (Tang and Emanuel, 2010), and the combined effect of vertical wind shear and environmental humidity can be quantified by the ventilation index (VI) of Tang and Emanuel (2012). The ventilation index is defined as

$$VI = \frac{VWS \cdot \chi_m}{u_{PI}} \tag{1.2}$$

where u_{PI} is the potential intensity as defined by Bister and Emanuel (2002), and χ_m is the entropy deficit, defined as:

$$\chi_m = \frac{s_m^* - s_m}{s_{SST}^* - s_b} \tag{1.3}$$

where s_m^* is the saturation entropy at 600 hPa, s_m is the entropy at 600 hPa, s_{SST}^* is the saturation entropy at the sea surface, and s_b is the entropy in the boundary layer. The ventilation index thus compares the "anti-fuel" effect of high vertical wind shear and low mid-tropospheric humidity to the fuel sources included in the potential intensity, such as high SST. Tang and Emanuel (2012) find that most TCs are generated at VI values of below 0.1. Whether a TC intensifies or weakens in an environment of given VI is more complex. TCs most frequently intensify at VI values below 0.01, and weaken most frequently at VI values above 0.04, though there is great overlap in the distribution of VI for intensifying and weakening TCs. High vertical wind shear and low environmental humidity both act to reduce the saturated potential temperature of the updraft, which increases the outflow temperature in the Carnot engine model of Emanuel (1986), which reduces the temperature difference between the surface and the outflow, which reduces the efficiency of the heat engine. Vertical wind shear also enhances the entrainment of dry air into the boundary layer, which dries the inflow of forming and existing tropical cyclones (Riemer et al., 2010; Riemer and Laliberté, 2015), thus reducing equivalent potential temperature and increasing the outflow temperature, which reduces the efficiency of the heat engine.

A proposed development pathway of an initial disturbance into a TC is described in detail in a review paper by Montgomery and Smith (2014). Within a disturbance with radial inflow, convective cells develop and stretch the vorticity field. These cells are called vortical hot towers (VHTs). These VHTs move towards the center of the inflow region and aggregate. During this aggregation process, the cyclone becomes increasingly axisymmetrical, and positive vorticity anomalies are moved towards the center while negative anomalies are moved outwards.

For the TC to spin up, two mechanisms work in tandem, both related to the convergence of angular momentum. Above the planetary boundary layer, angular momentum is materially conserved, such that convergence increases the tangential wind speed as per the equation

$$M = rV + \frac{1}{2} f r^2 \tag{1.4}$$

where M is the angular momentum, r is the radius from the cyclone center, V is the tangential wind speed, and f is the Coriolis parameter. For M to be conserved, a reduction in r, i.e. radial inflow of an air parcel, must lead to an increase in V. This process increases the radial pressure gradient, which also increases the radial pressure gradient in the boundary layer. The second mechanism is convergence in the boundary layer, where M is not conserved due to the presence of friction. However, the reduction of V caused by the reduction in M can be offset by a sufficiently fast reduction in r, ultimately increasing V as an air parcel moves towards the center. The inflow slows down underneath the eyewall as the inward flowing air becomes supergradient (i.e., faster than gradient wind), which causes horizontal convergence in the boundary layer inflow. As a result, air is lifted and condensation occurs. These two mechanisms thus steadily increase the radial pressure gradient, inflow and tangential wind speed to spin up the TC.

Another genesis pathway is the tropical transition of a precursor cyclone (Davis and Bosart, 2003). Precursor cyclones typically exist in a baroclinic environment of high vertical wind shear, but show a reduction in baroclinicity and vertical wind shear just prior to transitioning into TCs. The precursor cyclone acts as a conduit that enables the organization and development of the emerging TC. McTaggart-Cowan et al. (2013) found that TCs formed via tropical transition account for over one third of North Atlantic TCs.

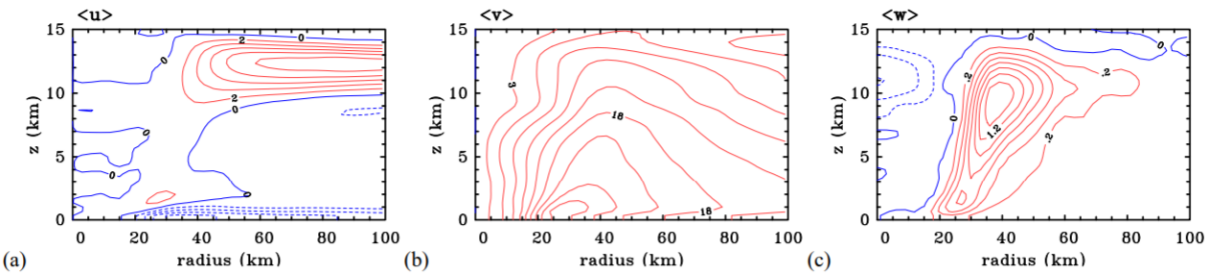

Figure 1.3: Figure 2a-c of Persing et al. (2013). Azimuthal means of radial (a), tangential (b) and vertical (c) wind in ms^{-1} of a rapidly intensifying simulated tropical cyclone. Red contours show positive values, blue dashed contours show negative values, and the blue solid contour shows the zero contour.

1.1.2 Structure of Tropical Cyclones

The large scale cyclonic rotation of a TC can be described by the gradient wind balance

$$-\frac{1}{\rho}\frac{\partial p}{\partial r} = fV + \frac{V^2}{r} \tag{1.5}$$

where ρ is density, p is pressure, r is the radius, f is the Coriolis parameter, and V is the tangential velocity. The left hand side of the equation describes the pressure gradient force, which accelerates an air parcel towards the center. The right hand side describes the Coriolis force and the centrifugal force, which accelerate an air parcel away from the center. A velocity that is larger than the gradient wind balance would predict is called supergradient wind, and a velocity that is smaller than the gradient wind balance would predict is called subgradient wind. In the presence of friction, V is reduced, causing net acceleration towards the center. As described in the previous subsection, this increases wind speed. Therefore, friction has the paradoxical role of increasing wind speed in the boundary layer.

TCs have a structure that is very distinct from that of extratropical cyclones. One key difference is the near radial symmetry of tropical cyclones, which allows for the representation of structural elements in azimuthal mean fields around the center. Persing et al. (2013) performed a simulation with 3 km horizontal grid spacing to produce figure 1.3 (their figure 2a-c), which shows the azimuthal mean wind vector components during a period of rapid intensification. Several features that differentiate tropical cyclones from other cyclones can be identified in it.

In panel a, the azimuthal mean radial wind speed is shown. Within the boundary layer, the dashed lines indicate negative velocity, i.e. a velocity towards the center. This feature is the frictionally induced inflow that is described above. While the strong inflow is confined to the boundary layer, weaker inflow extends to about 10 km height. This inflow causes momentum to converge towards the TC center, and counteracts outflow at low altitudes. The cause for this inflow is latent heating in the eyewall. The convection is more than strong enough to remove the mass converging in the boundary layer, and therefore induces inflow above the boundary layer as well (Montgomery and Smith, 2017). Directly above the boundary layer, there is a small region of outflow. The outflow is caused by the wind being supergradient, and boundary layer air ascending to a level above the strong inflow due to convergence. It can then move outwards, only being hindered by the weaker inflow above the boundary layer. The much larger and stronger outflow region aloft is where the mass that converges at lower levels is expelled away from the TC center. The temperature of this outflow layer is highly relevant to the efficiency of the Carnot engine view on tropical cyclones (Emanuel, 1986). The weak outflow throughout the troposphere at low radii is indicative of the outward slope of the eyewall. The inflow in the boundary layer and outflow aloft constitute the radial components of a secondary circulation within a TC with ascent in the eyewall and slow subsidence away from the center being the vertical components.

In panel b, the azimuthal mean tangential wind speed is shown. The positive values indicate counter-clockwise rotation in the northern hemisphere (i.e., cyclonic rotation). This rotation is the primary circulation of a TC, and constitutes the strongest wind component. The maximum wind speed is found near the top of the boundary layer, where there is frictionally induced inflow, but the loss of momentum due to friction is weak (Montgomery and Smith, 2017). The radial position of this wind maximum is where the inflow stagnates and there is strong vertical motion. The tangential wind speed decreases with height due to the thermal wind relation, which induces anticyclonic flow around a positive temperature anomaly (such as the warm core of a TC) in its upper levels. However, as ascending air cannot change its velocity instantaneously, the reversal of the circulation to anti-cyclonic flow occurs in the outflow, some distance away from the center, and is therefore not seen in fig. 1.3.

In panel c, the azimuthal mean vertical wind speed is shown. There is a region of deep convection from the boundary layer to near the tropopause where the radial inflow in the boundary layer stagnates. The stagnation of the inflow causes convergence, which is compensated by forced vertical motion. Due to high evaporation rates caused by high wind speed, the air in the boundary layer is very humid. This allows for condensation, and thus latent heat release, to occur at low altitudes upon lifting. The large latent heat release of the lifted air enables the resulting convection to warm the air sufficiently to reach altitudes close to the tropopause. The resulting convective cloud is the eyewall of the tropical cyclone, and constitutes the vertical component of the secondary circulation. Towards the center of the eyewall, there is weak subsidence. The cause for this subsidence is that as the ascent in the eyewall stagnates, strong flow away from the center and weak flow towards the center are induced. The inflow forces air to subside in the eye. As air in the eye is thus warmed along its trajectory, the eye is cloud free in a well developed eye.

Another structural element that differs from its extratropical counterpart is the warm core of a tropical cyclone, as seen in fig. 1.2. Haurwitz (1935), almost a century ago, used the existence of a warm core to argue that the height of a tropical cyclone is substantially more than 3 km, as was previously assumed due to deteriorating wind speeds with height. He further described the dry, subsiding air in the eye, and correctly assumed that this air mass previously ascended in the eyewall, where it warmed and lost much of its humidity, and is not simply heated environmental surface air. While this may seem banal to a modern reader, it underlines the immense difficulty that one faces when observing violent weather without remote sensing and without aircraft. With rather simple means, he also described how the warm core increases in radius with height, producing a funnel-like structure. More recently, Durden (2013) used vertical soundings of warm cores to show that there is great variability in the structure of warm cores. Anomaly maxima are found anywhere between 760 and 250 hPa. Further findings are that stronger anomalies tend to have a larger vertical extent, and are linked to stronger TCs, as would be expected from hydrostatic considerations.

1.1.3 North Atlantic Tropical Cyclone Tracks

The movement of a TC across the surface of the planet is primarily governed by two factors. The first, and more dominant, is the environmental flow. The second is the β-effect (Holland, 1983), which describes a westward and poleward component of the TC's motion that is caused by the meridional gradient of the Coriolis parameter and the conservation of absolute vertical vorticity (Rossby and collaborators, 1939).

Colbert and Soden (2012) separate the tracks of North Atlantic tropical cyclones that form in the main development region (MDR, Goldenberg and Shapiro (1996)) into three categories, as seen in figure 1.4 (their figure 1b). They define the MDR as the region spanning from 10°N to 20°N and from 65°W to 17.5°W. The categories are straight moving (SM), recurving

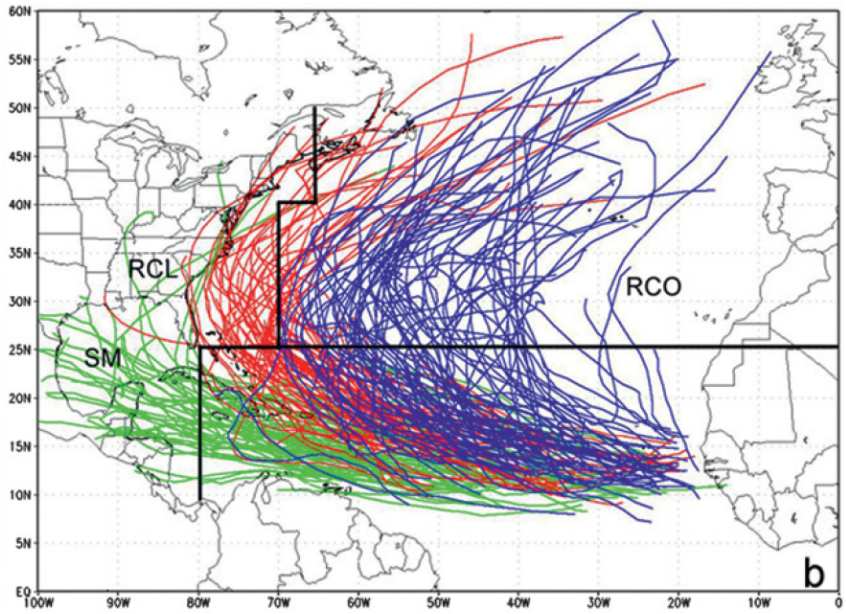

Figure 1.4: Figure 1b of Colbert and Soden (2012). Recurving ocean (RCO, blue), recurving landfall (RCL, red) and straight moving (SM, green) tropical cyclone track categories. Black lines delineate the borders between the categories.

landfall (RCL) and recurving ocean (RCO) tracks. They note that generally, SM TCs are generated further to the west and south of the other categories, giving them less time to be moved northwards by the β-effect. RCO TCs, generally forming farthest to the east, have the most time to be deflected northwards by the β-effect. Colbert and Soden (2012) further describe that the strength and extent of the North Atlantic subtropical high-pressure system (NASH) exerts a substantial influence on the track of tropical cyclones. A strong and large NASH favors SM tracks, while a weak and small NASH favors RCO tracks, due to its effect on the environmental steering flow.

1.1.4 Extratropical Transition

TCs that move polewards and do not undergo landfall will at some point interact with the extratropical flow. This can cause the cyclone to become asymmetrical, develop fronts, and lose its warm core. This interferes with the circulation of the cyclone, impeding its ability to sustain its intensity as a tropical cyclone. TCs that begin extratropical transition thus generally weaken, but may re-intensify as extratropical cyclones if they complete the transition.

Evans and Hart (2003) use the thermal asymmetry and transition of a warm core to a cold core structure to produce a definition of extratropical transition. A tropical cyclone approaching a mid-latitude trough has a thermal gradient imposed onto it, producing an asymmetry. A transitioning TC will be steered by a westerly flow, such that the air to the left, more poleward side of its motion is colder than the air to the right, more equatorward side on the northern hemisphere, and vice versa on the southern hemisphere. Evans and Hart (2003) thus define

$$B = h\left(\left(\overline{Z_{600} - Z_{900}}\right)_R - \left(\overline{Z_{600} - Z_{900}}\right)_L\right) \tag{1.6}$$

where B is the storm-relative thickness field asymmetry, i.e. the difference in the geometric height of the 600-900 hPa mean altitudes to the right and left of the cyclone relative to its motion, h is an indicator for the hemisphere, with $h = 1$ for the northern hemisphere and $h = -1$ for the southern hemisphere, Z is the geometric height of the indicated pressure levels, the subscripts $_{600}$ and $_{900}$ denote the 600 and 900 hPa pressure levels, respectively, and the subscripts $_R$ and $_L$ denote the right and left side relative to cyclone motion, respectively. The overbar denotes

an areal mean within a semicircle. The radius to which the areal mean is considered is 500 km. Extratropical transition onset is defined to have begun when B exceeds a value of 10 m.

As cyclones weaken during the extratropical transition process, some of them decay and do not finish the process, while others can re-intensify as extratropical cyclones. Evans and Hart (2003) thus define

$$-V_T^L = \frac{\partial \left(Z_{MAX} - Z_{MIN} \right)}{\partial \ln p} \Bigg|_{900\ \text{hPa}}^{600\ \text{hPa}} \tag{1.7}$$

where $-V_T^L$ is a measure for thermal wind, Z_{MAX} is the maximum isobaric height and Z_{MIN} is the minimum isobaric height within a 500 km radius, and p is pressure. As tropical and extratropical cyclones are low pressure systems, and this low pressure anomaly generally persists to beyond 600 hPa in height, Z_{MIN} is close to the center, and Z_{MAX} is far away from the center. $-V_T^L$ is thus a measure of whether the pressure anomaly weakens or strengthens with height. The sign of $-V_T^L$ is indicative of the direction of thermal wind, and thus of whether the core is warm or cold. Extratropical transition is defined to be completed when $-V_T^L$ becomes negative, i.e. when the warm core of the cyclone developed into a cold core.

Hart and Evans (2001) found that roughly half of North Atlantic hurricanes undergo extratropical transition, and that roughly half of landfalling TCs in the North Atlantic undergo extratropical transition. They also found that there is a seasonal cycle in the mean latitude of transition, with it being low early in the season, high in the mid-season, and in between late in the season.

1.2 Sub-Seasonal and Seasonal Tropical Cyclone Activity Predictions

Upon reaching land TCs can cause substantial damage to life and property. While the potential for damage caused has not increased during the past century, an increase in population and wealth along the North American coast has led to an increase in damage, i.e. the coasts have become more vulnerable (Pielke Jr. et al., 2008).

Predicting the activity of a TC season can aid in preparatory work to mitigate the damage they cause. This gives rise to the need for sub-seasonal and seasonal forecasting of TC activity. In the North Atlantic basin, this effort has been ongoing and steadily improved since the early 1980s (Gray, 1984a,b). Forecasts can use a statistical or a dynamical approach, and the two can be combined to form a hybrid approach.

1.2.1 Statistical Forecasting

The first attempts at forecasting the seasonal TC activity used a statistical approach, where certain predictors that correlate with TC activity are combined to produce a forecast. Nicholls (1979) correlated the pressure anomaly at Darwin, Australia during winter to the number of TCs in the Australian region. The estimated correlation coefficient of -0.6 suggested that skillful forecasts could be produced based solely on this pressure anomaly. Gray (1984a,b) related the North Atlantic seasonal tropical cyclone activity, measured in number of hurricanes, hurricane days and storm days, to the El Niño-Southern Oscillation (ENSO), the Quasi-Biennial Oscillation (QBO) and regional sea-level pressure anomalies in the Caribbean basin. He found that the ENSO correlates somewhat well with the number of hurricanes and tropical storms, and that the direction of the QBO correlates quite well with both the number of hurricanes and tropical storms and the number of hurricane days. Gray et al. (1992a) found that the influence of the QBO is linked to an increase in upper level ventilation for east phases of the QBO, while the ventilation is reduced in west phases. Gray et al. (1992b) further argue that east QBO phases are linked to enhanced convection within 7° of the equator, while west phases are linked to enhanced

convection within 8–18° the equator. West QBO phases are thus linked to enhanced convection in regions where TCs are generated, which in turn increases TC activity. ENSO has also been linked to vertical wind shear in the North Atlantic main development region for TCs, such that warm SST anomalies in the eastern Pacific basin are associated with an increase in vertical wind shear, and therefore a reduction in TC activity (Goldenberg and Shapiro, 1996).

Klotzbach and Gray (2004) use several predictors linked to the QBO and ENSO, but further include predictors linked to the North Atlantic Oscillation (NAO), the Pacific-North-American pattern (PNA) and the Arctic Oscillation (AO) to demonstrate that statistical predictions can have skill even when performed six to eleven months in advance. Saunders and Lea (2005) use July horizontal winds in several different regions to produce skillful forecasts for the wind energy of TCs undergoing landfall in the USA from August to October. Klotzbach (2007) concludes that statistical forecasting has improved greatly since its inception, and is likely to improve with the improvement of global data sets such as ECMWF (European Centre for Medium-Range Weather Forecasts) reanalysis products.

1.2.2 Dynamical Forecasting

Dynamical forecasting aims to predict TC activity by using numerical models within which TC activity can be determined directly by tracking them, or indirectly by deriving it from the prediction of other quantities via statistical methods. The latter is the aforementioned hybrid approach. Thorncroft and Pytharoulis (2001) produced skillful forecasts of vertical wind shear in the main development region of North Atlantic hurricanes, which could be used to draw conclusions on TC activity. Vecchi et al. (2014) find that while a purely dynamical approach shows skill, a hybrid method using SST predictions outperforms the purely dynamical predictions especially at long lead times of several months to half a year. They also conclude that sub basin-scale predictions are feasible. Dynamical forecasting generally provides skillful results (e.g., Thorncroft and Pytharoulis (2001); Vitart et al. (2007); Vecchi et al. (2014); Zhang et al. (2019), and operational forecasts have good skill in predicting TC number and provide information on regional activity and landfall locations (Klotzbach et al., 2019).

Befort et al. (2022) compared six different European seasonal forecasting models (ECMWF SEAS5 (Johnson et al., 2019), U.K. Met Office GloSea5-GC2 (MacLachlan et al., 2015), Météo France System 5 (France, 2015), Météo France System 6 (Dorel et al., 2017), DWD GCFS2.0 (Fröhlich et al., 2021) and CMCC SPS3 (Gualdi et al., 2020)) with horizontal resolutions ranging from about 32 km to about 110 km (see table 1 of Befort et al. (2022)). They show that the number of TCs in the North Atlantic basin throughout a season is generally represented well in its total number and the seasonal cycle, though the total number is underestimated by some models with coarser horizontal resolution. Notably, all models also have skill specifically in the tropical coastal regions of North America. The seasonal energy of TCs produced in the models is found to correlate well with observations and reanalyses. However, while the models are skillful in the West Pacific basin as well, this is not the case specifically at the western coastline.

A summary of the performance of twelve forecasting centers using statistical, dynamical and hybrid methods can be found in Klotzbach et al. (2019). They conclude that forecasts have a good level of skill, and recommend the use of newly available historical data sets for statistical forecasting and for the calibration of methods. They further recommend the inclusion of new techniques, such as machine learning, and exploring the potential for regional and multi-annual predictions.

1.2.3 The 2013 North Atlantic Hurricane Season

The 2013 North Atlantic hurricane season was forecast to be above average in activity, but in reality this was not the case. Only two category 1 hurricanes (i.e., hurricanes with a maximum

wind speed between 33 m/s and 42 m/s) and no major hurricane occurred, which is well below average. A reason for this was proposed by Zhang et al. (2016), who found that an abundance of Rossby wave breaking dried the tropical North Atlantic by mixing relatively dry extratropical air into it, and by increasing vertical wind shear.

Potential vorticity (PV), defined as:

$$PV = \frac{\eta \cdot \nabla\theta}{\rho} \tag{1.8}$$

where η is absolute vorticity, $\nabla\theta$ is the gradient of potential temperature,and ρ is density, can be used to detect PV streamers. PV streamers are elongated filaments of the 2 PV unit (PVU) contour which protrude into the troposphere, and can be used as a proxy for a breaking Rossby wave Wernli and Sprenger (2007); Béguin et al. (2013); Sprenger et al. (2017). The frequency, size and anomaly magnitude of PV streamers have all been found to correlate negatively with TC activity in the North Atlantic region Zhang et al. (2017); Papin et al. (2020).

1.3 Tracking of Tropical Cyclones in Numerical Model Data

Numerical modeling produces large amounts of data that require some degree of automation to analyze. Fortunately, the distinct structure of TCs allows for an algorithm to detect TC centers based on a number of criteria, and to distinguish them from extratropical cyclones.

Commonly used structural features are the presence of a central pressure minimum with a nearby maximum in low-level vorticity (e.g., Chauvin et al. (2006); Bengtsson et al. (1995); Zhao et al. (2009)), or only a central low-level vorticity maximum (e.g., Hodges (1999)), which detects cyclonic weather systems, and evidence for a warm core, which distinguishes TCs from other cyclones. Identifying the warm core of a TC can be done either by directly assessing the warm core itself (e.g., Bengtsson et al. (1995); Chauvin et al. (2006); Zhao et al. (2009)), or by assessing the wind or vorticity change with height, as both weaken with height in the presence of a warm core (e.g., Bengtsson et al. (1995); Chauvin et al. (2006); Strachan et al. (2013)).

An alternative way of identifying TC centers is described in Tory et al. (2013), who use an adapted form of the Okubo-Weiss (OW) parameter, which they call the OWZ parameter. It is defined as

$$OWZ = \max\left(\frac{\zeta^2 - \left(E^2 + F^2\right)}{\zeta^2}, 0\right) \cdot \eta \cdot \operatorname{sign}(f) \tag{1.9}$$

where ζ is the vertical component of relative vorticity, E is the stretching deformation, F is the shearing deformation, and η is the vertical component of absolute vorticity. The OWZ parameter quantifies the solid body component of the rotation of the cyclonic absolute vorticity, which aids in identifying low-deformation environments. A high OWZ implies a sheltered environment within which a TC can develop, which makes the OWZ parameter well suited for detecting early stages of a TC. The OWZ parameter can be jointly used with vertical wind shear and relative humidity criteria to track TCs (Tory et al., 2013; Bell et al., 2018).

An issue that all TC tracking algorithms share is the reliance on threshold parameters. For example, if a low-level vorticity maximum is detected, it must be sufficiently strong to be counted as a potential TC center. This is necessary to not track any spurious signal, but only cases where a TC is strongly suspected to be present. These thresholds are chosen subjectively. As a result, the performance of any TC tracking algorithm is sensitive to the choice of parameters (Horn et al., 2014). If the parameters are too weak, then false positives become more likely. If they are too restrictive, then viable model TCs are more likely to evade detection, especially at weak stages in their life cycle. A possible solution to this is presented by Camargo and Zebiak (2002), who use one set of parameters to detect TCs, and another set of parameters to expand the search

forwards and backwards in time once a TC has been detected. The first set of parameters serves to reduce the probability of false positives, while the second set serves to detect the tail ends of TCs.

1.4 Objectives

This thesis covers a potential improvement of seasonal and sub-seasonal tropical cyclone activity forecasts by using the large scale potential vorticity structure in the North Atlantic basin. This can be subdivided into three main objectives, as described below.

1.4.1 Development of a Tropical Cyclone Tracking Algorithm

If there is a relationship between the tropical cyclone activity and the large scale potential vorticity field, then it is important to know if this is reproduced in numerical models. To assess the behavior of tropical cyclones within model data, these must be reliably tracked. Therefore, a pre-existing tracking algorithm (Kleppek et al., 2008) is adapted and expanded. This leads to the following objectives:

- Adaptation of the Kleppek et al. (2008) algorithm for use with ICON
- Implementation of a warm core criterion
- Implementation of threshold parameter variation
- Validation of the new tracking method

1.4.2 Large Scale Potential Vorticity Influence on Tropical Cyclone Activity

To improve statistical tropical cyclone activity forecasts, there must be some relation between a predictor and tropical cyclone activity. Possibly, there is such a predictor that is related to the large scale upper-tropospheric potential vorticity field. This leads to the following two research questions, which are to be answered within this thesis:

- Is there a link between the large scale potential vorticity field and tropical cyclone activity in the North Atlantic basin in reanalysis and observational data?
- If this link exists, what is the underlying physical mechanism?

1.4.3 Assessment of Sub-Seasonal Potential Vorticity Forecasts

If a link between the large scale potential vorticity field on the 360 K isentropic surface and tropical cyclone activity exists in reanalysis and observational data, then it is of interest to assess whether numerical models can reproduce it. Regional numerical simulations are thus performed to explore the relation between the potential vorticity field and TC activity in model data. The following two questions are to be addressed:

- Is the relation between the large scale potential vorticity field and North Atlantic TC activity that has been found in reanalysis and observational data reproduced in numerical simulations?
- If the this link is reproduced, is it based on the same underlying physical mechanism?

Chapter 2

Data and Methods

2.1 The ERA5 Reanalysis Product

ERA5 is a ECMWF reanalysis product. Within this thesis, ERA5 is used to initialize model simulations and force the lateral boundaries of model simulations. It consists of a data assimilation component, a forecasting component, and an observational component. The ERA5 reanalysis product is described following Hersbach et al. (2020) and the references therein.

ERA5 uses a sequential data assimilation scheme, which advances in 12-hourly analysis cycles. Within each cycle, observations are combined with prior information from a forecast to estimate the evolution of the atmosphere and the surface. This includes a variational analysis of upper-air atmospheric fields (temperature, wind, humidity, ozone) and near-surface parameters (2 m temperature, 2 m humidity, surface pressure), soil moisture, soil temperature, snow and ocean waves. The analyses provide the basis for a short-range forecast, initialized 9 hours into the 12-hour cycle, which provides the background estimate for the next cycle. The forecast ensures that observations can be extrapolated in space and time in a physically meaningful way, and to estimate parameters that are not directly observed, such as turbulent fluxes or cloud properties.

The data assimilation uses a hybrid incremental 4D Var analysis, where an ensemble component of one control and nine perturbed members are used to determine background error estimates for the deterministic data assimilation. Uncertainties is the reanalysis product can thus be estimated. The data assimilation consists of a 4D Var analysis for the atmosphere, and data assimilation for surface parameters.

The goal of the 4D Var analysis is to constrain the model forecast with observations. This requires a background estimate from the preceding cycle, observations within the current analysis, and second order moment error characteristics of the background state, bias parameters and observations. The error characteristics for the background state are derived from an ensemble of ten members.

The ensemble data assimilation system uses ten members to estimate background errors. One of these uses unperturbed data to run (the control), and the other nine used perturbed data. The members use a lower resolution than the 4D Var analysis, namely TL319 as compared to TL639. The perturbations are randomly sampled from a Gaussian distribution with a variance equal to the expected variance of the observation errors. Model physical tendencies in the short-range forecasts that link analysis cycles are perturbed likewise. As the number of members is quite limited, additional climatological information is used to determine background error covariances. The weight of the climatological information is smaller for larger wave numbers.

Land surface parameters are weakly coupled to the atmosphere, in that they influence each other only in the following assimilation cycle by being relevant to the forecasting process of the

next background state. First, prognostic 2 m temperature and relative humidity, and snow depth and density are analyzed. Then, soil moisture, soil temperature, ice temperature and snow temperature are determined. Over the ocean, 2 m temperature and humidity are diagnostic, such that they do not influence subsequent results. This prevents land observations from influencing the state over the ocean.

ERA5 uses the IFS release Cy41r2, containing three fully coupled components for atmosphere, land surface and ocean waves. The horizontal resolution is about 31 km. 137 vertical levels are used, the model top being at 1 Pa.

Observations are subjected to a number of quality control and data selection steps. Data can blacklisted a priori, which is done when instruments have anomalous periods, for specific regions or satellite channels, and for certain variables such as 10 m wind over land. Observations can also be given a low weight to reduce their impact.

2.2 HURDAT2 Hurricane Data

2.2.1 Data Set Description

HURDAT2 is a dataset developed by the National Hurricane Center (NHC) of the USA. It is described here following Landsea and Franklin (2013). The dataset is a post-storm analysis that contains data for the intensity, central pressure, position and maximum extent of 34, 50 and 64 kt winds for each quadrant. The precision of the dataset is 5 kt, 1 hPa, 0.1°, 5 nautical miles (n mi), 5 n mi and 5 mi, respectively. For the storms considered in this thesis, data are available at synoptic times (0000, 0600, 1200 and 1800 UTC). Before 1956, data were analyzed only once or twice a day, and were interpolated to synoptic times to construct the dataset. Prior to 1979, central pressure data were only included when specific observations could be used explicitly as best track values. From 1979 onward, estimates have been produced for all synoptic times. From 2004 onward, size information is included in the data set. Asynoptic times are included for cases where landfall or peak intensities occur outside of synoptic times for 1851-1945 and from 1991 onward. The best tracks are subjective assessments based on many data, some of which are only available after the storm has passed. These data can contradict each other, and the manual construction of the best tracks relies on the experience of NHC hurricane specialists to weigh the available data to create a sensible history for each storm. To ensure that the data are representative of the 6-hour interval they are centered on, variations with time scales of less than 24 hours are not represented within HURDAT2, even if they are known quite accurately. The HURDAT2 data are thus smoothed, which can cause discrepancies between the best track data and observations, including for the position of the storms. This is not the case for landfall positions, where the NHC's best estimate for the actual landfall position, intensity and time are used. Given the remote position of tropical cyclones over oceans, where measurements are difficult, the best tracks rely heavily on remote sensing via satellites. Only about 30% of storms have aircraft observations.

2.2.2 Uncertainty Estimates

Landsea and Franklin (2013) further provides an uncertainty estimate of the data set. However, this estimate is based on a 2010 survey of the specialists who construct the best tracks, and number only eleven persons (seven for a prior survey in 1999). The uncertainty estimates are therefore to be considered only as "ballpark estimates", as it is put in Landsea and Franklin (2013), and are justified by the absence of any other measure (i.e., they are better than no estimate at all).

The uncertainty in intensity increases slightly with increasing intensity of storms, but the uncertainty relative to the intensity decreases from about 25% for tropical storms to about 15% in category 1 and 2 hurricanes and about 10% for major hurricanes for satellite-only observations. For storms with satellite and aircraft observations, the relative uncertainty is about 15%, 10% and 8%, respectively. The inclusion of aircraft measurements thus reduces the relative uncertainty substantially, more so for weaker storm systems. The uncertainty is reduced compared to that in 1999, due to new tools made available in the 2000s.

The uncertainty for central pressure increases with increasing storm intensity, especially so for satellite-only measurements. The relative uncertainty is about 30% for tropical storms, about 20% for category 1 and 2 hurricanes, and about 15% for major hurricanes. The inclusion of aircraft measurement improves this drastically, yielding about 20%, 10% and 5% relative uncertainty, respectively.

The uncertainty in position is both dependent on the intensity of storms, with a decrease for more intense storms, and on the availability of data, with the addition of aircraft measurements reducing uncertainty, and land-based observations for landfalling storms reducing it further. For tropical storms, the uncertainty for satellite-only measurements is about 35 n mi, which is reduced to about 22 n mi when aircraft measurements are included, and about 18 n mi for landfalling storms. As a reference for a relative uncertainty measure, the median radius of the outermost closed isobar is used, which is about 150 n mi for tropical storms and about 200 n mi for both category 1 and 2 and major hurricanes. For satellite-only observations, the relative uncertainty is then about 20% for tropical storms and 10% for hurricanes. the inclusion of aircraft measurements reduces this to about 15% for tropical storms, about 7.5% for category 1 and 2 hurricanes, and about 5% for major hurricanes. Storms undergoing landfall in the USA have this reduced further to about 10%, 5% and 5%, respectively. Surprisingly, the uncertainty estimates are very similar to those in the 1999 survey, despite improvements in monitoring.

The uncertainty for the maximum extent of 34, 50 and 64 kt winds is virtually independent of intensity, but show a strong dependency on data availability. The relative uncertainty is quite large for all intensities for satellite-only data, with about 40% for tropical storms, and about 30% for hurricanes of all categories for the 34 kt wind radii. The inclusion of aircraft measurements reduces this to about 35% for tropical storms, about 25% for category 1 and 2 hurricanes, and about 20% for major hurricanes. For landfalling hurricanes it is further reduced to about 30%, 20% and 20%, respectively. The relative uncertainties for the 50 and 64 kt winds are even higher. While these uncertainties might seem alarming, it should be noted that storm size data are not used within this thesis, and mentioned here only for the sake of completeness.

2.3 ICON - the ICOsahedral Nonhydrostatic Atmosphere Model

The ICOsahedral Nonhydrostatic atmosphere model (ICON) was developed by the German Weather Service (DWD) and the Max-Planck-Institute for Meteorology (MPI-M). It is specifically designed to allow for global, regional and large eddy simulation (LES) applications, to scale well with parallel high-performance computing architecture, and to allow for nested grids, where a local, high resolution grid is inserted into a parent grid of coarser resolution. Zängl et al. (2015) describes the dynamical core of the model. This section follows the ICON model tutorial (Prill et al., 2019) and references therein in describing the grid and used parametrizations.

2.3.1 The Horizontal Grid

What differentiates ICON from many other models is the peculiar icosahedral grid, which was pioneered in NICAM (Nonhydrostatic ICosahedral Atmosphere Model) (Satoh et al., 2008, 2014) with great success. With this grid, the planet is represented by a 20-sided die (an icosahedron), which is projected onto a sphere. The nomenclature used to describe the grid resolution is of the

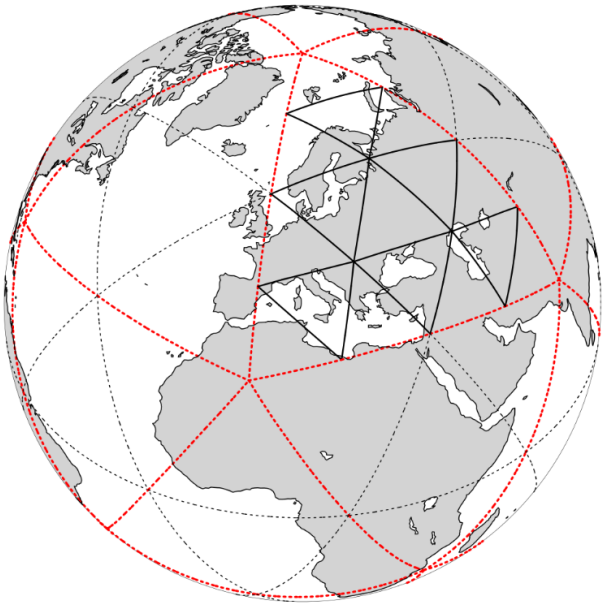

Figure 2.1: Figure 2.1 of Prill et al. (2019). The base icosahedral grid (R1B0) is shown in dashed red lines, the R1B0 grid is shown in dashed black lines, and the R1B2 grid is shown in solid black lines.

form RnBk, where the icosahedron edges are divided into n parts, and the resulting edges are bisected k times. This results in a grid that is quasi, though not exactly, uniform in cell area. Figure 2.1 shows the base grid (R1B0) in dashed red lines. The sides of the original icosahedron are not further divided into parts, and the sides are not bisected. The dashed black lines show a R2B0 grid, where the original sides are divided into 2 parts. The solid black lines show a R2B1 grid, where the R2B0 grid is bisected once.

2.3.2 Radiation Parametrization

Radiation is calculated using the Rapid Radiative Transfer Model (RRTM), which is described here following Mlawer et al. (1997). The RRTM uses the correlated-k method, which is an accelerated calculation that approximates fluxes and cooling rates in a heterogeneous atmosphere. For each homogeneous layer and spectral band, a small set of absorption coefficients is used. To obtain representative values for the absorption coefficients, they are transformed into a cumulative probability function within a spectral band, i.e. the absorption coefficient becomes a function of the cumulative probability instead of wave length. Sub-intervals of the cumulative probability are then used to determine characteristic values for the absorption coefficient. The error caused by this approximation is solely due to the finite size of the sub-intervals, such that the accuracy of the method is determined by the desired computational efficiency. A second error source is the extension of this method to a vertically heterogeneous atmosphere. The outgoing radiation of one layer at a specific value of the cumulative probability is the incoming radiation of the adjacent layer at the same cumulative probability value. However, the mapping from wave length to cumulative probability typically differs from layer to layer, giving rise to errors. This error source is only absent if the distribution of absorption coefficients in cumulative probability space were identical from one layer to the next. Mlawer et al. (1997) show that the accuracy of the RRTM is comparable to that of line-by-line models.

ICON uses 16 bands in the long-wave spectrum and 14 bands in the short-wave spectrum. Since radiation is extremely computationally expensive, a reduced radiation grid can be used. If this is done, a coarser grid is used for radiation computations, which are then downscaled to the full grid and empirically corrected to account for high-resolution information on albedo and surface temperature. Within this thesis, no reduced radiation grid is used.

2.3.3 Microphysics Parametrization

ICON can use one-moment or two-moment cloud microphysics schemes. There are two one-moment schemes, where both predict the specific mass of cloud water, rain water, cloud ice and snow, and one additionally predicts graupel. The two-moment scheme predicts the specific mass and number concentrations of cloud water, rain water, cloud ice, snow, graupel and hail, and includes nucleation and microphysical interactions between hydrometeor categories. Using the two-moment scheme is only recommended for at least convection-permitting grid resolutions. Within this thesis, the one-moment scheme that does not predict graupel is used.

2.3.4 Convection Parametrization

Convection parametrizations describe the effect of the aggregate of sub-grid scale convection based on grid-scale variables. They are responsible for vertical mixing of heat, moisture and momentum, convert potential energy into kinetic energy, and produce precipitation. Within ICON, there are three types of convective clouds: shallow, mid-level and deep convection. The parametrization of deep and mid-level convection can be disabled for convection-permitting simulations. As the simulations used in this thesis are not convection-permitting, the full parametrization is used.

The scheme is a spin-off of the Tiedtke-Bechtold scheme, which is described here following Bechtold et al. (2004). Bechtold et al. (2008) for the vertical variation in mass flux and the convective adjustment time.

The convection scheme uses the assumption that convectively available potential energy (CAPE) is consumed over a given time scale, the convective adjustment time. While Bechtold et al. (2004) uses a constant value of 1 hour, this is not the case in ICON, which follows Bechtold et al. (2008) and uses a time scale that is dependent on the convective turnover time-scale, and thus the vertical velocity and vertical extent of a cloud, and on the model resolution. The cloud top is calculated based on an updraft vertical velocity equation, with the top being where the vertical velocity is zero. The scheme first attempts to identify shallow convection, which has a cloud depth of less than 200 hPa, by considering an air parcel with strong entrainment in the first model level above the surface with an imposed temperature and moisture perturbation. The scheme then attempts to identify deep convection with weak entrainment originating in the first 300 hPa above the surface, excluding the lowest model layer. If there is deep convection, it replaces any shallow convection identified in the first step. If no deep convection is found, the next model level is considered. Below the first 60 hPa above the surface, the average of a 30 hPa layer is lifted, while above the first 60 hPa above the surface full model layers are lifted. The cloud base is not required to be buoyant, but is required to have a positive vertical velocity. The vertical variation of the convective mass flux follows Bechtold et al. (2008) and is described in terms of entrainment and detrainment, which are both separated into a turbulent and an organized convective component. Entrainment is formulated as a function of environmental specific humidity and saturation specific humidity, such that environmental humidity exerts a very strong control over the convective mass flux. The turbulent component of detrainment is constant, and the organized convective component is proportional to the reduction in updraft kinetic energy when the parcel becomes negatively buoyant.

2.3.5 Turbulent Diffusion Parametrization

The following description is based on the ICON model tutorial (Prill et al., 2019) and Raschendorfer (2001). There are two components to the turbulent diffusion scheme, one in the free troposphere and one in the surface layer.

The turbulent kinetic energy (TKE) is a prognostic variable. The prognostic equation includes diffusion of TKE and the production of TKE due to sub-grid scale thermal circulation.

A statistical sub-grid scale cloud scheme is used to account for sub-grid scale condensation. The scheme is based that of , with a notable extension compared to a moist Mellor-Yamada (Mellor and Yamada, 1982) scheme being the formal separation of turbulence from non-turbulent parts of the sub-grid scale energy spectrum. This makes the scheme applicable above the boundary layer and in a very stably stratified atmosphere.

The scheme further calculates transport resistances to fluxes of prognostic variables from the surface into the atmosphere. A vertical interpolation function is derived from the application of the turbulence scheme at the top and the at the bottom of the lowest atmospheric layer, which is then extrapolated to the rigid surface. A vertical integration of the flux gradient representation provides the transport resistances for the bulk surface-to-atmosphere fluxes. The determination of specific roughness lengths for scalars is replaced by a direct calculation of partial resistances for scalar transfer through the laminar and roughness layers, which is dependent on near-surface model variables, the aerodynamic roughness length, and the enlargement of surface area by land use.

2.3.6 Cloud Cover Parametrization

The cloud cover scheme in ICON combines information from the microphysics, turbulence and convection parametrizations. The split between cloud ice and water vapor that is determined in the microphysics scheme is replicated in the cloud cover scheme for the turbulent component of ice clouds. The convective anvil is calculated from an equation dependent on detrainment from the convection scheme and a decay time scale, which is set to 30 minutes. The sub-grid scale variability of water is prescribed by using a top-hat total water, i.e. the sum of water vapor, cloud water and cloud ice, distribution with a width of 10%. Assumptions on the vertical overlap of clouds are made in the radiation scheme.

Chapter 3

Parallel use of Threshold Parameter Variation for Tropical Cyclone Tracking

Bernhard Enz[1], Jan Engelmann[1,2], and Ulrike Lohmann[1]

[1]Institute for Atmospheric and Climate Science, ETH Zurich, Zurich, Switzerland
[2]Institute of Computational Biology, Helmholtz Center Munich, Munich, Germany

This work has been submitted to Geoscientific Model Development and is under review.

Abstract

Assessing the capacity of numerical models to produce viable tropical cyclones, as well as assessing the climatological behavior of simulated tropical cyclones, requires an objective tracking method. These make use of parameter thresholds to determine whether a detected feature, such as a vorticity maximum or a warm core, is sufficiently strong to indicate a tropical cyclone. The choice of parameter thresholds is generally subjective. This study proposes and assesses the parallel use of many threshold parameter combinations, combining a number of weaker and stronger values. The tracking algorithm succeeds in tracking tropical cyclones within the model data, beginning at their aggregation stage or shortly thereafter, and ending when they interact strongly with extratropical flow and transition into extratropical cyclones, or when their warm core decays. The sensitivity of accumulated cyclone energy to tracking errors is assessed. Tracking errors include faulty initial detection and termination of valid tropical cyclones and systems falsely identified as tropical cyclones. They are found to not significantly impact the accumulated cyclone energy. The tracking algorithm thus produces an adequate estimate of the accumulated cyclone energy within the underlying data.

3.1 Introduction

Numerical models are a useful tool to further our understanding of weather and climate, and to make predictions thereof. Within these model simulations, certain features, like tropical cyclones (TCs), can be tracked and their behavior analyzed. TCs are of particular importance, as they pose an immense threat to human life and assets when they make landfall. The damage caused by TCs is likely to increase with an increase in population and wealth in coastal areas (Pielke Jr. et al., 2008). Further, Bender et al. (2010) predicted an increase in the frequency of category 4 and 5 hurricanes in a warmer climate, which is linked to an increase in destructiveness (Grinsted et al., 2019).

Model simulations, especially when performed with high horizontal resolution, for large domains, and for extended periods of simulated time, produce vast amounts of output data. To

analyze certain features, such as the lifetimes, intensities and tracks of TCs, they must be identified. As manually tracking every TC is cumbersome, an automated and objective algorithm is preferable.

Any tracking algorithm implicitly contains a definition of the tracked system, and then searches for instances where this definition is fulfilled. Within the context of TCs, a commonly used baseline is that a TC is a system with a maximum in vorticity collocated with (e.g., (Chauvin et al., 2006)) or in the vicinity of (e.g., (Bengtsson et al., 1995; Zhao et al., 2009)) a minimum in sea level pressure. The maximum in vorticity can be used without requiring the minimum in sea level pressure (e.g., Hodges (1999)). However, this alone does not distinguish TCs from other systems that can occur in the region of interest, such as extratropical cyclones. Therefore, the warm core structure of TCs is usually also searched for during the tracking process, which can be done directly or indirectly.

Directly assessing the warm core is done by defining a temperature anomaly, which compares the temperature at the TC center to that of the environment at a specified altitude or pressure. For example, Bengtsson et al. (1995) require the temperature anomaly at 300 hPa to be larger than that at 850 hPa, while requiring the sum of the temperature anomalies at 300, 500 and 700 hPa to exceed a threshold value. This ensures that the temperature anomaly is stronger at higher altitude, and that it is not too weak. Chauvin et al. (2006) require a strengthening of the temperature anomaly with height, but only that the 700 and 300 hPa temperature anomalies exceed a threshold value. Zhao et al. (2009) use the mean temperature between 500 and 300 hPa to define the temperature anomaly, but use the local maximum thereof, which must be within 2° horizontal distance of the sea level pressure minimum.

Indirectly assessing the warm core is done by searching for a pattern that is consistent with the presence of a warm core. For example, Bengtsson et al. (1995) and Chauvin et al. (2006) require the cyclonic wind to weaken with height, which is indirect evidence for a warm core structure. Strachan et al. (2013) require that the vorticity in the TC center is reduced with height, which is related to the weakening of cyclonic winds with height, and therefore evidence for a warm core. Tsutsui and Kasahara (1996) detect the warm core by requiring the thickness of the 200 hPa - 1000 hPa layer at the center and in the inner region of a TC to be larger than at the periphery. Walsh et al. (2012) combine the direct and indirect criteria, in that they require a positive 300 hPa temperature anomaly and a reduction of wind speed with height.

An alternative method of tracking TCs is provided by Tory et al. (2013), who used the Okubo-Weiss (OW) (Okubo, 1970; Weiss, 1991) parameter and absolute vorticity to form the OWZ parameter. The OWZ parameter reflects the solid body component of absolute vorticity, and can thus be used to identify vorticity rich quasi-closed circulations. It is argued that every TC precursor shows increased OWZ, and thus the OWZ parameter is particularly useful to detect the early stages of a TC. Combined with vertical wind shear and relative humidity criteria, the OWZ parameter can then be used to track TCs (Tory et al., 2013; Bell et al., 2018). A review of TC tracking schemes can be found in appendix B of Ullrich and Zarzycki (2017).

Many tracking criteria across many algorithms require that a system exceeds a corresponding threshold value. For example, the warm core temperature anomaly must exceed the environmental temperature by a predetermined value, or the central vorticity maximum must exceed a predetermined minimum value. This inherently makes tracking algorithms sensitive to the choice of these threshold values (Horn et al., 2014). If the threshold values are too weak, then false positives may be found, and the algorithm cannot be trusted to detect only TCs. If the threshold values are too strict, then TCs that exist in the model can be truncated in the early and late stages, or missed entirely. Furthermore, the horizontal resolution of the model may affect how sensible a given threshold value choice is (Walsh et al., 2007).

While Horn et al. (2014) found that even small changes in threshold parameters can have a large impact on the tracking results, Zarzycki and Ullrich (2017) specify that the impact is large for the discrete count of TCs, but relatively small for integrated metrics such as accumulated cyclone energy (ACE, Bell et al. (2000)).

To make the tracking process less sensitive to the choice of threshold values, it is possible to vary these values. An example of this is provided by Camargo and Zebiak (2002), who use more strict threshold values to first identify TCs, and then use relaxed threshold values forwards and backwards in time when a system is detected. This allows them to detect early and late stages of the TC life cycle with the relaxed values while mitigating the pitfall of falsely tracking non-TC systems.

The relative weakness of the defining TC characteristics at early and late stages in the TC life cycle is not the only complication to their tracking, as the existential question of when a TC begins and when it ends can also be asked outside of the scope of tracking. In the North Atlantic basin, only about 40% of TCs form in the absence of baroclinic processes, and about 40% of TCs form in a process called tropical transition (TT) (McTaggart-Cowan et al., 2013), where a precursor storm moves over warm water and attains TC characteristics (Davis and Bosart, 2003). Warm water is required as TCs form predominantly over water warmer than 26°C (Palmen, 1948), though TT events with a strong initial lower-level circulation can form at slightly lower sea surface temperatures (McTaggart-Cowan et al., 2015).

Montgomery and Smith (2014) describe the initial intensification of a weak cyclonic precursor system. They discuss how many mesoscale systems of deep convection, which they name vortical hot towers (VHTs), locally stretch vorticity within this precursor system, and how the thus produced cyclonic vorticity anomalies aggregate while the corresponding anticyclonic anomalies move outwards. This process gradually increases the vorticity of the precursor system, and allows it to develop into a mature TC.

The termination of a TC can occur quite rapidly when they move over land. Other than this rather straight-forward termination, there is also the possibility for a TC to develop characteristics of extratropical cyclones in a process called extratropical transition (ETT) (Evans and Hart, 2003). ETT occurs when a TC moves poleward and encounters a strong meridional temperature gradient, which enables it to form fronts and thereby strong radial asymmetry. This loss of symmetry and the increased vertical wind shear associated with horizontal temperature gradients cause the warm core to decay, such that the system develops an ETC structure. ETT occurs for 46% of TCs in the North Atlantic basin, and transitioning systems account for about half of the systems that landfall (Hart and Evans, 2001).

Both the initial and final stages of TCs are therefore not instantaneous, but rather processes that take a finite amount of time to conclude. A tracking algorithm would therefore preferably detect a cyclone at some point during its development, and cease to detect it at some point during its termination, as this would capture the entire TC phase of the cyclone while allowing for some leeway during the phases immediately before and after.

While publications typically contain a description of how TCs are tracked, it is by no means common that they include an assessment of how well the tracking algorithm performs. As this is a fundamental component on which the data analysis builds, this paper is devoted to introducing a newly developed algorithm, and assessing how well it performs. The new algorithm uses varying threshold values, which allows it to contain both lax and strict threshold value combinations, which are then combined to form a final tracking product.

The remainder of this paper is structured as follows. Section 3.2 describes the data and methods used to produce model TCs which can then be tracked, as well as the tracking algorithm. Section 3.3 shows that the numerical simulations are capable of producing viable TC-like vortices. Section 3.4 assesses at which stage model TCs are first tracked, and section 3.5 assesses at which stage model TCs are last tracked, and why they terminate. Section 3.6 explores false positives, and how they are caused. Section 3.7 assesses the impact of tracking errors on ACE. Section 3.8 assesses the sensitivity of the tracking process to the allowed translational velocity of TCs. Section 3.9 summarizes the results, and provides the drawn conclusions and an outlook.

3.2 Data and Methods

3.2.1 Numerical simulations

ICON version 2.6.1 (Zängl et al., 2015) is used in limited area mode (ICON-LAM) to produce simulation data with which the tracking algorithm can be validated. The simulation domain spans from 120°W to 15°W and from the equator to 70°N. An unstructured, triangular grid with resolution of R03B07 (see section 2.1 of Zängl et al. (2015) for more information on the grid nomenclature) is used, which corresponds to a grid spacing of about 13 km. 50 vertical levels are used, with the distance between levels increasing with altitude. The first level is at about 10 meters above the surface, and the model top is at 23 km. A time step of 100 s is used. Shallow and deep convection parametrizations are used (Bechtold et al., 2008). An ensemble of 20 members spanning the entire North Atlantic hurricane season is generated for the 2013 season. Within this study, this season is defined as beginning on 00:00 UTC on 1 June and ending on 00:00 UTC on 1 December. The month of May is used to initialize and spin up the simulations, as described below.

ERA5 data (Hersbach et al., 2020) are used to construct the initial state of the simulations, and to prescribe monthly mean values for sea surface temperature and sea ice, and as lateral boundary conditions in 6-hourly intervals. Sea surface temperature, sea ice and boundary conditions are interpolated to individual time steps throughout the simulation. The physical fields that are prescribed at the boundary are zonal, meridional and vertical wind, the logarithm of sea level pressure, temperature, specific humidity, cloud liquid water content, cloud ice water content, rain water content, snow water content and surface geopotential. The first member of the ensemble is initialized at 00:00 UTC on 1 May 2013. The following 19 members have their initial times shifted by 24 hours for each additional member, such that the final member is initialized on 00:00 UTC on 20 May 2013.

Even though the simulations are performed based on data for 2013, the TC activity in the simulations differs strongly from observations. As the intended focus of the study is on the validation of the tracking algorithm, and only a single season is simulated, a comparison of simulated data to observations is intentionally omitted. The intent of the numerical simulations is not to validate the ability of the simulations to reproduce the 2013 North Atlantic hurricane season, but to produce a number of viable model-generated TCs that serve as the basis to validate the tracking algorithm. Thus, the simulated data can, for the focal purpose, be regarded as arbitrary manifestations of some TC season, within which viable TCs exist and can be tracked.

3.2.2 Tropical cyclone tracking and evaluation

The tracking algorithm is based on that of Kleppek et al. (2008), which has previously been adapted to identify TCs in ECHAM output data. New features of the presented algorithm are the inclusion of a warm core criterion, and parallelization and threshold variation to address the threshold choice issue mentioned in section 1.

Variable		Threshold Values				
$p_{s,dis}$	[km]	50	100	150		
ζ_{min}	[s^{-1}]	10^{-6}	10^{-5}			
ΔT_{core}	[K]	0.5	0.75	1	1.25	1.5
T_{dis}	[km]	50	100	200	300	400

Table 3.1: Threshold parameter values used in tropical cyclone tracking.

The tracking algorithm requires mean sea level pressure, the vertical component of relative vorticity, and temperature on the 300 hPa isobaric surface on a regular longitude-latitude grid. For the purposes of this study, the chosen resolution is 0.125° x 0.125°, corresponding to about 14 km at the equator, to which the ICON output is remapped. Vertical vorticity is used not on a pressure level, as ICON internally uses model levels. Over the ocean, these are as a constant geometric height, and so vertical vorticity is used at 2.5 km. While this may seem odd, it should be noted that variations in the vertical vorticity threshold barely shows any impact on the tracking process, as is argued later on. The main purpose of the vorticity criterion is to ensure that the rotation of the system is cyclonic.

Initially, all points on the horizontal grid are potential centers of a TC, and the algorithm then excludes all points that do not meet the criteria mentioned below. All points that remain are considered to be TC centers at this stage. This is done for each time step individually, such that no tracks are constructed at this stage. The following criteria need to be fulfilled for a point to qualify as a potential TC center, with the used values listed in Table 3.1:

1. The sea level pressure must exhibit a local minimum within a given distance ($p_{s,dis}$)
2. The vertical component of relative vorticity must exceed a threshold value within the lower troposphere (ζ_{min})
3. The 300 hPa temperature directly above the sea level pressure minimum must exceed the mean 300 hPa temperature within a given distance (T_{dis}) by a certain value (ΔT_{core})

The algorithm evaluates these criteria in sequence, i.e. it identifies sea level pressure minima, then the identified minima are evaluated for their vorticity, and the remaining points are then evaluated for their warm core structure. All thresholds of this list are varied (see Table 3.1. This is done by prescribing not a single, but multiple threshold values, and all threshold combinations then being used in parallel. This results in multiple distinct sets of identified TC centers, which show considerable overlap especially for strong TCs. Combinations with weak constraints identify weaker TCs more readily, while combinations with strong constraints identify only the stronger phases of TCs. This means that the tail ends of TCs are tracked by the weak constraints, while the strong constraints are less susceptible to falsely tracked points. The choice of threshold parameter values is based on parameters used throughout the scientific literature, and on the physical feasibility of values (e.g., a positive value for the warm core temperature difference that is within a range that can be exceeded by weak TCs). These choices are not tailored to the underlying dataset.

After TC centers at individual time steps are identified, tracks are constructed from them in a second step. To determine whether two TC centers at consecutive detection steps represent the same system, it is assumed that a TC can have a translational velocity of at most 20 ms^{-1}.

The sensitivity to this velocity is explored in more detail in section 8. If the two TC centers are within a distance that is consistent with this assumption, they are deemed to be the same TC. Tracks are only retained if they reach a minimum life time (τ). Within this study, τ is always 18 hours, meaning that a TC track must endure for at least four consecutive detection steps. The minimum life time criterion is necessary to remove very short-lived false positives that frequently occur well within the extratropics.

This procedure results in a set of tracks for every parameter combination. These are then merged to form one final, singular set of tracks. To achieve this, every set is searched for instances of the same underlying TC, which typically has a variable track length as stronger constraints in the parameter thresholds produce shorter tracks than weaker constraints. Since the tracking algorithm aims to include weaker phases, the full length of these tracks is retained. To exclude probable false positives, the number of parameter combinations that identified an individual TC, regardless of the individual track length, as long as the minimum life time is fulfilled, is considered. Tropical depressions (TDs, see Table 3.2) are very weak systems, and are not easily identified. Thus, if 10% of all combinations identify a TD, it is retained. Tropical storms (TS) are more intense, but still weak compared to hurricanes. They are retained if at least 20% of all combinations identify the TC. Hurricanes are rather intense TCs, and are thus comparatively easy to identify. They are retained if at least 50% of all parameter combinations identify them. These values are subjectively chosen, based on visual inspection of azimuthally averaged wind and temperature fields of a subset of the considered TCs. While this introduces a fixed threshold again, the threshold value issue is reduced to one parameter, and this parameter does not describe the physical properties that the tracked system must exhibit.

The choice of the final parameter thresholds is tailored specifically to the underlying dataset. For use with other data, it is recommended that these values are revisited, and adapted if necessary.

As an important purpose of tracking TCs is to determine the activity within a season, the TC activity is quantified by the accumulated cyclone energy (ACE) (Bell et al., 2000). It is calculated as the sum of the squared maximum wind speeds of all TCs at either the TS or hurricane stage at 6-hourly intervals, i.e.

$$ACE = \sum_{i=1}^{k} v_{max,i}^2 \tag{3.1}$$

where v_{max} is the maximum wind speed of a TC at time i, which is documented every 6 hours until the end of the season (k). References to TC intensity follow the Saffir-Simpson hurricane wind scale Saffir (1973), slightly adapted to be consistent with commonly used modern values as seen in table 3.2. HURDAT2 data (Landsea and Franklin, 2013) are used to compare simulated ACE to observations.

The first and last detection steps of individual TCs are separated into a number of categories, which are described in table 3.3. These categories aid in evaluating how early TCs are tracked, and what causes them to terminate.

3.3 Tropical Cyclones in the Simulation Data

Validation of a TC tracking algorithm requires that the model producing the underlying data can represent viable TCs, at least to the extent that the features used in tracking are truly features of the simulated TC. Figure 3.1 shows the azimuthal mean radial and vertical wind and temperature anomaly of the most intense TC within the dataset, which was a category 4 TC. The reference temperatures to determine the temperature anomaly is the azimuthal mean vertical profile at 500 km distance from the center. The third row shows the TC at its high-

Category	Maximum Wind Speed [ms^{-1}]
TD	$v_{max} < 17$
TS	$17 \leq v_{max} < 33$
Cat 1	$33 \leq v_{max} < 43$
Cat 2	$43 \leq v_{max} < 50$
Cat 3	$50 \leq v_{max} < 58$
Cat 4	$58 \leq v_{max} < 70$
Cat 5	$70 \leq v_{max}$

Table 3.2: Saffir-Simpson Hurricane Wind Scale, where TD is a tropical depression, TS is a tropical storm, Cat 1-5 are hurricane categories 1-5, and v_{max} is the maximum instantaneous wind speed.

est intensity, and the second and first rows show the TC 24 and 48 hours prior to this, respectively.

The radial wind panels at all three shown times show inflow within the boundary layer, and outflow near the tropopause. This is a well documented feature, which has already been reproduced by very early numerical simulations, where the boundary inflow is recognized as a feature crucial to the TC (e.g., Ooyama (1969)). The boundary layer inflow is rather weak in comparison to that found in fig. 2 of Montgomery and Smith (2017), but as this is not immediately relevant to the tracking algorithm, this is not investigated further. An expected, though absent from our simulated TC, feature is a shallow region of outflow above the boundary layer (Smith and Montgomery, 2015), as supergradient wind is lifted above the boundary layer and adjusts to gradient wind balance. A further feature of radial wind that is expected following Willoughby (1988), but is absent from our simulated TC, is weak inflow throughout the mid-troposphere, which is linked to vortex stretching, and thus TC intensification. Vortex stretching is also linked to changes in vertical velocity with height. All three vertical wind panels show clear updraft regions throughout the vertical extent of the troposphere, beginning at a radius of about 50 km near the top of the boundary layer. The vertical wind speed increases with height in parts of this updraft region, which is indicative of vortex stretching. The panel at 24 hours before maximum intensity in particular shows a deep region of an increase in vertical velocity with height, which is reversed at a height of around 11 km. This reversal leads to a reduction in vorticity, which manifests itself as a reduction in tangential velocity (not shown), and is collocated with the outflow region. The missing mid-level inflow is thus not indicative of absent vortex stretching, as the vertical wind profile shows clear signs of vortex stretching. The eye of a well developed TC is characterized by subsidence, as shown in Montgomery and Smith (2017) for simulated TCs. While this is present at the time of maximum intensity, it is not present 24 hours earlier, and is not well developed 48 hours earlier. Possible causes for this are the general weakness of the subsidence, and the small scale of this phenomenon. Further, it has been found that increasing the horizontal resolution of numerical simulations beyond the resolution used in this study can affect the range of downdraft velocities (Gentry and Lackmann, 2010). Generally, the numerical simulations within this study have the capacity to produce the mean secondary circulation features of TCs rather well, even if the more intricate features of secondary inflow are not represented well. Notably, the numerical model can produce vortex stretching in the lower troposphere, which is relevant to the tracking algorithm as it requires a vorticity maximum.

The temperature anomaly panels for all three time steps show a distinct warm core at the center of the TC. The magnitude of the anomaly increases with increasing TC intensity, which is

Category	Occurrence	Description
Genesis Categories		
Single Maximum	36%	TCs exhibit a single vorticity maximum near the central sea level pressure minimum, or only very weak secondary maxima around a strong central maximum within the first 24 hours.
Transitional	34%	TCs exhibit multiple vorticity maxima near the central sea level pressure minimum, and transition to a single vorticity maximum, possibly with very weak local maxima around a strong central maximum, within 24 hours of first detection.
Multiple Maxima	19%	TCs exhibit multiple vorticity maxima near the central sea level pressure minimum within the first 24 hours.
Termination Categories		
Warm Core Offset	52%	The warm core offset relative to the central pressure minimum becomes too large to fulfill the warm core criteria.
Translation Velocity	27%	The translational velocity becomes too large for the algorithm to continue the constructed track.
Vanishing Pressure Minimum	4%	The central pressure minimum vanishes, and thus there is no local minimum to be tracked any longer.

Table 3.3: Description of genesis and termination categories with the occurrence rate of each category. The total number of tracked TCs is 113, about 12% of tracked TCs are false positives. Not all terminations fall under this categorization.

consistent with the findings of Durden (2013), and the temperature anomaly maxima fall within the height range of 760–250 hPa described therein. As is discussed in Stern and Nolan (2012), the altitude of the warm core can vary drastically, and multiple local maxima can coexist. They find that the most common altitude for the strongest warm core maximum is between 4 km and 8 km. Wang and Jiang (2019) found that the height of the warm core maximum increases with TC intensity, and typically ranges from 10 to 11 km for category 4 TCs. Therefore, the shown TC has a warm core at an acceptable height. The numerical simulations are thus concluded to have the capacity to produce warm core features that the tracking algorithm requires to distinguish tropical cyclones from extratropical cyclones.

Figure 3.2 shows all TCs of a single ensemble member, indicating their category and the percentage of parameter combinations that detected a given track segment. Tracks typically start at very low intensities, and with a lower percentage of threshold parameters detecting the system. The TS and hurricane stages are detected by more parameter combinations, as their structure is more developed. The parameter combinations with weaker constraints are therefore necessary to capture the early stages of TCs.

Figure 3.3 shows the accumulation of ACE throughout the season for HURDAT2 data and

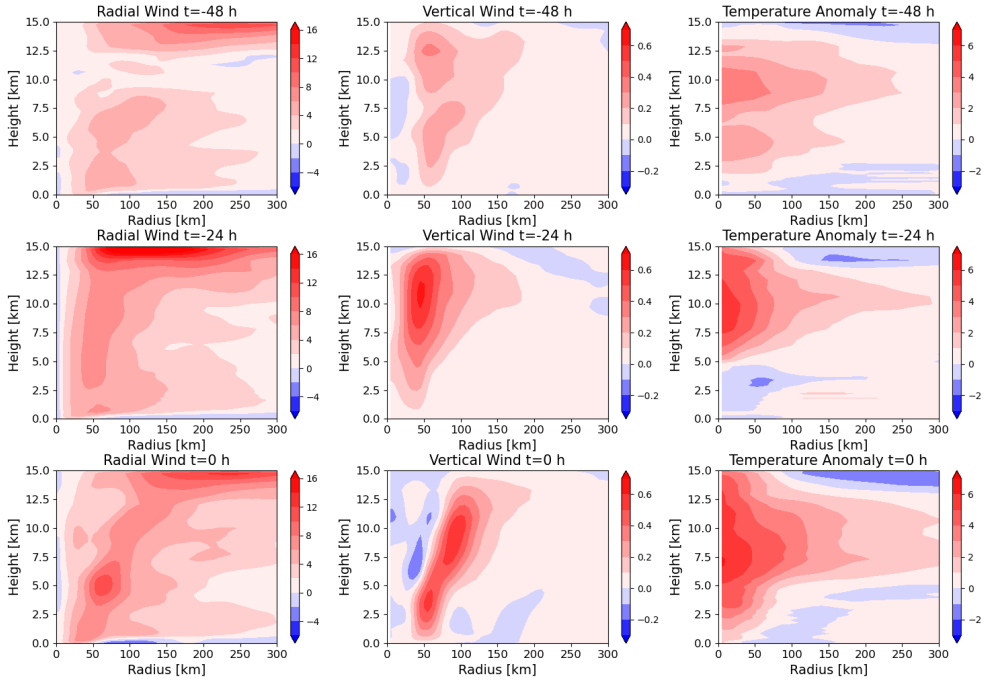

Figure 3.1: Azimuthal mean radial wind (first column), vertical wind (second column) and temperature anomaly (third column) of the most intense TC within the simulation dataset at its highest intensity (third row) and 24 (second row) and 48 (first row) hours prior.

for the 20 simulated ensemble members. While the simulations underestimate the TC activity early in the season, this is compensated with high activity during September, where most of the activity is concentrated. While most simulations eventually drastically overestimate ACE, it is important to note that the 2013 season was one of very low activity (see, e.g., Zhang et al. (2016) for a discussion of the low activity and its causes). Therefore, the simulations produce ACE values that are realistic compared to observed TC seasons.

3.4 Genesis Detection

The detection of tropical cyclogenesis is met with a fundamental problem: TCs typically form from a pre-existing disturbance, which gradually develops TC-like characteristics. This means that there is no clear distinction between the pre-existing disturbance and the developed TC. As the tracking algorithm aims to maximize the duration of a TC, how early a TC is detected is sensitive to how weak the most liberal threshold values are chosen. It is thus of interest to investigate how early in the life cycle of a TC the system is detected.

For all detected TCs, the first tracked 24 hours are divided into the three genesis categories listed in Table 3.3. As the number of TCs is not prohibitively high, this division is done manually to avoid possible oddities in the categorization that an algorithm could produce, though it does introduce some subjectivity. A total of 113 TCs across 20 ensemble members (i.e., about 5-6 TCs per simulation) are assessed, of which about 12% are false positives, which are discussed in section 6. The following figures show a detection percentage, which is the number of parameter combinations which identified the specific TC at the given time. The maximum of this percentage along the entire track is what the algorithm uses to decide whether a track is retained. The figures show the temporal evolution of this percentage throughout the first few time steps.

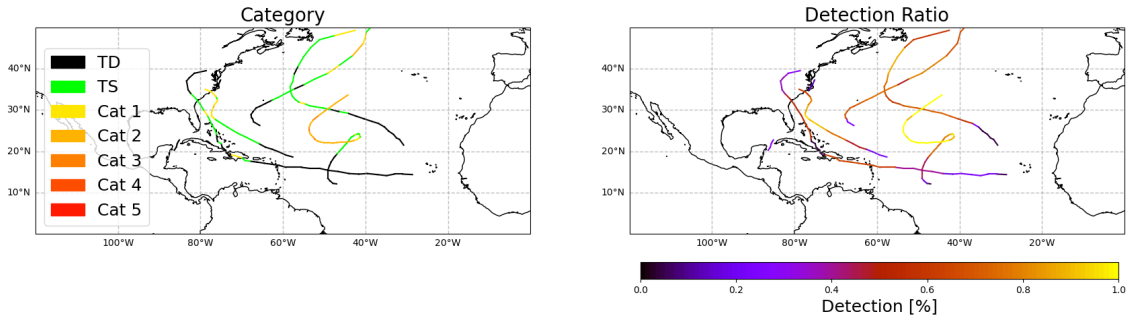

Figure 3.2: Tropical cyclones detected in a single ensemble member. The left panel shows their category, and the right panel shows the percentage of parameter combinations that detected a given track segment.

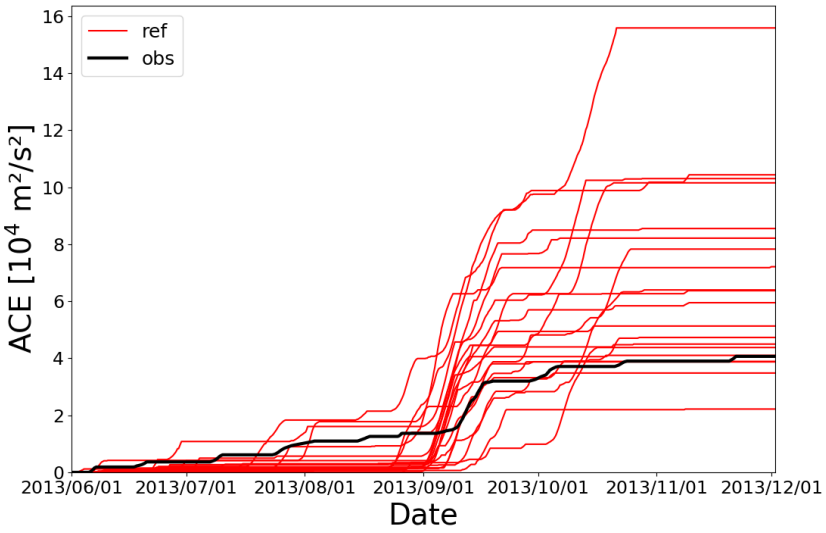

Figure 3.3: Accumulation of ACE throughout the season for HURDAT2 data (black) and the 20 simulation ensemble members (red).

Figure 3.4 shows a typical example of the single maximum category. This category requires a TC to exhibit a single vorticity maximum near the central sea level pressure minimum, or to have only very weak local vorticity maxima around a strong maximum throughout the entire 24 hour period. About 36% of all tracked systems fall within this category. The horizontal wind speed panels show an asymmetry in the cyclonic wind, which is due to the superposition of the cyclonic wind field and the translational velocity of the TC. Further, the wind speed at the center of the TC is very low, which is a result of the vanishing tangential wind speed towards the center. The TC thus has a developed cyclonic circulation. The vorticity panels, as per the categorization, show a strong central maximum, with comparatively very weak local maxima in the vicinity. The lack of a tracked aggregation phase is not necessarily indicative of a flaw in the tracking algorithm, as TCs can be generated from an extratropical precursor cyclone via tropical transition (Davis and Bosart, 2004), where the precursor cyclone attains TC characteristics. Tropical transition accounts for over a third of cyclogenesis events in the Northern Atlantic (McTaggart-Cowan et al., 2013). The algorithm only tracks these cyclones once the TC characteristics are sufficiently developed. This underlines the importance of the warm core criteria, which serve to distinguish extratropical cyclones from TCs. The temperature anomaly panels show a distinct warm core very close to the center in all three instances. After 24 hours, the warm core is offset to the southeast from the TC center. While the offset is not immediately relevant to first detection, it shows that the warm core criteria allow for some offset of the warm

core relative to the TC center without losing the ability to track the TC. The allowance for this displacement is sensitive to the warm core threshold parameters, which is reflected in the reduction of the detection percentage for this time step, in that the percentage is decreased for a more intense, but also more offset, core. This in turn shows that the detection percentage is not sensitive to TC intensity alone. The mean sea level pressure panels serve to show that the algorithm tracks a genuine low pressure system, and not a spurious local minimum. Notably, the low pressure system is still tracked when it is embedded in a larger scale pressure gradient, underlining the importance of a parameter that defines the region within which a point must constitute a local minimum.

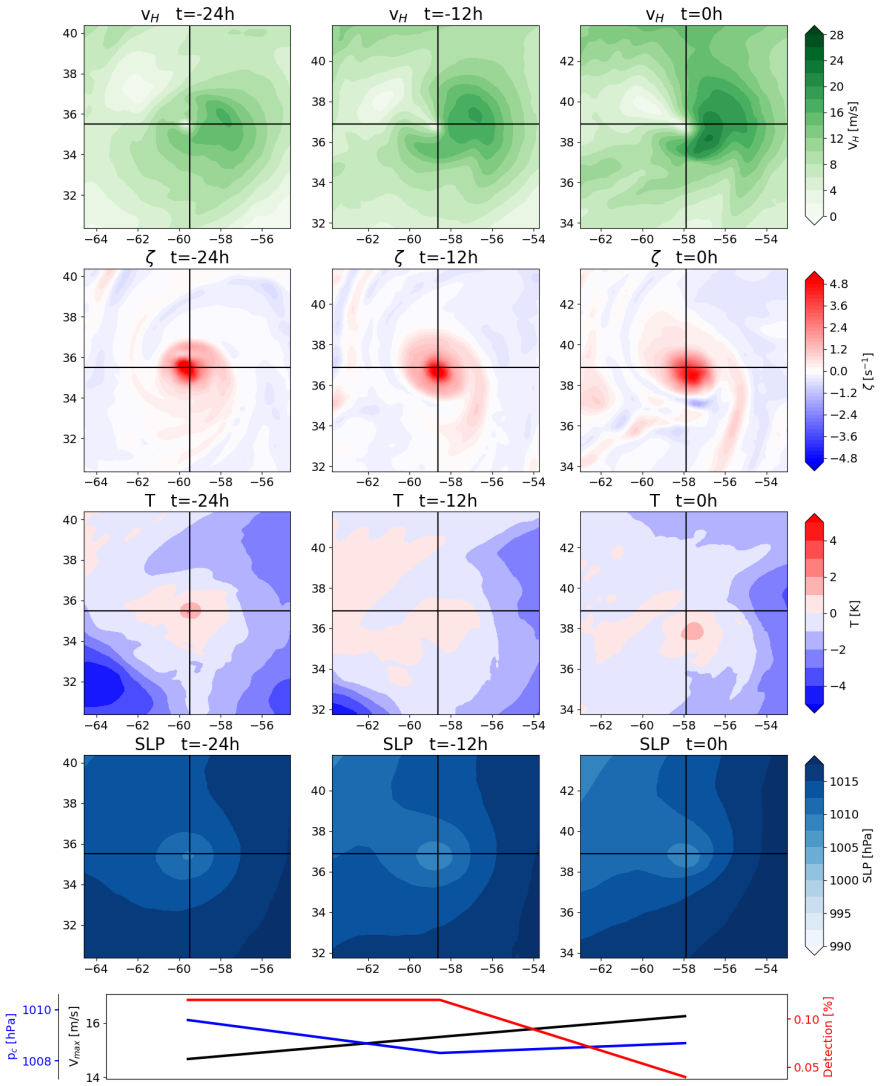

Figure 3.4: Example of a TC in the single maximum genesis category. 850 hPa horizontal wind magnitude (first row), 850 hPa vertical vorticity (second row), 300 hPa temperature anomaly (third row), mean sea level pressure (fourth row) and central pressure (blue), maximum wind speed (black) and detection percentage (red) at the three times shown (fifth row). The first column depicts first detection, the second column shows the TC 12 hours after first detection, the third column shows the TC 24 hours after first detection. Black cross-hairs indicate the TC center.

Figure 3.5 shows a good example of the transitional category, in that the first time step shows a number of local vorticity maxima of roughly equal magnitude spread throughout a sizeable region. This category requires that at first detection, there are multiple local vorticity maxima in the vicinity of the central mean sea level pressure minimum. Within 24 hours these must give way to a single vorticity maximum, possibly with comparatively very weak local maxima around it (i.e. it must transition into the pattern that the single maximum category requires from first detection on). This category thus captures TCs that complete an aggregation phase of mesoscale convective systems within the first 24 hours of detection. About 34% of all tracked systems fall within this category. A good example of this category is shown instead of a typical example for two reasons. First, this shows the situation that the variation of parameters aims to track more effectively. Second, the panels 12 hours after first detection show a situation that is reflective of a typical first detection in this category, such that a more typical situation is still captured by the figure. The wind field panels show a pattern similar to that of the previous category, where cyclonic flow is enhanced in the direction of translation, and reduced in the opposing direction. The location where the tangential velocity is drastically reduced close to the center is slightly offset from the mean sea level pressure minimum, which is typical for the tracked TCs within this category. Once the transition to a single vorticity maximum is completed, this offset typically becomes very small or vanishes entirely. The vorticity panels show many local maxima of comparable intensity at first detection. In this stage, a key component to the production of vertical relative vorticity is the stretching of pre-existing vertical vorticity. Examination of the vertical wind speeds shows that the vorticity maxima are located where the vertical wind speed increases with height (not shown), which strongly suggests the presence of vortical hot towers, as discussed in Montgomery and Smith (2014), or at the very least strong generation of vertical vorticity through vortex stretching. Therefore, the algorithm appears to be tracking the aggregation stage of mesoscale systems, which then develop into a TC. The algorithm thus successfully fulfills the goal of capturing this stage for about a third of all tracked systems. However, typically this stage is only detected when the aggregation has progressed substantially, as the panels depicting the TC 12 hours after first detection are more typical for this category. The warm core intensifies throughout the aggregation period, and the location of the maximal temperature anomaly moves closer towards the center of the TC. These two factors cause the detection percentage to increase drastically from the first to the second panel. This shows that the early aggregation phase is within a range where the warm core parameters are crucial to detection, and the thermal structure of the TC must show some organization. The sea level pressure panels show that the algorithm can track low pressure systems that are rather weak, as is required for capturing the aggregation phase. The maximum wind speed at first detection is close to TS strength in this example, but can be around 10 ms^{-1} in other examples. This low maximum wind speed reflects the early detection in the non-aggregated state. The maximum wind speed as tracked by the algorithm is not identical to the maximum wind speed seen in the figure. This is because the algorithm only searches for the maximum wind speed within 100 km of the TC center to ensure that there is no false inclusion of winds outside of the TC circulation. The maximum wind speed can therefore be underestimated for TCs with a very large radius of maximum winds. Hence, this constraint on the maximum radius of maximum winds should be revisited for use with other datasets.

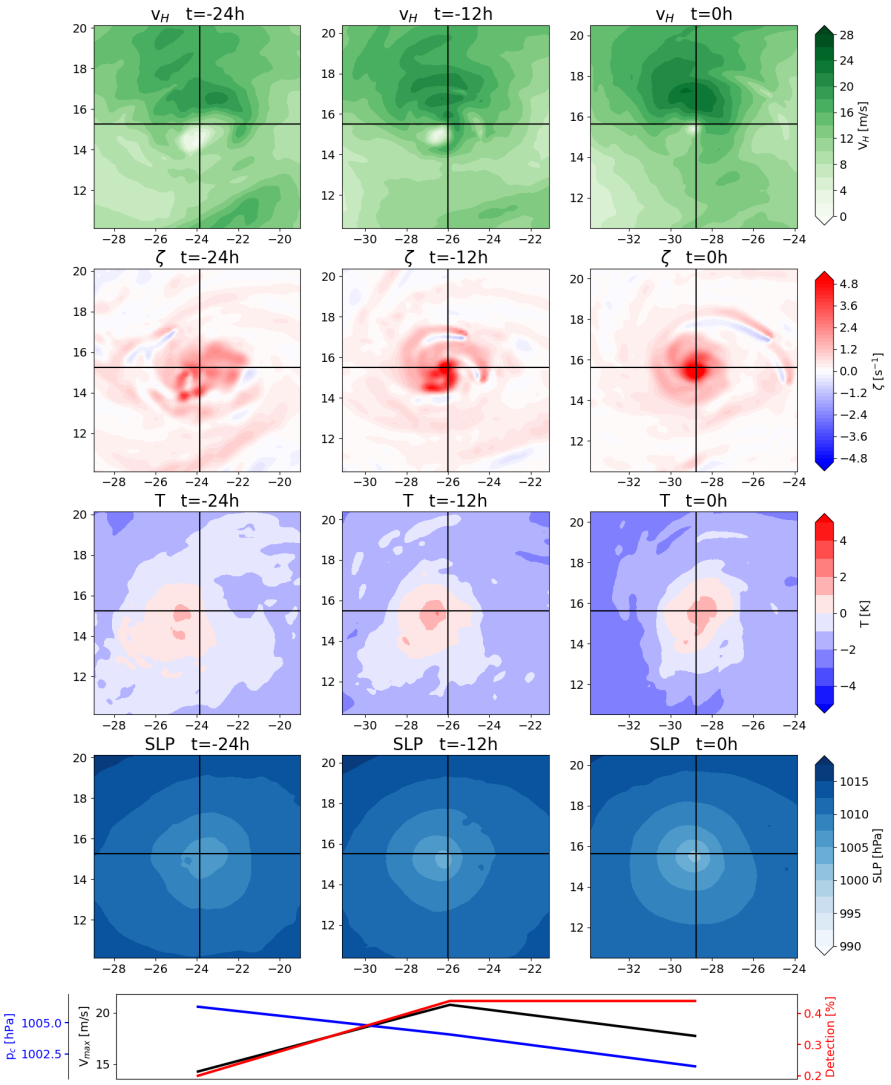

Figure 3.5: As fig. 3.4 for a TC in the transitional genesis category.

Figure 3.6 shows a typical example of the multiple maxima category. This category requires that there are multiple vorticity maxima throughout the first 24 hours of the TC, and that there is no singular maximum that is substantially stronger than the others. About 19% of all tracked systems fall into this category. The wind field panels differ substantially from those shown for the previous two categories. While the very low wind speeds at the center still indicate cyclonic rotation, this is not evident from the winds further away from the center. The cyclonic rotation is thus rather weak, and obscured by environmental winds. This calls into question the usefulness of a maximum wind speed metric, but it will be shown below that these early phases barely impact ACE. This particular example develops into a category 1 hurricane about one week later, which has a much larger impact on ACE. The vorticity panels show only few vorticity maxima, but these increase in number throughout the first 24 hours. This could be due to more VHTs forming, which locally stretch vorticity and aggregate later on. This implies that TCs of this category are detected very early in their life cycle, which is intended. The warm core is barely developed at first, but intensifies throughout the first 24 hours. However, there is no single central maximum, but rather a few local maxima emerge. This unstructured warm core is reflected in the detection percentage, which is barely high enough to not discard this stage of the life cycle. The warm core criteria are thus capable of detecting systems early on, but are not liberal enough to track any low pressure system with mild diabatic heating. It appears that a substantial region of increased temperature is required for the tracking algorithm to detect a TC, especially when the increased temperature is offset relative to the TC center.

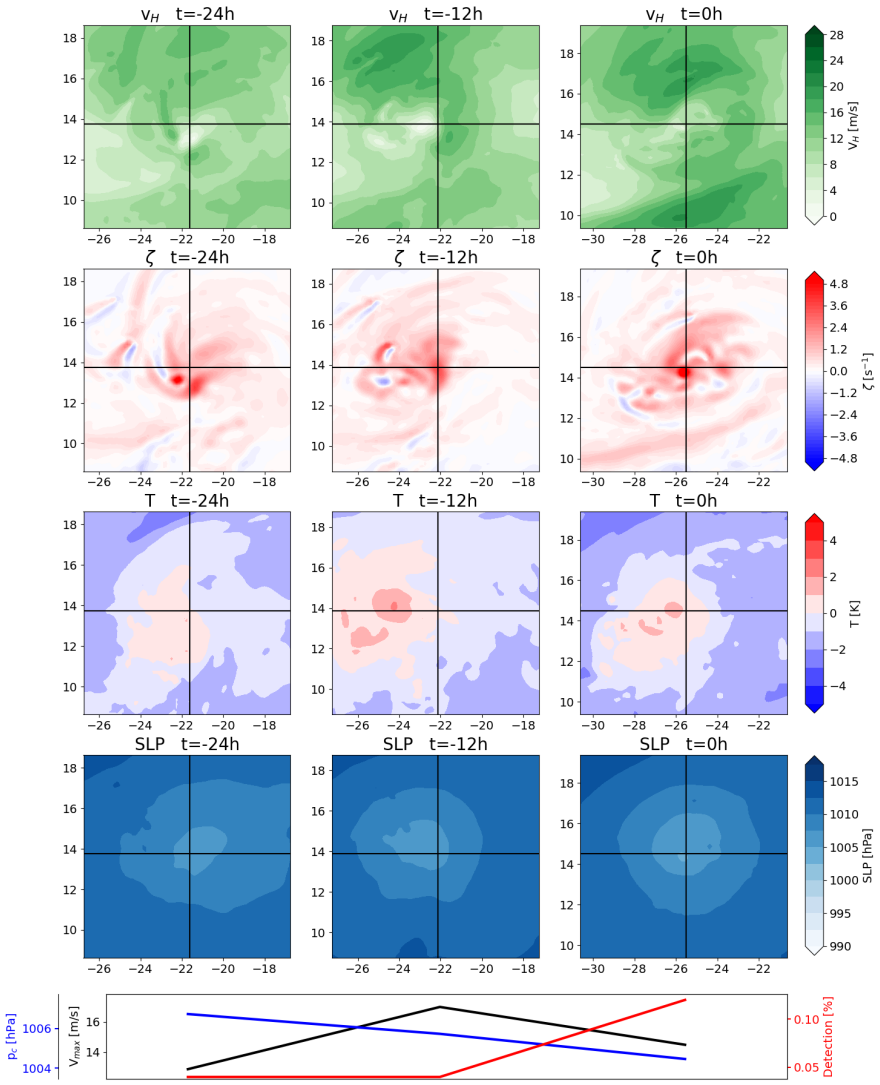

Figure 3.6: As fig. 3.4 for a TC in the multiple maxima genesis category.

3.5 Tropical Cyclone Termination

The termination of a TC is, much like genesis, not strictly defined. Therefore, it is investigated what the tracking algorithm deems to be the last time step at which a TC exists, and why it is not tracked further. The algorithm ceases to track a system when the surface pressure minimum disappears, vorticity becomes too weak, the warm core can no longer be detected, or the translational velocity is too large to construct a track. Within the used data set, three main causes for TC termination have emerged: (i) The TCs either have a warm core that is offset in a way that increases the environmental temperature such that the warm core criterion is no longer fulfilled, (ii) the warm core weakens substantially, or (iii) the TC moves too fast to be connected to previous detection steps. Typically, at least two of these processes occur in parallel. The following figures resemble those of the previous section, but now span only the last 6 hours of the TC in the first and second column, and a third column shows plots 6 hours after the TC is last tracked, centered on the final TC position. Mean sea level pressure contours are overlaid on the horizontal wind magnitude, vorticity and temperature anomaly filled contours to better identify where the pressure minimum is located relative to features within these plots. The temperature anomaly within the figure (not during the actual tracking) is calculated using a 4°x4° square centered on the center of the cross-hairs as a reference, as this is somewhat reflective of how the temperature anomaly is calculated by the tracking algorithm.

Figure 3.7 shows an example of a TC where the tracking algorithm finds a pressure minimum with sufficient vorticity, but where the warm core is offset relative to the pressure minimum, and the warm core is weakening in intensity. The wind magnitude panels show a cyclonic wind field around a pressure minimum even after the TC is no longer tracked, and the vorticity panels show that there is sufficient vorticity to fulfill the vorticity criterion at all times. In the third column, the distance between the pressure minimum and the last tracked position is also well within the permissible distance that would allow for a track to be constructed. Therefore, the TC must be terminated by the warm core criteria no longer being fulfilled. This is because the weakening warm core is positioned east-south-east of the pressure minimum, and some distance away from it. The pressure minimum is thus located towards the edge of the warm core. This combines a rather weak anomaly above the pressure minimum with an environmental temperature that is heavily impacted by the presence of the warm core, such that no warm core is detected. The weakening warm core throughout this period is not directly visible in the figure because the reference temperature is progressively reduced, but the absolute temperature of the maximum does indeed decrease, and the area of elevated temperature decreases as well. This aids in offsetting the warm core location from the pressure minimum, as the area of strong temperature anomaly is reduced. This scenario is the most common, with about 52% of cases terminating due to an offset of the warm core position.

Figure 3.8 shows an example where the TC has a translational velocity that is too large for a track to be constructed. While between the last two tracked steps the TC moves about 3° to the north and 2° to the east, the TC then accelerates and moves about 4° to the north and 3° to the east. This makes it too fast for a track to be constructed. The wind field panels indicate that there is still cyclonic rotation around a pressure minimum, and the vorticity panels show that there is still strong vorticity associated with the TC. The warm core criteria also seem to be fulfilled. However, a feature that is typical for such cases is that there is a strong environmental temperature gradient, and cold air enveloping the TC in a cyclonic fashion. This is indicative of extratropical transition (Evans and Hart, 2003), which may also be the cause for the increasing asymmetry in the vorticity field surrounding the TC. The intensity of the warm core is substantially reduced within the shown 12 hour window, which is consistent with the erosion of a warm core during extratropical transition. Therefore, it appears that TCs that have a too high translational velocity tend to be TCs that are interacting with extratropical flow and are undergoing extratropical transition. While it is reasonable to exclude transitioned TCs, the precise moment where tracking is terminated is not controllable with this algorithm. Further, the tracks do not

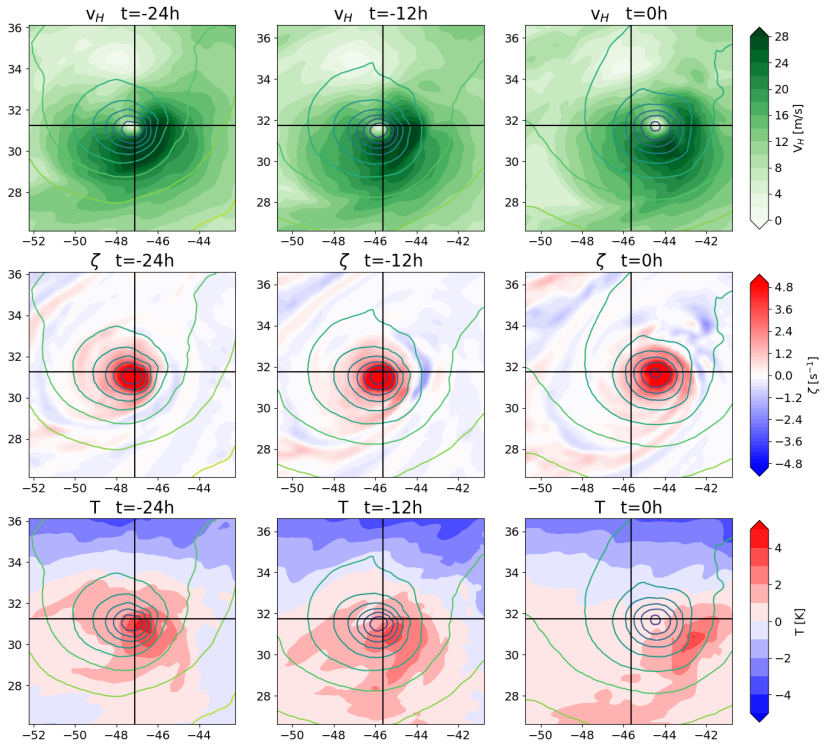

Figure 3.7: Example of a TC in the warm core offset termination category. 850 hPa horizontal wind magnitude (first row), 850 hPa vertical vorticity (second row), 300 hPa temperature anomaly (third row), with overlaid mean sea level pressure contour lines. Black cross-hairs indicate the tracked TC center for the first two columns, and the last tracked TC center (i.e. that of the second column) for the third column.

terminate explicitly because of the transition process, but because the TCs accelerate, making this termination scenario convenient, but accidental. About 27% of TCs terminate due to a too large translational velocity.

For more control over the termination of a track (or the continued tracking, but with appropriate labeling) due to extratropical transition, it may be beneficial to explicitly treat extratropical transition. Bourdin et al. (2022) and Bieli et al. (2020) both describe methods based on the definition of extratropical transition provided in Evans and Hart (2003) to distinguish between tropical and extratropical cyclones. The explicit treatment of extratropical transition is currently not implemented in the scheme here, but will be the focus of possible future improvements.

Far less common is the vanishing of the sea level pressure minimum. This occurs when a substantially larger low pressure system absorbs the local pressure minimum, which causes the TC to weaken and its pressure minimum to vanish towards the edge of the larger low pressure system. This is the case for 4 TCs within this data set. There is one TC that approaches the eastern boundary of the domain at 15°W, where it weakens and is eventually no longer tracked. Due to the proximity to the boundary, it is not counted in any of the other categories.

In conclusion, tracked TCs reliably terminate due to the erosion or offset of the warm core, due to interaction with extratropical flow, or due to the vanishing local pressure minimum at their center. The translational velocity criterion aids in terminating TCs when they interact

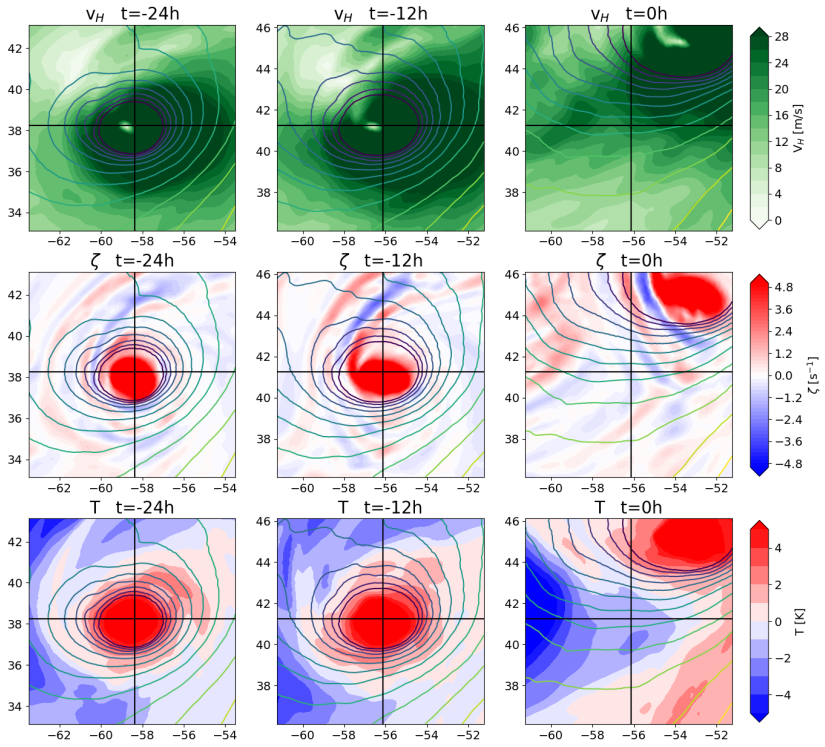

Figure 3.8: As fig. 3.7, but for a TC in the translational velocity termination category.

with extratropical flow, even when the warm core is still present. While this is convenient, as TCs terminated in this manner show strong asymmetry instead of the typical radial symmetry of a TC, it is not intended and not controllable by parameter choice. The maximum translational velocity parameter serves to form tracks out of individual detection steps, and must be chosen to fulfill that function. It can therefore not be chosen freely and adapted to optimize its function as a termination criterion.

3.6 False Positives and Other Tracking Issues

Naturally, there are limitations to the tracking algorithm. Other than beginning to track TCs too early or terminating them too late, there are also instances of tracked systems that cannot feasibly be considered TCs. About 12% of all tracked systems are false positives. Almost all of these cases show traits of extratropical cyclones, which is consistent with Bourdin et al. (2022), who found false alarms to frequently be caused by extratropical cyclones. Edge cases are mostly eliminated by the life time criterion of the algorithm. Figure 3.9 shows a typical example of such a case. The wind field at all shown times shows an elongated band of high wind speeds, but no central minimum. There appears to be no discernible center of cyclonic flow near the track center, indicating that the wind field is inconsistent with the existence of a TC at this location. The vorticity fields at all shown times further substantiate this, as elongated bands, partially with alternating signs, are inconsistent with a developed TC, and also inconsistent with the aggregation of local maxima caused by vorticity stretching as seen in previous examples. The temperature fields do not show warm cores, but positive anomalies in an environment with a strong temperature gradient. The presence of strong negative anomalies reduces the environmental temperature sufficiently for the algorithm to detect what it believes to be a warm core, as the positive anomaly at the center does not need to be pronounced or confined to a small

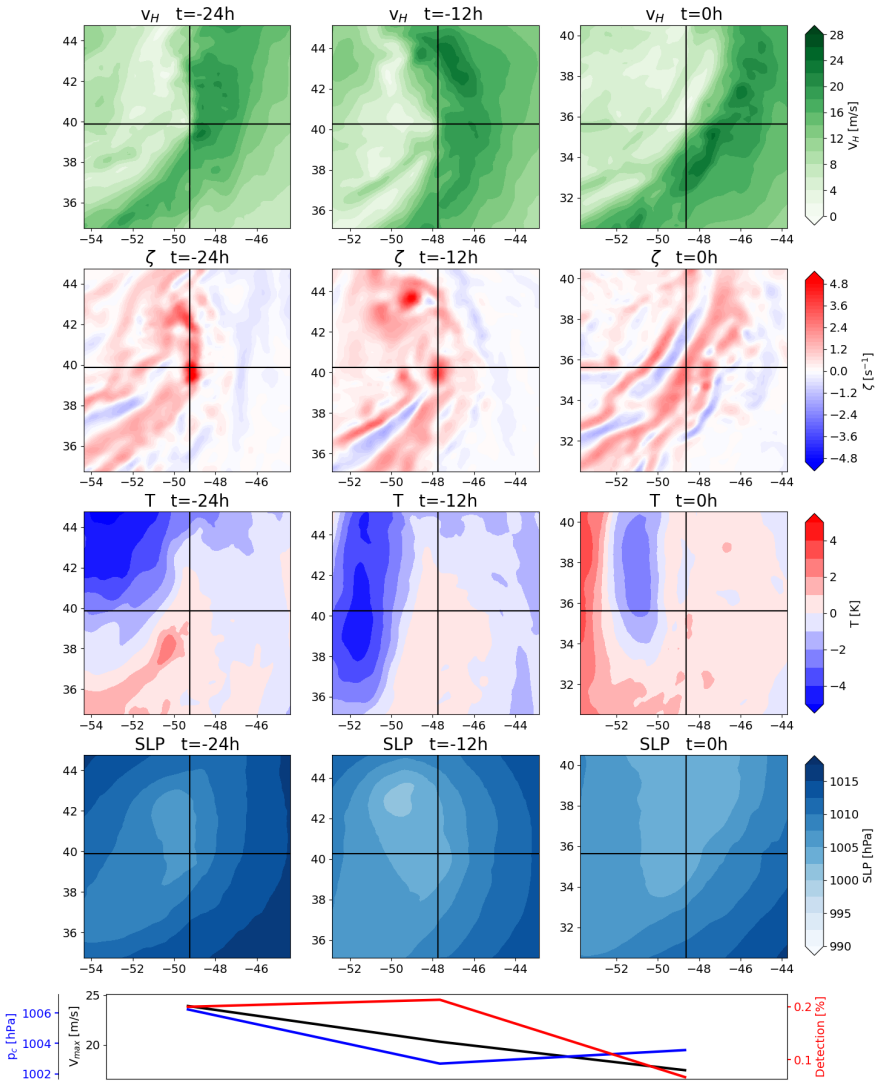

Figure 3.9: As fig. 3.4, but showing a falsely tracked frontal structure.

region to be above the environmental mean temperature. The sea level pressure fields show that the center of the tracked system is not where the pressure minimum of the low pressure system is located. Instead, the distance from the true pressure minimum of the system increases with time. It is thus concluded that the algorithm can mistakenly track frontal structures in extratropical cyclones, as these can show a local pressure minimum, sufficient vorticity, and a strong temperature gradient that technically fulfills the warm core criterion, even though it is not a true warm core. Other, atypical cases of false positives are local pressure minima with some positive vorticity that are in an environment with a strong temperature gradient, which fulfills the warm core criterion even though no true warm core is present.

Outside of false positives, it is possible for the algorithm to detect a TC, but to falsely identify first detection. Figure 3.10 shows a case where first detection is close to the TC's true location. At first detection, the minimum in the wind field that indicates the center of the cyclonic rotation is some distance away to the northeast, as is the vorticity maximum. As the vorticity maximum is rather broad, and only a few spurious and comparatively weak local maxima are located outside of it, there appears to have been an aggregation phase prior to detection. The sea level pressure shows a minimum close to the wind speed minimum and vorticity maximum

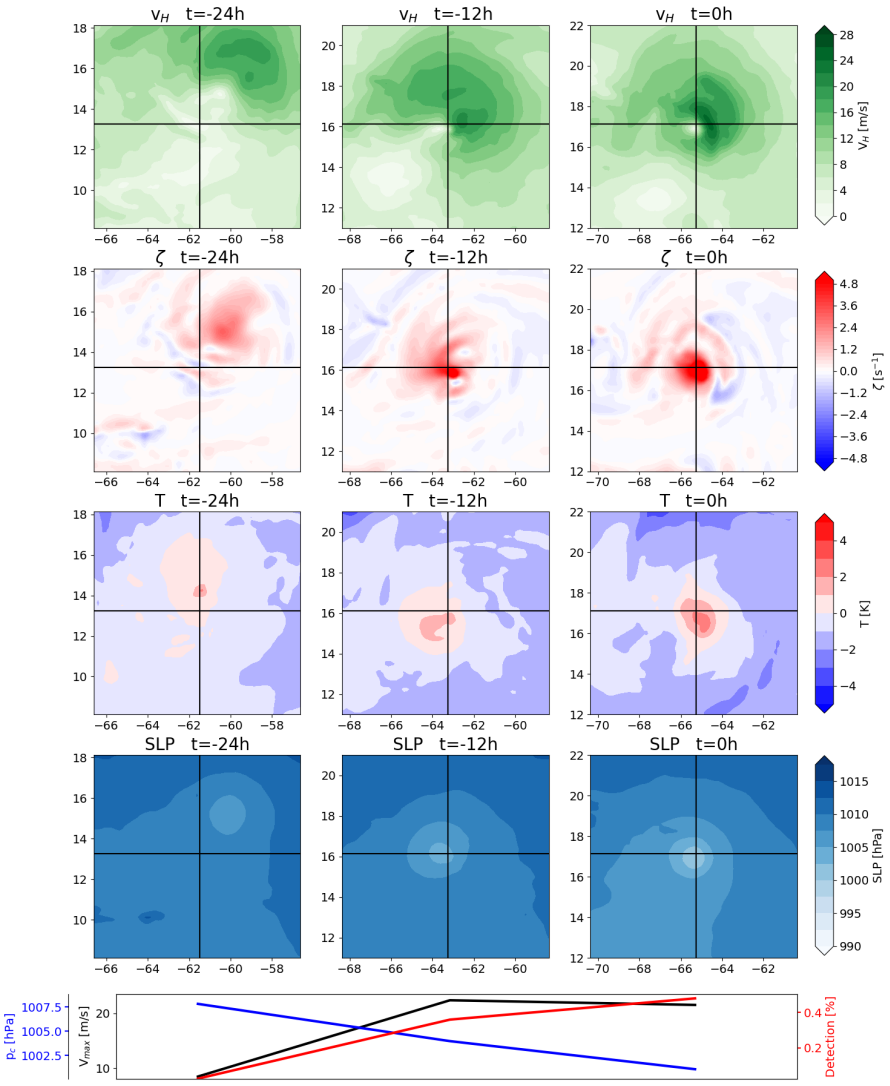

Figure 3.10: As fig. 3.4, but showing a falsely tracked initial location.

to the northeast of the tracked center. In the following detection steps the system is tracked correctly. This false tracking is likely caused by the pressure minimum to the northeast of the first detected point not fulfilling the warm core criteria. A local minimum outside of this - the falsely tracked center - fulfills all criteria in what appears to be a single or at most two parameter combinations, as indicated by the very low detection percentage at this time. This falsely tracks a system earlier than it otherwise would be at a location that does not reflect where the system is located. It should be noted that this is the only case within this data set where first detection of a TC is at the wrong location.

Similar to falsely identifying the beginning of a TC, it is possible for the algorithm to detect a TC correctly, but to then not terminate it early enough. Figure 3.11 shows a case where a legitimate TC is detected, but the algorithm then detects a local pressure minimum adjacent to a stronger low pressure system. This local minimum has sufficient vorticity to fulfill the threshold requirement, and is in a region with a sizeable temperature gradient. This allows the system to fulfill the warm core criterion without having a warm core, causing the algorithm to continue to track a system beyond extratropical transition. Two such cases exist within the used data set.

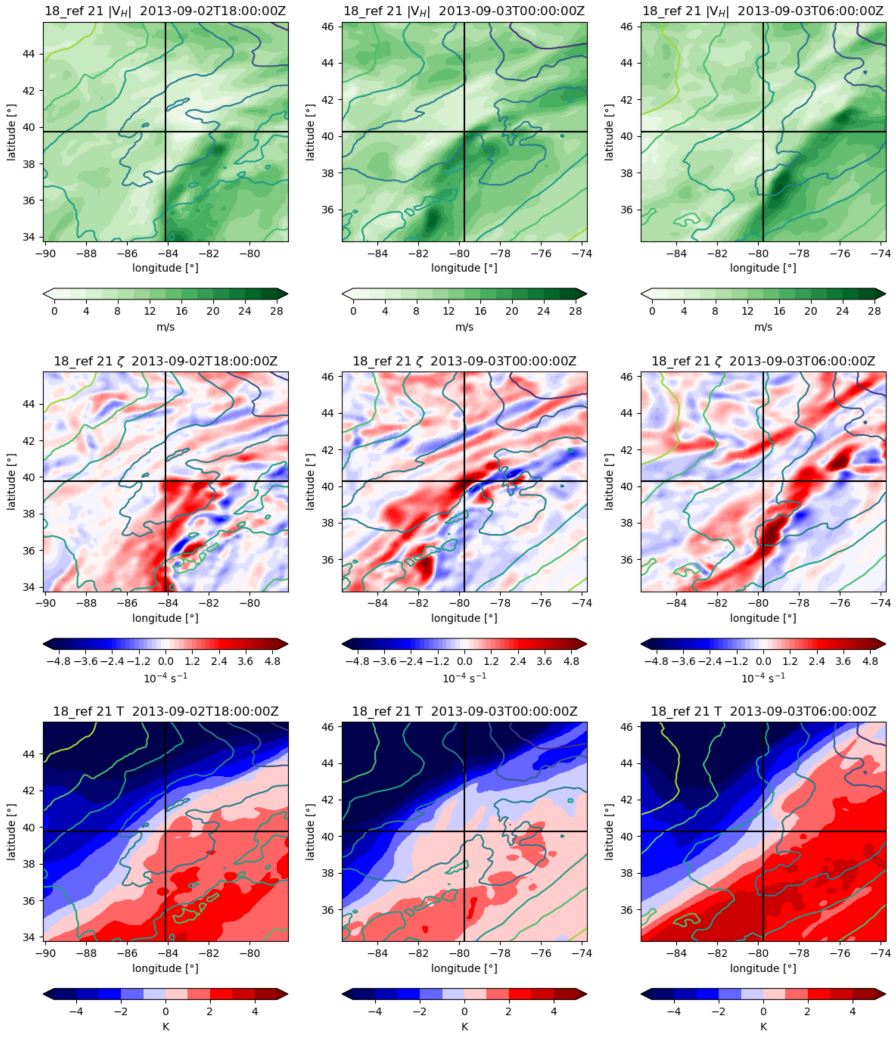

Figure 3.11: As fig. 3.7, but showing a false continuation of a TC that no longer exists.

In conclusion, there are features tracked by the algorithm that are not TCs, and TCs are not always tracked correctly. False positives are rather rare (about 12% of all tracked systems). The impact of these errors on ACE is explored in the following section.

3.7 Tracking Error Impact on ACE

Within this thesis, the main metric used to describe tropical cyclone activity is ACE. To determine the effect of tracking errors on ACE, a few different ACE calculations are considered. Figure 3.12 shows box plots of the 20 ensemble members comparing the different calculations. The first is full ACE, which includes all TCs at stages of TS strength or higher, including the false positives. This distribution is used as a reference for the following three. The second calculation is the same, but excludes all manually identified false positives. A one-sided t-test is performed to determine whether the distributions differ significantly, and the resulting p-value is 0.54. Therefore, there is no significant effect on ACE when false positives are included in the calculation. This is likely because the identified false positives typically have short lifetimes, and are not very intense, and therefore do not contribute substantially to ACE.

The third calculation includes all TCs at stages of TD strength or higher. The underlying rationale is that extending the tail ends of the tracks, and having varying track lengths depending on tracking parameter threshold choices, could impact the energy produced by individual TCs, which would not be captured by the regular ACE calculation. However, a one-sided t-test yields

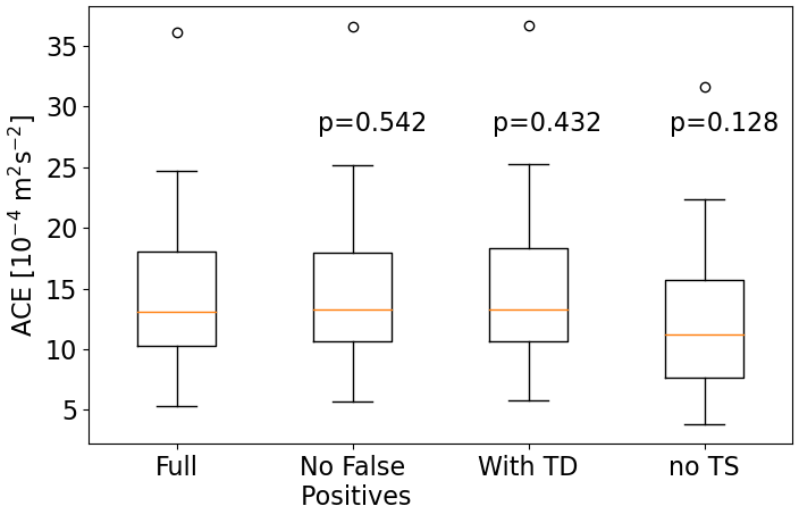

Figure 3.12: Box plots of ACE with the p-values of a one-sided t-test that assesses the difference of the means of various ACE calculations.

a p-value of 0.43, which shows that no significant difference is produced by the inclusion of the TD stage. The track extension of the parameter combinations with weak constraints thus allow for very early stages in TC development to be tracked without significantly affecting the energy produced by individual TCs.

The fourth calculation only includes the hurricane stage of TCs. This is done to show that extending the tail ends of TCs does not significantly impact the ACE contribution of individual TCs. In principle, the algorithm could extend the lifetime of TCs for too long, or could track them too early. As shown previously, this could be an issue when extratropical and tropical transition are involved, as there is no explicit treatment of these processes. Removing all TS stage data from ACE is an estimate for an upper bound of the impact this could have, which is intentionally chosen to be overestimated. A one-sided t-test yields a p-value of 0.13, meaning that the difference is not significant at the 90% level. Therefore, even if all tracks included TS stage data due to some flaw of the algorithm, ACE would still be adequately represented. This is especially the case when considering that the presented scenario is intentionally chosen to be an upper bound, and that most TS stage data truly reflect a TS in the data.

The results of Zarzycki and Ullrich (2017) show that ACE is less susceptible to changes when parameter thresholds are varied, which is comparable to the results presented here. Here, it is shown that ACE does not vary significantly when TD and TS strength systems are included or excluded. These systems are used to provide upper bounds for the impact of false positives and longer tails of tracks. It is suspected that the underlying reason is that ACE is dominated by intense TCs, and that parameter threshold variation primarily affects weaker stages of TCs (as shown in fig. 3.2). This hypothesis is supported by Bourdin et al. (2022), who found that in their comparison of different tracking schemes, strong cyclones are generally found by all compared schemes, and weak cyclones are more susceptible to not being found by all.

The impact of flaws in the tracking algorithm on ACE is thus concluded to be negligible, and the extension of the tail ends of tracks does not significantly increase the total energy produced throughout the full life cycle of individual TCs. The tracking algorithm is concluded to be capable of adequately capturing ACE within the underlying data.

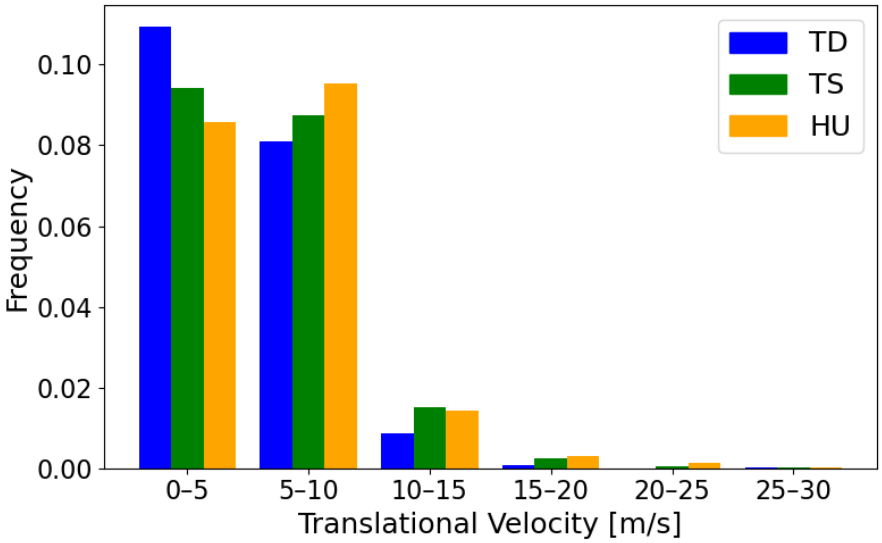

Figure 3.13: Normalized histogram of translational velocity of HURDAT2 systems for tropical depressions (TD, blue), tropical storms (TS, green) and hurricanes (HU, red).

3.8 Sensitivity to Translational Velocity

It has long been known that interaction with extratropical flow can accelerate the translational velocity of TCs undergoing extratropical transition (e.g., Krueger (1954); Palmén (1958)). This circumstance can accidentally, though conveniently, terminate TCs at some point during extratropical transition via the maximum translational velocity criterion. This may cause the choice of the maximum translational velocity to be more impactful than intended. Therefore, the sensitivity to this threshold is investigated.

The maximum translational velocity threshold used for the preceding analyses is 20 ms^{-1}. Figure 3.13 shows histograms of the translational velocities of HURDAT2 systems of TD, TS and hurricane (HU) categories. This velocity is calculated as the great circle distance between the TC's current location, where the categorization is made, and the location 6 hours prior, divided by six hours. Non-synoptic times are not considered.

The histograms show that it is extremely rare for observed TCs to move at a mean velocity of 15 m/s or faster. The TC tracking algorithm is thus applied three times, with the maximum allowed translational velocity set as 15, 20 and 25 m/s, respectively. Figure 3.14 shows the corresponding box plots. There is an increase in ACE with an increase in maximum translational velocity, as a relaxation of this parameter naturally constructs longer tracks. However, with p-values of 0.60 and 0.32 for the 15 m/s and 25 m/s cases, respectively, there is no significant difference in the distribution of ACE. An increase in the maximum translational velocity inherently bears the risk of introducing erroneous tracking, and therefore an increase beyond 20 m/s does not seem necessary or appropriate. A reduction to 15 m/s appears to be feasible, but fig. 3.13 shows that there are still a few observed TCs with a mean velocity above 15 m/s. Therefore, using 20 m/s appears to be the most appropriate maximum translational velocity.

3.9 Conclusions

A tracking algorithm for tropical cyclones was developed for use with ICON output data. The algorithm successfully tracks tropical depression, tropical storm and hurricane strength systems. About 36% of TC tracks begin with a strong central vorticity maximum, and about 34% begin with an aggregation of multiple vorticity maxima, in line with the VHT theory of TC cyclogenesis (Montgomery and Smith, 2014). About 19% of TC tracks begin with an ongoing aggregation

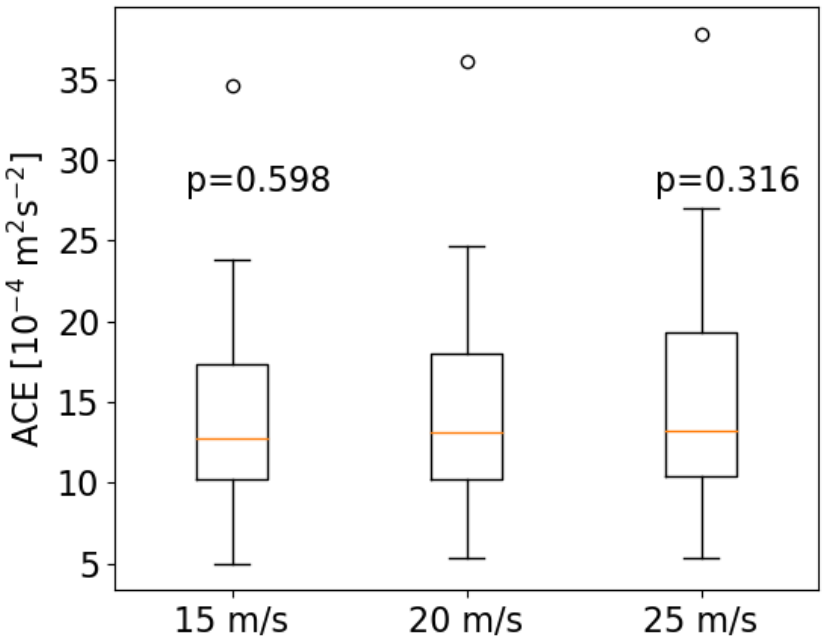

Figure 3.14: Box plots of ACE with the p-values of a one-sided t-test that assesses the difference of the means of ACE using different maximum translational velocities.

process, and remain within this process for at least the first 24 hours. About 12% of tracked systems are false positives.

The benefit of threshold parameter variation is apparent in the tracking of weak systems, especially at early stages of the TC life cycle. In particular, the relaxation of the warm core criterion allows for a larger distance between the warm core temperature anomaly maximum and the sea level pressure minimum. This distance becoming too large is the leading cause of track termination in TCs that are weak, but could feasibly be tracked for longer. However, it also allows for structures that are not warm cores to be falsely tracked. This is evident from the about 12% false positives, but also in TC termination, where a wrongful continuation of a system can be tracked. As the use of the OWZ parameter is particularly useful in detecting cyclogenesis, a comparison between the threshold parameter variation and the OWZ parameter for tracking early stages of a TC may be in order. Joint use of the two methods could be feasible. Variations in the vorticity threshold do not seem to be of much importance, as TCs that are tracked typically fulfill even the most strict vorticity criterion. A threshold of 10^{-6} s^{-1} could thus be sufficient, as this constrains the resulting tracks to those with positive vorticity.

Specifically for weak TCs, the maximum wind speed is often underestimated. This is because they often have a radius of maximum winds that is larger than the maximum radius within which the algorithm determines maximum wind speeds. An increase in radius may provide more accurate results, though care needs to be given to not accidentally include winds that are not part of the TC. It is possible that using a variable radius threshold based on central pressure could be beneficial, as weak TCs in particular are affected. However, a more accurate detection of TC genesis should precede this to provide a more solid basis for the exact nature of the radius variability.

The warm core criteria are central to discriminating between TCs and other low pressure systems. They are also responsible for most track terminations. Therefore, these criteria in particular need to be refined. Within the used data set, strong environmental temperature gra-

dients have caused the warm core criteria to be fulfilled even in the absence of a warm core. A possible solution to this would be to not only use the environmental mean temperature as a reference, but to introduce an additional requirement of having to reach a minimum positive anomaly within every quadrant. This would cause the criterion to not be fulfilled when one side of the detected system is substantially warmer than the other side, i.e. when a strong environmental gradient is present. Further, the offset of the temperature anomaly maximum from the pressure minimum could be treated explicitly. This could consist of introducing a new threshold parameter which determines the maximal allowed distance between the two extrema, and could be made dependent on the central pressure, as this is particularly relevant for weak systems.

While cyclones could be detected and tracked by a dedicated algorithm for extratropical cyclones after the transition, there is no guarantee that this does not result in gaps between the tropical and extratropical stage of cyclones during the transition. A further possible addition to the algorithm would therefore be an explicit treatment of extratropical transition. Currently, this process is only included via the warm core criteria, which is not only immensely inelegant, but also allows for no control over how this process is tracked. A clear definition of the transition process is given in Evans and Hart (2003), and Bieli et al. (2020) and Bourdin et al. (2022) both provide useful methods to implement this capability.

Furthermore, the effect of tracking errors on ACE has been investigated. The false positives appear to only have a minor impact on ACE. A hypothetical case where all detections of TD and TS strength systems are false is used to show that even if this were the case, the impact on ACE would be insignificant. Therefore, the ACE value calculated from the tracking algorithm output is concluded to reflect the true ACE value within the simulation data. Changes to how cyclogenesis is being tracked can thus be made without substantially impacting ACE. Explicit treatment of the extratropical transition process might have a larger impact, as these systems can still have somewhat high wind speeds, and extratropical transition occurs frequently.

Chapter 4

Influence of Potential Vorticity Structure on North Atlantic Tropical Cyclone Activity

Bernhard Enz[1], David Neubauer[1], Michael Sprenger[1] and Ulrike Lohmann[1]

[1]Institute for Atmospheric and Climate Science, ETH Zurich, Zurich, Switzerland

This work has been submitted to Journal of Climate, and is currently in revision.

Abstract

Tropical cyclones are among the most devastating natural phenomena that can cause severe damage when undergoing landfall. In the wake of the poorly forecast 2013 North Atlantic hurricane season, Rossby wave breaking on the 350 K isentropic surface has been linked to tropical cyclone activity measured by the accumulated cyclone energy (ACE). Here, ERA5 reanalysis data and HURDAT2 tropical cyclone data are used to argue that the latitude of the 2 potential vorticity unit (PVU) contour on the 360 K isentropic surface in the western North Atlantic is linked to changes in vertical wind shear and relative humidity during the month of September.

A more equatorward position of the 2 PVU contour is shown to be linked to an increase in vertical wind shear and a reduction in relative humidity, as manifested in an increased ventilation index, in the tropical western North Atlantic during September. The more equatorward position is further linked to a reduction in the number of named storms, storm and hurricane days, hurricane lifetime, and number of tropical cyclones making landfall. Changes in genesis location are shown to be of importance for the changes in landfall frequency and hurricane lifetime. In summary, the 2 PVU contour latitude in the western North Atlantic can therefore potentially be used as a predictor in seasonal and sub-seasonal forecasting.

Significance Statement

Forecasts for the North Atlantic hurricane season are operationally produced. Their aim is to predict the number of tropical cyclones and their total energy throughout the season. This study proposes to include the tropopause latitude in these forecasts, as it is shown to be linked to vertical wind shear and mid-tropospheric relative humidity in the western tropical North Atlantic. The tropopause latitude is thereby linked to the number of tropical cyclones, their lifetime and the total energy throughout the season. This link is particularly strong during September.

4.1 Introduction

Tropical cyclones (TCs) have the potential to lead to a loss of life and cause massive damage when making landfall. The damage is likely to increase with a larger and wealthier population concentrated in coastal areas (Pielke Jr. et al., 2008). TCs are projected to become more destructive (Grinsted et al., 2019) and intense TCs may become more frequent (e.g., Bender et al. (2010)) in a warmer climate.

Vertical wind shear, i.e. the vertical shear of horizontal wind, has long been linked to TC intensity. Increased vertical wind shear has been found to impede intensification by tilting the TC vortex and causing an outward flux of potential vorticity (PV) and equivalent potential temperature, thereby weakening the cyclone (Frank and Ritchie, 2001). Further, vertical wind shear aids in ventilating the TC core by entraining relatively dry environmental air into convective updrafts (Emanuel et al., 2004; Tang and Emanuel, 2010, 2012) and into the boundary layer (Riemer et al., 2010; Riemer and Laliberté, 2015). Entrainment thereby reduces latent heating and buoyancy, and thus hinders convection. Furthermore, entrainment reduces the equivalent potential temperature in the convective updrafts, which leads to outflow at lower altitudes and thereby warmer temperatures. This reduces the intensity of the TC following the heat engine model of Emanuel (1986). Relative humidity at various pressure levels throughout the lower and mid-troposphere has been linked to TC intensity and intensification rates, and reduced relative humidity has been found to reduce TC activity (e.g., Kaplan and DeMaria (2003); Emanuel et al. (2004); Hendricks et al. (2010); Wu et al. (2012)). The ventilation index of Tang and Emanuel (2012) includes the combined effect of humidity and vertical wind shear. It has been found useful in the reconstruction of the annual cycle of North Atlantic TC activity, in particular the typically sharp increase in activity from July to August (Yang et al., 2021). Further, the ventilation index shows significant correlation with TC frequency and rapid intensification (i.e. an increase in maximum wind speed of at least 15.4 m/s in 24 hours, see Kaplan and DeMaria (2003)) frequency within numerical modeling frameworks (Horn et al., 2014).

The large potential for damage that TCs can cause gives rise to the need for seasonal forecasting of TCs, which is an endeavor that has been undertaken for several decades. In the North Atlantic, the earliest attempts by Gray (1984a,b) used El Niño events, Quasi-Biennial Oscillation phases and sea-level pressure anomalies in the Caribbean during spring and early summer to forecast hurricane activity with useful skill. Since then, this approach of statistical forecasting has been continuously developed (e.g., Klotzbach and Gray (2004); Saunders and Lea (2005); Klotzbach (2007)). Statistical forecasting generally makes use of the relationship between observable phenomena and environmental factors relevant to TC activity. For example, positive El Niño phases correlate with an increase in vertical wind shear and a decrease in TC activity in the tropical North Atlantic (Aiyyer and Thorncroft, 2006).

Dynamical seasonal forecasts, where a numerical model is used to predict the future state of the atmosphere, can also be used to predict TC activity. In a purely dynamical approach, TCs within the forecast are tracked and evaluated directly. Even at low resolutions, climate models can produce TC-like structures, though the simulated TCs are larger and weaker than observed TCs (Manabe et al., 1970; Bengtsson et al., 1982). Still, while individual TCs are unrealistic, they provide useful information for forecasting the geographical and seasonal distribution of TCs (Bengtsson et al., 1995). Dynamical forecasting has since improved greatly, and provides skillful results (e.g., Thorncroft and Pytharoulis (2001); Vitart et al. (2007); Vecchi et al. (2014); Zhang et al. (2019)). Dynamical forecasts can also be used in combination with statistical modeling in a hybrid approach, where the large-scale environment produced by the dynamical forecast is used to make statistical forecasts. Operational TC forecasts have generally been found to have good skill in predicting the number of TCs, and some provide useful information on landfall locations and regional activity (Klotzbach et al., 2019).

Forecasts for the 2013 North Atlantic hurricane season were consistently indicating an above average activity in terms of number of named storms, hurricanes and major hurricanes. In reality, there were 14 named storms, which is slightly above average, but only two category 1 hurricanes and no major hurricanes, which is far below average. Zhang et al. (2016) proposed that an increased number of anticyclonic Rossby wave breaking events reduced the humidity in the tropics through mixing with extratropical air and increased vertical wind shear. This prevented cyclones from intensifying despite other environmental factors being conducive to intense cyclones. Zhang et al. (2016) investigated the development of Rossby waves using PV, and drew special attention to the peculiar extreme equatorward position of the 2 potential vorticity unit (PVU) contour on the 350 K isentropic surface during August. The 2 PVU contour can also be used to identify stratospheric PV streamers, which are elongated filaments that protrude from the high-PV stratosphere into the low-PV troposphere. These, in turn, can be used as a proxy for anticyclonic Rossby wave breaking (Wernli and Sprenger, 2007; Béguin et al., 2013; Sprenger et al., 2017).

PV streamers and associated Rossby wave breaking events can be reliably identified (e.g., Bowley et al. (2019); Papin et al. (2020)), and Rossby wave breaking has been studied in reanalysis data (e.g., Postel and Hitchman (1999); Scott and Cammas (2002); Abatzoglou and Magnusdottir (2006); Wernli and Sprenger (2007)). However, predicting Rossby wave breaking based on numerical models may show biases in frequency and location (Barnes and Hartmann, 2012). The location biases are not simply a direct result of biases in the general tropopause location, but of where along the tropopause models produce these events. The bias in Rossby wave breaking frequency is largest in the North Atlantic region, and the bias of the 2 PVU contour (i.e., the tropopause) latitude has been found to be lower than that of the Rossby wave breaking latitude during summer in climate models (Béguin et al., 2013).

The link between TC activity, which is often described in terms of accumulated cyclone energy (ACE) (Bell et al., 2000), and PV streamers as a proxy for Rossby wave breaking has been investigated in several publications. Li et al. (2018) found that Rossby wave breaking events are generally uncorrelated with ACE on a short time scale of 8 days, using their entire data data set from 1985–2013, but also found that they correlate during a number of individual years, which may point towards interannual variability of correlation. On a seasonal time scale, ACE correlates substantially and negatively with Rossby wave breaking frequency and the area of the involved PV streamers (Zhang et al., 2017), and a combined measure which takes into account frequency, size and the magnitude of the anomaly of PV streamers (Papin et al., 2020) on the 350 K isentropic surface. Rossby wave breaking can also enable tropical cyclogenesis (Takemura and Mukougawa, 2021) via tropical transition, where a precursor extratropical cyclone develops tropical characteristics, such as a warm core and axisymmetry (Davis and Bosart, 2004). McTaggart-Cowan et al. (2013) found that tropical cyclogenesis via tropical transition accounts for over a third of tropical cyclogenesis events in the North Atlantic basin. Despite the potential for cyclogenesis, it appears that the overall effect of an increased Rossby wave breaking frequency is detrimental to TC activity in terms of ACE (Zhang et al., 2017). TCs formed via tropical transition have been found to be less predictable than TCs formed via other genesis pathways (Wang et al., 2018), which suggests that changes in Rossby wave breaking frequency may affect predictability throughout a TC season.

The aim of this study is to assess if the latitude of the 2 PVU contour on multiple isentropic surfaces can potentially act as a predictor for seasonal ACE. The effects on environmental vertical wind shear and mid-tropospheric relative humidity are assessed and compared to the effects caused by Rossby wave breaking. Furthermore, it is investigated if changes in the position of the 2 PVU contour have an impact on other TC-related metrics concerning number and lifetime.

The following sections are organized as follows. Section 2 describes the methods and data

used in this study. Section 3 describes the statistical link between the 2 PVU contour latitude and ACE. Section 4 describes the impact that the 2 PVU contour latitude exerts on environmental variables, and Section 5 describes the exerted impact on TC count and lifetime metrics. Section 6 summarizes the results and states the key conclusions.

4.2 Data and Methods

For the purpose of this study, the North Atlantic hurricane season is defined as beginning on June 1 at 00:00 UTC, and ending on December 1 at 00:00 UTC. Only the North Atlantic basin is considered.

Observational and reanalysis data for the years 1980 to 2017 are used. The observational HURDAT2 TC data (Landsea and Franklin, 2013) provide the longitude and latitude of cyclone centers, as well as wind speeds that are needed to calculate ACE. ACE is defined as

$$ACE = \sum_{i=1}^{k} v_{max,i}^2 \tag{4.1}$$

where $i = 1$ is the initial time (e.g., the beginning of the season), k is the final time (e.g., the end of the season), and v_{max} is the maximum wind speed of any given TC at a given time. Data are used in 6-hourly intervals. ACE includes only TCs, which for the purposes of this study are defined as any cyclone categorized as tropical storm (TS) or hurricane (HU) in the HURDAT2 data, and are only considered at synoptic hours (i.e. 00:00, 06:00, 12:00 and 18:00 UTC).

HURDAT2 data are further used to derive other metrics for seasonal activity. The first is the number of individual days per season where a cyclone of hurricane strength (categorized in HURDAT2 as HU) exists within the North Atlantic basin (hurricane days). The second is the number of individual days per season where a cyclone of at least tropical storm strength (categorized in HURDAT2 as TS or HU) exists within the North Atlantic basin (storm days), which thus includes hurricane days. The third is the number of named storms. The fourth is the number of named storms that make landfall, where named storms that make landfall multiple times are counted only once. The fifth is the lifetime of TCs, where the number of entries at synoptic hours and at which the TC is categorized as TD (tropical depression), TS or HU is used. All named terms that contain the word "storm" refer exclusively to TC systems, and not any other storm system, within this study.

Genesis location density is defined by first dividing the North Atlantic basin into squares of 5° side length. HURDAT2 data are then used to obtain the first entry for each cyclone in a set of years, as motivated in the corresponding section. The resulting number of cyclones per square is divided by the number of included cyclones, as this allows for a more meaningful comparison of two distinct sets of years with a different number of total cyclones.

ERA5 reanalysis data (Hersbach et al., 2020) are used to obtain PV, wind and relative humidity data. PV is interpolated to a 0.5°x0.5° grid and to isentropic surfaces from 345 K to 365 K in 5 K intervals. The algorithm used in Sprenger et al. (2017) is used to identify the 2 PVU contour on isentropic surfaces in terms of equidistant points along the contour. The latitude of the 2 PVU contour, here dubbed $\overline{\Phi}_{TP}$, is then calculated as the mean latitude of these points within a zonal window of 5° half-width at individual longitudes. $\overline{\Phi}_{TP}$ thus describes the smoothed 2 PVU contour latitude at every longitude on the considered isentropic surfaces.

The PV streamer detection algorithm of Sprenger et al. (2017), which is a refined version of the Wernli and Sprenger (2007) algorithm, is used to obtain PV streamer frequencies with a

resolution of 0.5°x0.5°. Other methods of obtaining PV streamer frequency, in particular the one used in Papin et al. (2020), identify the centroid of the streamer, and obtain from it the geographical distribution of the frequency. In comparison, the method of Sprenger et al. (2017) identifies all points on the specified grid where a PV streamer is present, and not only the centroid position. The frequency is defined as the ratio of time steps at which a PV streamer is present at a given location and the total number of time steps in the considered time interval. PV streamers are used as a proxy for anticyclonic Rossby wave breaking.

Various pressure levels have been used to describe mid-tropospheric humidity. Within this study, it is quantified by total precipitable water between 850 and 200 hPa in order to not be limited to a single or only few pressure levels. 850 and 200 hPa are chosen be consistent with the levels used in Zhang et al. (2016).

Consistent with the pressure levels used for total precipitable water, vertical wind shear is defined as the difference between horizontal wind on the 200 hPa and the 850 hPa isobaric surface, i.e.:

$$VWS = \sqrt{(u_{200} - u_{850})^2 + (v_{200} - v_{850})^2} \tag{4.2}$$

where VWS is vertical wind shear, u and v are the zonal and meridional wind components, respectively, and the indices denote the isobaric surface in hPa.

As vertical wind shear and humidity act in combination to ventilate TCs, the ventilation index of Tang and Emanuel (2012) is calculated to quantify this combined effect. The ventilation index is defined as:

$$VI = \frac{VWS \cdot \chi_m}{u_{PI}} \tag{4.3}$$

where u_{PI} is the potential intensity as defined by Bister and Emanuel (2002), and χ_m is the entropy deficit, defined as:

$$\chi_m = \frac{s_m^* - s_m}{s_{SST}^* - s_b} \tag{4.4}$$

where s_m^* is the saturation entropy at 600 hPa, s_m is the entropy at 600 hPa, s_{SST}^* is the saturation entropy at the sea surface, and s_b is the entropy in the boundary layer. Entropy is calculated as in Tang and Emanuel (2012), who apply the pseudo-adiabatic entropy according to Bryan (2008). The boundary layer entropy is calculated using values at 950 hPa, which is assumed to be representative for the boundary layer.

The main development region (MDR) is defined as the region from 10°N to 20°N and from 20°W to 80°W (Goldenberg and Shapiro, 1996). The MDR is split into an eastern MDR (EMDR) and a western MDR (WMDR), with the border being at 50°W. Further, a high intensity region (HIR) is defined to represent the region where major hurricanes occur, based on Knapp et al. (2010). The corners of this region are at (50°W, 30°N), (100°W, 30°N), (100°W, 21°N), (83°W, 10°N), (50°W, 10°N), such that it encompasses the Gulf of Mexico and the western tropical North Atlantic basin. Both regions are shown in fig. 4.1.

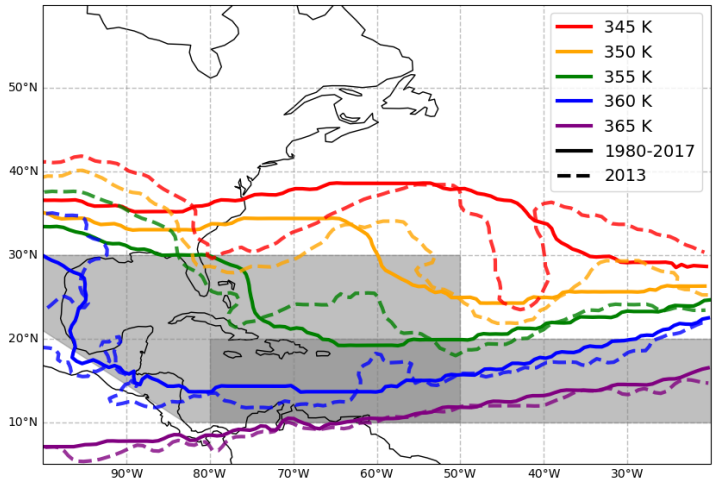

Figure 4.1: Mean 2 PVU contour in September on the 345 K to 365 K isentropic surfaces using 1980–2017 climatology (solid) and 2013 (dashed) ERA5 data between 100°W and 20°W. Gray regions denote the HIR and MDR, with the darker shading indicating the overlap of the two regions.

4.3 $\overline{\Phi}_{TP}$ as a Predictor for ACE

This section explores $\overline{\Phi}_{TP}$ as a simplified predictor for seasonal ACE in place of other PV-related metrics, such as area and frequency of Rossby wave breaking events (e.g., Zhang et al. (2016)), or PV streamer index (Papin et al., 2020). Fig. 4.1 shows the September mean 2 PVU contours for the ERA5 (1981–2017) period and for the year 2013. Previous studies focused heavily on the 350 K isentropic surface, and found that Rossby wave breaking has an effect on ACE on a sub-seasonal and seasonal time scale (Zhang et al., 2016, 2017; Papin et al., 2020), but not on a time scale of 8 days (Li et al., 2018). Here, it is explored whether $\overline{\Phi}_{TP}$ calculated for monthly mean PV fields on the 350 K isentropic surface also correlates well with ACE, and whether this correlation is stronger on other isentropic surfaces.

Fig. 4.2 shows the correlation coefficient of monthly mean $\overline{\Phi}_{TP}$ at longitudes from 90°W to 30°W and from June to September with seasonal basin-wide ACE. Only the 350 K and 360 K isentropic surfaces are shown, as the correlations below 350 K and above 360 K are weaker.

On the 350 K isentropic surface during September there is substantial correlation of $\overline{\Phi}_{TP}$ with ACE (r=0.67) with a maximum at 71°W. This is roughly where the climatological TC track density (1979–2007) is at a maximum, and where the most intense cyclones are located (Knapp et al., 2010). Therefore, environmental changes in this region affect many cyclones, and changes in TC intensity can have a higher impact on ACE due to the squared dependence of ACE on wind speed. Further, 71°W is about 5° to the west of where Zhang et al. (2016) identified the highest Rossby wave breaking frequency in August, and substantially further to the west of where Papin et al. (2020) identified the climatological maximum of PV streamer frequency during September. However, both use the PV streamer centroid to designate the position of the PV streamer and Rossby wave breaking. The centroid position is expected to be further east than the minimum latitude associated with a PV streamer. As shown in fig. 4.3, which is discussed in section 4c, the maximum correlation is also further to the west of the maximum PV streamer frequency when using the method of Sprenger et al. (2017), which is not as far east as that found in Papin

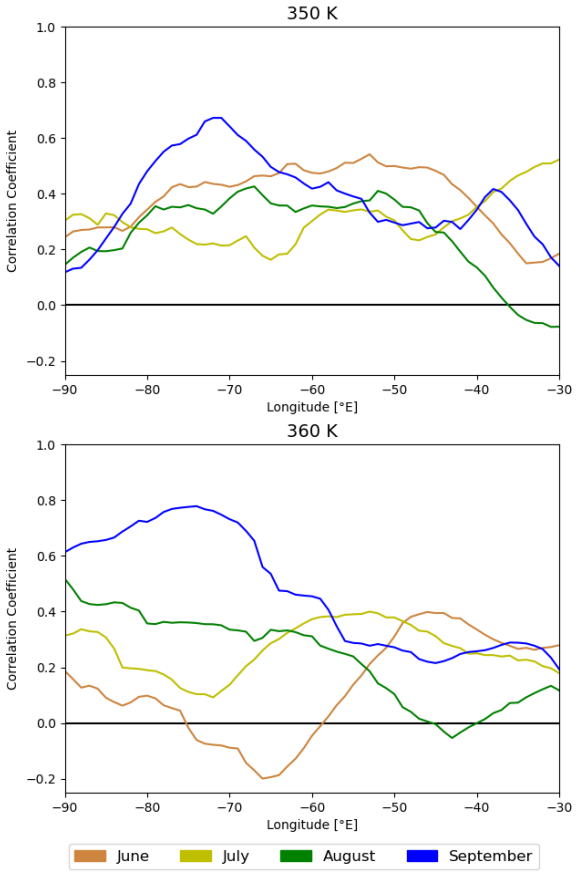

Figure 4.2: Linear correlation coefficients of $\overline{\Phi}_{TP}$ on the 350 K and 360 K isentropic surfaces with seasonal ACE using ERA5 and HURDAT2 data from 1980 to 2017 from June to September using a 5° half-width.

et al. (2020). In the low-activity 2013 season, the mean 2 PVU contour shows an equatorward deflection at around 75°W in September. At this location, the PV streamer frequency has been found to be increased in 2013 (Papin et al., 2020). It thus appears that ACE is influenced by $\overline{\Phi}_{TP}$, and by the frequency of PV streamers, specifically in a region where PV streamers are not maximally frequent in a climatological sense, and where many potentially intense cyclones occur.

On the 360 K isentropic surface, the correlation coefficient of September $\overline{\Phi}_{TP}$ with ACE is largest (r=0.78) at 74°W. While the correlation coefficient is very close to that on the 350 K isentropic surface, it is stronger than on the 350 K isentropic surface and remains stronger over a broader region. The reason for this difference is explored in the next section.

On the 350 K isentropic surface, June $\overline{\Phi}_{TP}$ is substantially correlated with ACE, which is stronger than the correlations of July and August $\overline{\Phi}_{TP}$ with ACE. This is likely not due to a direct effect of $\overline{\Phi}_{TP}$ on ACE during June, as only about 1% of ACE is produced in June in a 1980–2017 mean using HURDAT2 data, while about 5% and 24% are produced in July and August, respectively. Further, June $\overline{\Phi}_{TP}$ correlation with June monthly ACE is weaker than with seasonal ACE (not shown). A more plausible explanation is thus that $\overline{\Phi}_{TP}$ is autocorrelated. PV streamers typically do not persist for multiple months, and individual Rossby wave breaking events typically do not correlate with ACE on short time scales (Li et al., 2018). It is therefore assumed that autocorrelation of $\overline{\Phi}_{TP}$ is due to other underlying features, such as the correlation of Rossby wave breaking events with teleconnection indices described by Bowley et al. (2019).

$\overline{\Phi}_{TP}$ autocorrelations are summarized in table 4.1. As the question at hand is whether strong

Table 4.1: Autocorrelation coefficients of $\overline{\Phi}_{TP}$ on the 350 K and 360 K isentropic surfaces between months at their respective longitude where $\overline{\Phi}_{TP}$ correlates maximally with seasonal ACE, and said longitude. The listed longitude is the central longitude of the 5° half-width zonal window within which $\overline{\Phi}_{TP}$ is calculated.

350 K	Lon	Jul	Aug	Sep
Jun	53°W	0.35	0.39	0.43
Jul	30°W		0.39	0.43
Aug	67°W			0.40
Sep	71°W			
360 K	Lon	Jul	Aug	Sep
Jun	46°W	0.10	0.19	0.40
Jul	53°W		0.34	0.35
Aug	90°W			0.67
Sep	74°W			

correlation of June $\overline{\Phi}_{TP}$ with seasonal ACE is due in part to autocorrelation and strong correlation of September $\overline{\Phi}_{TP}$ with seasonal ACE, the longitude where the correlation coefficient is maximal is chosen for every month and isentropic surface, as denoted in table 4.1.

On the 350 K isentropic surface, June $\overline{\Phi}_{TP}$ correlates with September $\overline{\Phi}_{TP}$ with a correlation coefficient of r=0.43. This is similar to the autocorrelation of the PV streamer index in June-July with that in August-November found by Papin et al. (2020). July and August $\overline{\Phi}_{TP}$ correlate similarly with September $\overline{\Phi}_{TP}$.

On the 360 K isentropic surface, the autocorrelation coefficient of June $\overline{\Phi}_{TP}$ with September $\overline{\Phi}_{TP}$ is 0.4, but it should be noted that June $\overline{\Phi}_{TP}$ at 74°W is essentially uncorrelated with September $\overline{\Phi}_{TP}$ at 74°W (r<0.2). Autocorrelation coefficients of July and August with September are 0.35 and 0.67, respectively. The increased autocorrelation of August with September is reflected in the increased correlation of August $\overline{\Phi}_{TP}$ with seasonal ACE at the western edge of the investigated longitudinal range, while the opposite is observed for July, where a reduction in autocorrelation accompanies a reduction in correlation with seasonal ACE. The substantial correlation of June and July $\overline{\Phi}_{TP}$ with seasonal ACE are thus concluded to be due to autocorrelation of $\overline{\Phi}_{TP}$. The correlation of August $\overline{\Phi}_{TP}$ with seasonal ACE may be due to two factors. First, August contributes substantially more to seasonal ACE than June and July, which allows for a direct influence on ACE that is on a relevant scale compared to the full season. Second, the autocorrelation of $\overline{\Phi}_{TP}$ from August to September implies that effects of $\overline{\Phi}_{TP}$ on ACE during September are inherently linked to August $\overline{\Phi}_{TP}$.

In summary, September $\overline{\Phi}_{TP}$ on the 360 K isentropic surface could be a potent predictor for seasonal TC activity due to the broad region of strong correlation. Notably, the correlation is slightly stronger than those found by Zhang et al. (2017) and Papin et al. (2020) between several Rossby wave breaking metrics on the 350 K isentropic surface, such as frequency and area, and ACE in the North Atlantic basin. Both Zhang et al. (2017) and Papin et al. (2020)

also relied on reanalysis data to come to these findings, but based on 1979–2013 and 1979–2015 data, respectively. Since the correlation is particularly strong in September, $\overline{\Phi}_{TP}$ as a predictor would be mostly relevant for mid-season forecasting, where the lead time is the shortest. June $\overline{\Phi}_{TP}$ on the 350 K isentropic surface may be of some use for pre-season forecasting of ACE, due to autocorrelation of $\overline{\Phi}_{TP}$. However, the correlation with ACE is substantially weaker than that found on the 360 K isentropic surface for September $\overline{\Phi}_{TP}$.

4.4 The Link Between $\overline{\Phi}_{TP}$ and Environmental Variables

The mechanisms by which $\overline{\Phi}_{TP}$ influences ACE are not necessarily the same across isentropic surfaces, and the location where the influence is exerted may also differ. This section shows that vertical wind shear and relative humidity are affected by $\overline{\Phi}_{TP}$, that $\overline{\Phi}_{TP}$ on the 350 K isentropic surface influences ACE via similar pathways as $\overline{\Phi}_{TP}$ on the 360 K isentropic surface does, and that the affected regions differ, but partially overlap.

Zhang et al. (2016) argue that Rossby wave breaking leads to a reduction in humidity and an increase in vertical wind shear in the tropical North Atlantic. Multiple linear regression analysis based on 1980–2017 ERA5 data is thus used to assess whether there is a link between September $\overline{\Phi}_{TP}$, 850–200 hPa precipitable water, and 200 hPa - 850 hPa vertical wind shear. The goal is not to use this analysis to make any direct predictions, but only to argue that a dependence between these quantities exists. September $\overline{\Phi}_{TP}$ at 71°W is used on the 350 K isentropic surface, and September $\overline{\Phi}_{TP}$ at 74°W is used on the 360 K isentropic surface, as this is where the correlations with seasonal ACE are largest (see table 4.1). Adjusted R^2 values, which quantify the variance in the predicted variable that is explained by the variance in the predictors, are referred to as R^2 values for simplicity. The p-value is listed for the R^2 value and the regression coefficients, which represents the probability that the null hypothesis, i.e. there being no link between the predictors and the explained variable, is true based on the statistical test. For example, a p-value of 0.05 would thus signify a 95% confidence that a detected link truly exists, as the probability that the null hypothesis is true is only 5%. HIR, MDR, EMDR and WMDR mean values of vertical wind shear and precipitable water are considered separately for the linear regression analysis.

4.4.1 The HIR and the MDR

Table 4.2 summarizes the regression results for the HIR and MDR. Using only vertical wind shear as a predictor and using the 350 K isentropic surface, both regions show substantial correlation (R^2 >0.4, rows 1 and 2) of $\overline{\Phi}_{TP}$ with the mean vertical wind shear in the respective region. Using precipitable water as an additional predictor slightly increases the R^2 value in the HIR, but has only a very weak effect in the MDR. The p value associated with precipitable water is somewhat low for the HIR (p<0.1, row 3) and very large for the MDR (p>0.3, row 4). Changes in $\overline{\Phi}_{TP}$ thus seem to be linked to changes in precipitable water in the HIR, though not as strongly as to vertical wind shear. In contrast, it cannot be said with confidence that $\overline{\Phi}_{TP}$ is linked to changes in precipitable water in the MDR.

The lack of correlation with precipitable water in the MDR differs strongly from the findings of Zhang et al. (2016), who state that humidity changes are linked to Rossby wave breaking events on the 350 K isentropic surface. However, this apparent contradiction can be reconciled. Zhang et al. (2016) use the month of August, and not September, in their analysis. Repeating the multiple linear regression analysis for August reveals that using precipitable water as a sole predictor yields a similar R^2 value as when using vertical wind shear as a sole predictor (R^2=0.23 and R^2=0.27, respectively). Further, using precipitable water as the sole predictor for September results in a lower R^2 value (R^2=0.15), indicating that the link between $\overline{\Phi}_{TP}$ and precipitable water is substantially stronger in August than in September. Precipitable water as the sole predictor is significantly linked to $\overline{\Phi}_{TP}$ at the 95% level in all of these cases, but still very weak

Table 4.2: Multiple linear regression results for September mean $\overline{\Phi}_{TP}$ predicted by September mean vertical wind shear (VWS) and precipitable water (PW), listing the model, regression coefficients (β_n), the p-value of the coefficients (p_{β_n}), the adjusted R^2 value, and the p-value of the corresponding F-test. Indices for $\overline{\Phi}_{TP}$ denote the isentropic surface in K, and alphabetical indices for precipitable water and vertical wind shear denote the region within which they are averaged. ERA5 data for 1980 to 2017 are used.

Model	β_1 [ms^{-1}]	p_{β_1}	β_2 [mm]	p_{β_2}	adj. R^2	p(F)
$\overline{\Phi}_{TP,350} = \beta_1 \cdot VWS_{HIR}$	-1.7	$< 10^{-3}$			0.416	$< 10^{-3}$
$\overline{\Phi}_{TP,350} = \beta_1 \cdot VWS_{MDR}$	-1.1	$< 10^{-3}$			0.489	$< 10^{-3}$
$\overline{\Phi}_{TP,350} = \beta_1 \cdot VWS_{HIR} + \beta_2 \cdot PW_{HIR}$	-1.5	$< 10^{-3}$	0.8	0.081	0.450	$< 10^{-3}$
$\overline{\Phi}_{TP,350} = \beta_1 \cdot VWS_{MDR} + \beta_2 \cdot PW_{MDR}$	-1.0	$< 10^{-3}$	0.4	0.337	0.488	$< 10^{-3}$
$\overline{\Phi}_{TP,360} = \beta_1 \cdot VWS_{HIR}$	-1.9	0.003			0.201	0.003
$\overline{\Phi}_{TP,360} = \beta_1 \cdot VWS_{MDR}$	-1.5	$< 10^{-3}$			0.335	$< 10^{-3}$
$\overline{\Phi}_{TP,360} = \beta_1 \cdot VWS_{HIR} + \beta_2 \cdot PW_{HIR}$	-1.6	0.009	2.2	0.014	0.309	$< 10^{-3}$
$\overline{\Phi}_{TP,360} = \beta_1 \cdot VWS_{MDR} + \beta_2 \cdot PW_{MDR}$	-1.2	0.003	1.6	0.049	0.389	$< 10^{-3}$

compared to vertical wind shear as the sole predictor in the MDR, as is evident from the R^2 values.

A plausible reason for the decline of precipitable water as a predictor for $\overline{\Phi}_{TP}$ is that Rossby wave breaking is most active during summer. It peaks in July in the North Atlantic basin (Postel and Hitchman, 1999; Abatzoglou and Magnusdottir, 2006; Papin et al., 2020), and is responsible for mixing dry air into the tropics (e.g., Zhang et al. 2016). A reduction in these events could lead to less mixing, and thus a reduced impact on precipitable water in the tropical North Atlantic in September as compared to August. Further, there is also a reduction in vertical extent of Rossby wave breaking events from August to September (Abatzoglou and Magnusdottir, 2006). As the presence of a PV streamer is not required for a horizontal PV gradient to exert an influence on the wind field, and horizontal PV gradients are weaker in summer than in autumn (Postel and Hitchman, 1999), vertical wind shear can thus become the dominant predictor instead of precipitable water. Notably, even though the North Atlantic extratropics are generally drier in boreal autumn than in boreal summer (Gettelman et al., 2006), the humidity change from August to September does not appear large enough to compensate for the reduction in mixing due to reduced PV streamer activity.

Using the 360 K isentropic surface (rows 5 through 8), vertical wind shear remains the dominant predictor. However, using precipitable water as an additional predictor in the MDR increases the R^2 value from 0.335 to 0.389, and the p value associated with precipitable as a predictor is quite low with p=0.014. Precipitable water thus appears to be responsive to changes in $\overline{\Phi}_{TP}$ on the 360 K isentropic surface in the MDR. Section 4b argues that this response is not present in the entire MDR, and section 4c elucidates the cause for this response.

4.4.2 The WMDR and EMDR

Table 4.3 shows the multiple linear regression results of the WMDR and EMDR subregions. Using the 350 K isentropic surface and vertical wind shear as the sole predictor (rows 1 and 2), the correlation of $\overline{\Phi}_{TP}$ with vertical wind shear is substantially stronger in the WMDR than in the EMDR. As argued in the previous section, the WMDR is where the correlation coefficient of

Table 4.3: As table 4.2, but using the EMDR and WMDR.

.

Model	β_1 [ms^{-1}]	p$_{\beta_1}$	β_2 [mm]	p$_{\beta_2}$	adj. R^2	p(F)
$\overline{\Phi}_{TP,350} = \beta_1 \cdot VWS_{EMDR}$	-1.1	$< 10^{-3}$			0.297	$< 10^{-3}$
$\overline{\Phi}_{TP,350} = \beta_1 \cdot VWS_{WMDR}$	-0.8	$< 10^{-3}$			0.464	$< 10^{-3}$
$\overline{\Phi}_{TP,350} = \beta_1 \cdot VWS_{WMDR} + \beta_2 \cdot PW_{WMDR}$	-0.7	$< 10^{-3}$	0.3	0.476	0.457	$< 10^{-3}$
$\overline{\Phi}_{TP,360} = \beta_1 \cdot VWS_{EMDR}$	-1.4	0.004			0.182	0.004
$\overline{\Phi}_{TP,360} = \beta_1 \cdot VWS_{WMDR}$	-1.1	$< 10^{-3}$			0.331	$< 10^{-3}$
$\overline{\Phi}_{TP,360} = \beta_1 \cdot VWS_{WMDR} + \beta_2 \cdot PW_{WMDR}$	-0.8	0.003	2.2	0.002	0.475	$< 10^{-3}$

September $\overline{\Phi}_{TP}$ with ACE is maximal, and to the west of where the maximum in PV streamer frequency is located (see fig. 4.3, which is discussed in more detail further below). The vertical wind shear response in the WMDR thus seems to be sensitive to westward displacements of PV streamer frequency as was the case in 2013 (Papin et al., 2020), while vertical wind shear in the EMDR appears to be affected less. The reduced effect on the EMDR compared to the WMDR is a result of $\overline{\Phi}_{TP}$ on the 350 K isentropic surface being used at 71°W, i.e. where the correlation with ACE is strongest, which is within the WMDR.

Using precipitable water as an additional predictor in the WMDR reduces the R^2 value very slightly, and has an associated p value in excess of 0.4. Precipitable water changes due to changes in $\overline{\Phi}_{TP}$ on the 350 K isentropic surface are thus concluded to be negligible.

Using the 360 K isentropic surface and vertical wind shear as the sole predictor, the R^2 values decrease substantially in both subregions. However, using precipitable water as an additional predictor in the WMDR, the resulting R^2 value of 0.48 is rather close to those predicting the 350 K isentropic surface in the WMDR (R^2=0.46) and in the entire MDR (R^2=0.49). Therefore, when using the 360 K isentropic surface, both vertical wind shear and precipitable water in the WMDR are important predictors for $\overline{\Phi}_{TP}$. The reason for this is explored in the following subsection.

4.4.3 PV Streamer Climatology on the 350 K and 360 K Isentropic Surfaces

The PV streamer frequency in the North Atlantic region on the 360 K isentropic surface is shown in fig. 4.3 compared to the frequency on the 350 K isentropic surface, as identified in ERA5 data during the 1980–2017 period. Note that the Sprenger et al. (2017) algorithm is used to identify PV streamers, which does not use the centroid position, but the entire area of the streamer feature. Therefore, the southward extent of streamers is represented more accurately than when the centroid position is used (see also section 2).

On the 350 K isentropic surface, the PV streamer frequency is reduced from August to September, and the maximum is shifted eastwards, as also found by, e.g., Papin et al. (2020) tracking PV streamer centroid positions. PV streamer activity is thus shifted away from where TC activity is high (Knapp et al., 2010). On the 360 K isentropic surface, Abatzoglou and Magnusdottir (2006) show an increase in the number of Rossby wave breaking events from August to September in the North Atlantic region. However, this may be a result of their counting method.

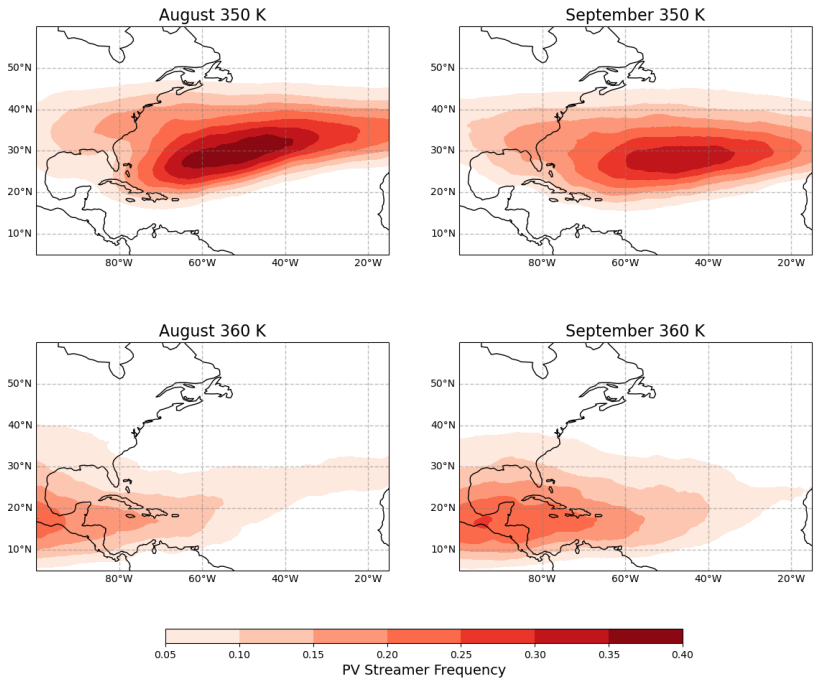

Figure 4.3: ERA5 1980–2017 climatological PV streamer frequency on the 350 K (top) and 360 K (bottom) isentropic surface during August (left) and September (right).

They counted events on the 360 K isentropic surface only if the event was not also present on the 350 K isentropic surface, such that an increase in the number of events on the 360 K isentropic surface may also be due to a reduction in vertical extent of events and not a true increase in the number of events. Fig. 4.3 shows that there is a genuine increase in PV streamer frequency from August to September on the 360 K isentropic surface, as the region where PV streamers occur shifts eastward from the Pacific into the North Atlantic region. Notably, PV streamer frequency is maximal between 10°N and 20°N, and is thus shifted into the WMDR. This strongly implies increased Rossby wave breaking in the WMDR during September, which enables mixing, and thus the comparatively strong response of precipitable water to changes in $\overline{\Phi}_{TP}$ as described in the previous subsection. The increase in PV streamer frequency from August to September is also consistent with the increase in correlation coefficient of $\overline{\Phi}_{TP}$ with ACE from August to September (see fig. 4.2).

4.4.4 $\overline{\Phi}_{TP}$ Quartiles on the 360 K Isentropic Surface

As 38 years are used within this study (1980–2017), the 9 years with the northernmost September $\overline{\Phi}_{TP}$ and the 9 years with the southernmost September $\overline{\Phi}_{TP}$ positions on the 360 K isentropic surface roughly correspond to, and are from here on referred to, as $\overline{\Phi}_{TP}$ quartiles. They are contrasted to highlight the difference between low (southern) and high (northern) values of $\overline{\Phi}_{TP}$. Only the 360 K isentropic surface is used to derive these quartiles, as this is where correlation with seasonal ACE is strongest in September (see fig. 4.2), and the specification of the isentropic surface is omitted for brevity.

Fig. 4.4 shows the PV streamer frequency for the southernmost and northernmost $\overline{\Phi}_{TP}$ quartiles. The southernmost quartile shows a substantially higher PV streamer frequency than the northernmost quartile, though the maximum is located close to the Pacific region. The northernmost quartile shows two comparatively weak maxima within the WMDR. More southern positions of $\overline{\Phi}_{TP}$ thus appear to be associated with enhanced mixing of extratropical and tropical air, though at some distance from the MDR. Fig. 4.5 shows 1980–2017 climatological

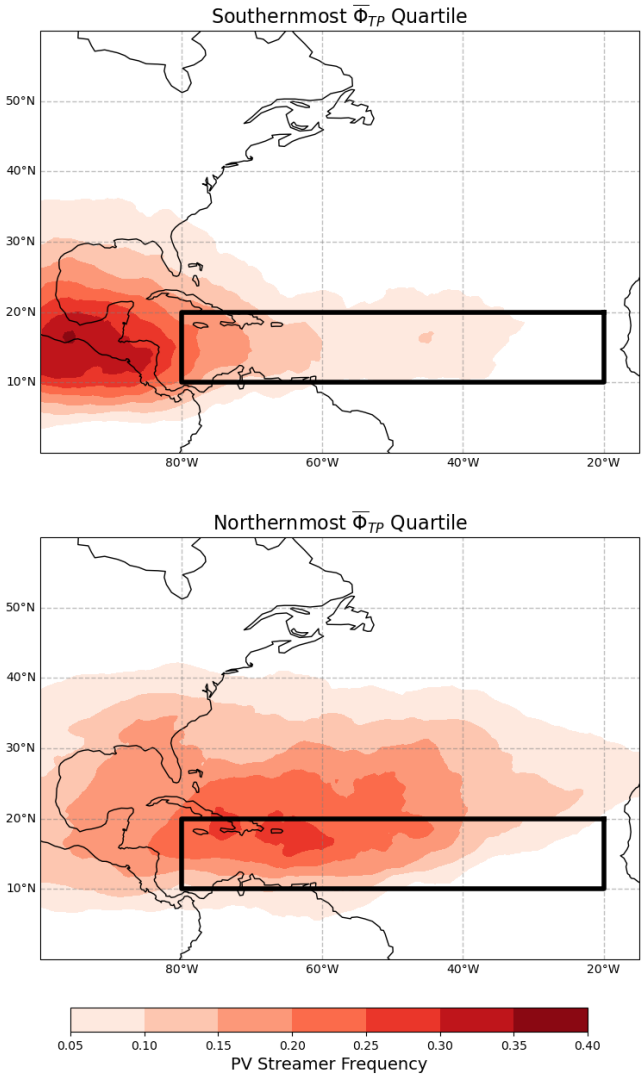

Figure 4.4: Mean September PV streamer frequency of ERA5 1980–2017 southernmost (top) and northernmost (bottom) $\overline{\Phi}_{TP}$ quartiles. The MDR is outlined in black.

September relative humidity at 600 hPa and the difference between the northernmost and southernmost $\overline{\Phi}_{TP}$ quartile. The 600 hPa level is chosen as this is the level used for the ventilation index, which depends on the difference between saturated entropy and environmental entropy. For the northernmost $\overline{\Phi}_{TP}$ quartile, where PV streamer frequency is reduced but has maxima within the MDR, relative humidity is still increased near the boundary between the WMDR and the EMDR. This indicates that the reduction in PV streamer frequency in the northernmost $\overline{\Phi}_{TP}$ quartile favors higher relative humidity, and thus TC intensification, in the WMDR more than the westward displacement of a comparatively strong maximum in the southernmost $\overline{\Phi}_{TP}$ quartile. On a different note, 600 hPa relative humidity changes substantially and significantly between the equator and 10°N between the quartiles. This implies that $\overline{\Phi}_{TP}$ could be linked to changes in the intertropical convergence zone (ITCZ), both in position and strength. However, this is not further explored here.

Fig. 4.6 shows a September mean 80°W to 50°W (i.e., the WMDR) zonal mean of zonal wind speed, the 2 PVU contour and the 350 K and 360 K isentropic surfaces for the 1980–2017 period and the southernmost and northernmost $\overline{\Phi}_{TP}$ quartiles. Both in climatology and in the

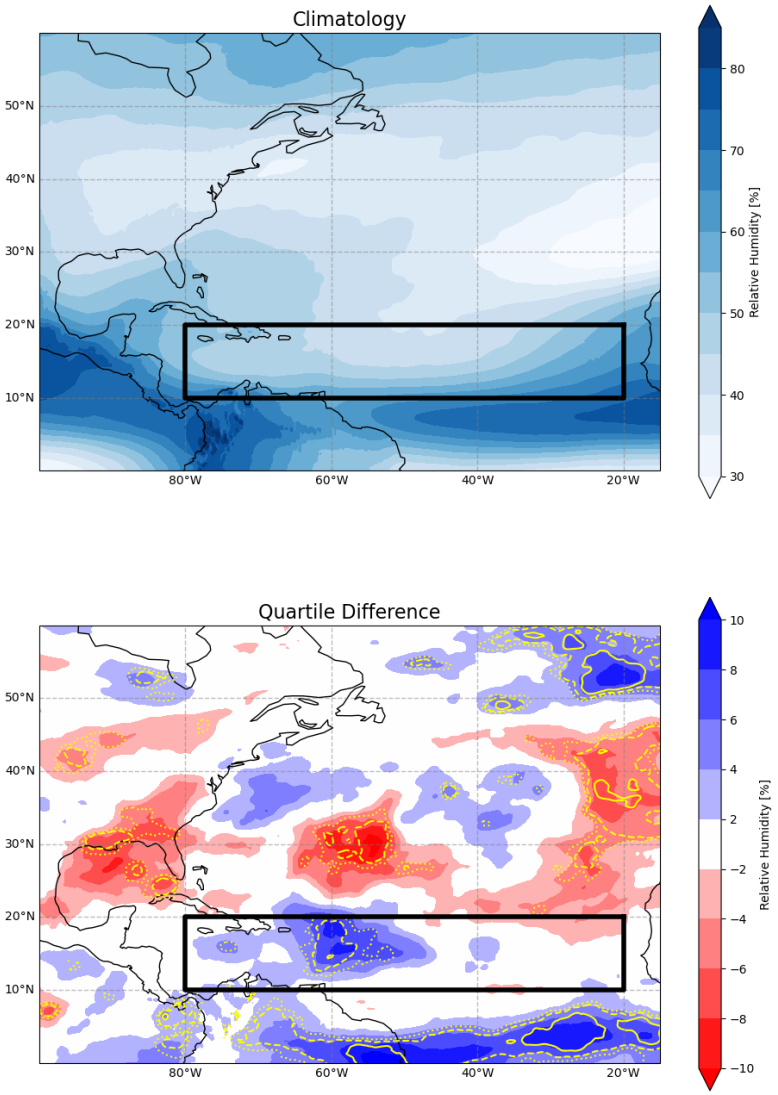

Figure 4.5: Mean September 600 hPa relative humidity of the ERA5 1980–2017 period (top) and the difference of the northernmost and southernmost $\overline{\Phi}_{TP}$ quartiles (bottom). Yellow contours denote the 90% (dotted), 95% (dashed) and 99% (solid) confidence levels. The MDR is outlined in black.

southernmost $\overline{\Phi}_{TP}$ quartile, westerly winds are dominant at upper levels in the WMDR. This places the WMDR downstream of the PV streamer frequency maximum at upper levels in the southernmost $\overline{\Phi}_{TP}$ case. Even though it is displaced to the west of the WMDR, the region of high PV streamer frequency thus still impacts the WMDR. Further, there is large-scale subsidence at upper and mid levels in the WMDR zonal mean (not shown), which allows mixing by Rossby wave breaking to the west of the WMDR to ultimately affect 600 hPa relative humidity within the WMDR. In contrast, upper level winds in the WMDR in the northernmost $\overline{\Phi}_{TP}$ quartile are predominantly easterly. The region where the quartile difference in 600 hPa relative humidity is largest within the MDR is therefore upstream of the maximum in PV streamer frequency for the northernmost $\overline{\Phi}_{TP}$ (see fig. 4.4 and fig. 4.5). The northernmost $\overline{\Phi}_{TP}$ quartile thus appears to be more humid because the effect of breaking waves does not easily propagate further into the MDR, but instead propagates towards its western boundary. As relative humidity is increased throughout most of the WMDR in the northernmost $\overline{\Phi}_{TP}$ quartile, the reduction in PV streamer frequency is concluded to be of higher importance to 600 hPa relative humidity within the WMDR than the relative displacement of high PV streamer frequency regions between quar-

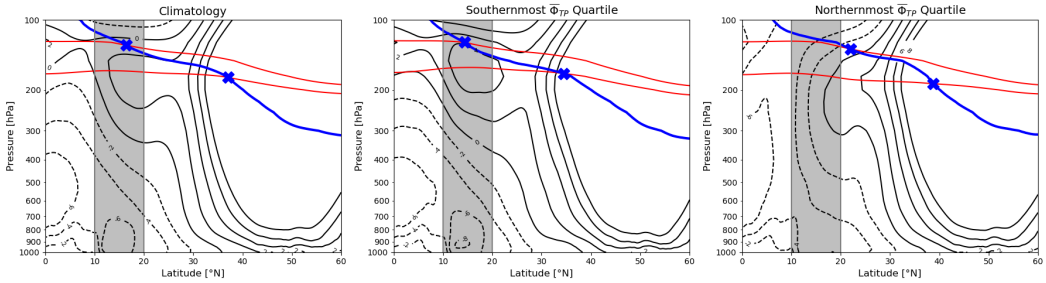

Figure 4.6: Left: ERA5 1980–2017 climatological September mean 80°W to 50°W zonal mean zonal wind speed (black contours, from -8 to 8 m/s, negative contours are dashed), 350 K and 360 K potential temperature contours (red) and 2 PVU contour (blue line). Center: Likewise, but for the 9 southernmost September mean $\overline{\Phi}_{TP,360}$. Right: Likewise, but for the 9 northernmost September mean $\overline{\Phi}_{TP,360}$. Blue crosses show 2 PVU contour intersections with potential temperature contours, and the gray area denotes the meridional extent of the MDR.

tiles.

The reversal of upper-level wind direction between quartiles also has implications for vertical wind shear. 850 hPa winds are easterly in the climatological mean as well as in the discussed quartiles. As the 200 hPa winds in the WMDR are mostly easterly in the northernmost $\overline{\Phi}_{TP}$ quartile, there is no reversal of wind direction with height, and vertical wind shear is thus greatly reduced. Near-surface winds are reduced in magnitude compared to the climatological mean, which also aids in reducing vertical wind shear. The southernmost $\overline{\Phi}_{TP}$ quartile shows an increased magnitude in zonal wind at 200 hPa in the MDR compared to the climatological mean, as well as an increase in the magnitude of near-surface winds. Vertical wind shear is thus increased due to an increase in magnitude at both levels used in the vertical wind shear definition, and the reversal of wind direction with height. The resulting difference in vertical wind shear between the two quartiles is shown in fig. 4.7, along with the 1980–2017 climatology. There is indeed a clear reduction in vertical wind shear in the northernmost $\overline{\Phi}_{TP}$ quartile as compared to the southernmost $\overline{\Phi}_{TP}$ quartile. This is in a location where there is a climatological maximum in vertical wind shear in excess of 12 m/s. A northward displacement of $\overline{\Phi}_{TP}$ thus reduces vertical wind shear throughout the WMDR, and specifically also in a region with climatologically rather pronounced vertical wind shear, which is beneficial to TC intensification. This is consistent with Aiyyer and Thorncroft (2006), who found an above average number of TCs during years where the 200 hPa flow in the MDR, which they defined as being slightly larger than used here, is easterly.

The combined effect of vertical wind shear and relative humidity, as quantified by the ventilation index, is shown in fig. 4.8. Climatologically, the ventilation index has a local maximum off the northern coastline of South America, which is where there is also a climatological maximum in vertical wind shear. The climatological ventilation index is largest in the MDR at the northern boundary of the EMDR, where vertical wind shear is high and relative humidity is low. The quartile difference shows a sizeable decrease in ventilation index for the northernmost $\overline{\Phi}_{TP}$ compared to the southernmost $\overline{\Phi}_{TP}$ off the coastline of South America and throughout a large portion of the WMDR. In this region, vertical wind shear is reduced for the northernmost $\overline{\Phi}_{TP}$, as described above, and SST is increased for the northernmost $\overline{\Phi}_{TP}$(not shown), which could cause a reduction in the ventilation index by increasing the potential intensity. The local maximum in the quartile difference in the EMDR, while intriguing, is only significant at the 80% level, which is not deemed sufficient to warrant further investigation here.

The connection between September mean $\overline{\Phi}_{TP}$, vertical wind shear and mid-tropospheric humidity is summarized in fig. 4.9 in the form of a pseudo-schematic. A poleward displacement

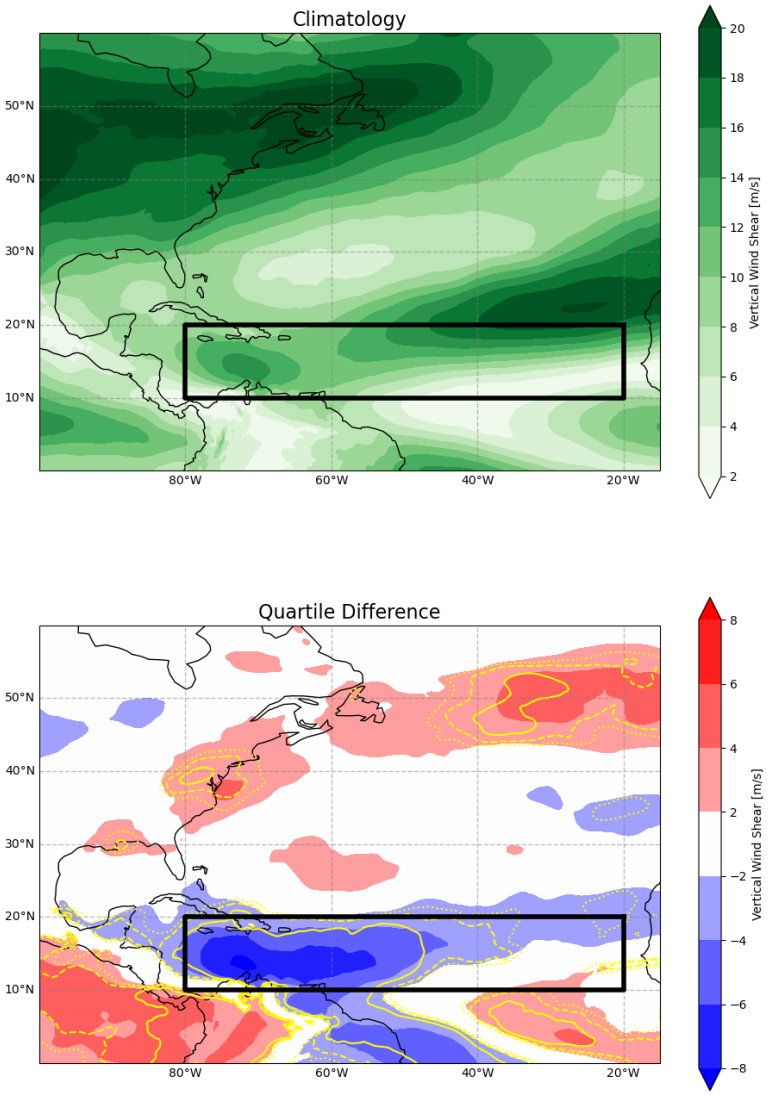

Figure 4.7: As fig. 4.5, but showing 200–850 hPa vertical wind shear.

of $\overline{\Phi}_{TP}$ is associated with reduced vertical wind shear and slightly increased relative humidity in favor of increased TC activity, while the opposite is the case for an equatorward displacement. The effect is mainly present in the WMDR.

4.4.5 Redundancy of Isentropic Levels as Predictors

$\overline{\Phi}_{TP}$ is linked to vertical wind shear in the WMDR on both the 350 K and 360 K isentropic surfaces, and thus there may be autocorrelation of $\overline{\Phi}_{TP}$ between isentropic surfaces. This is substantiated by Abatzoglou and Magnusdottir (2006) and Bowley et al. (2019), which both show that PV streamers can have a substantial vertical extent, and that the horizontal extent on the 360 K isentropic surface can greatly exceed the horizontal extent on the 350 K isentropic surface. However, Abatzoglou and Magnusdottir (2006) also show that during September in the North Atlantic basin, the vertical extent of PV streamers is decreased relative to the vertical extent in summer. Due to their counting method, it becomes clear that there are PV streamers on the 360 K isentropic surface that are not present on the 350 K isentropic surface. As $\overline{\Phi}_{TP}$ is not only determined by PV streamers, it should also be noted that $\overline{\Phi}_{TP}$ on the 350 K and 360 K isentropic surfaces can be controlled by the same underlying feature, such as a tropical upper-tropospheric

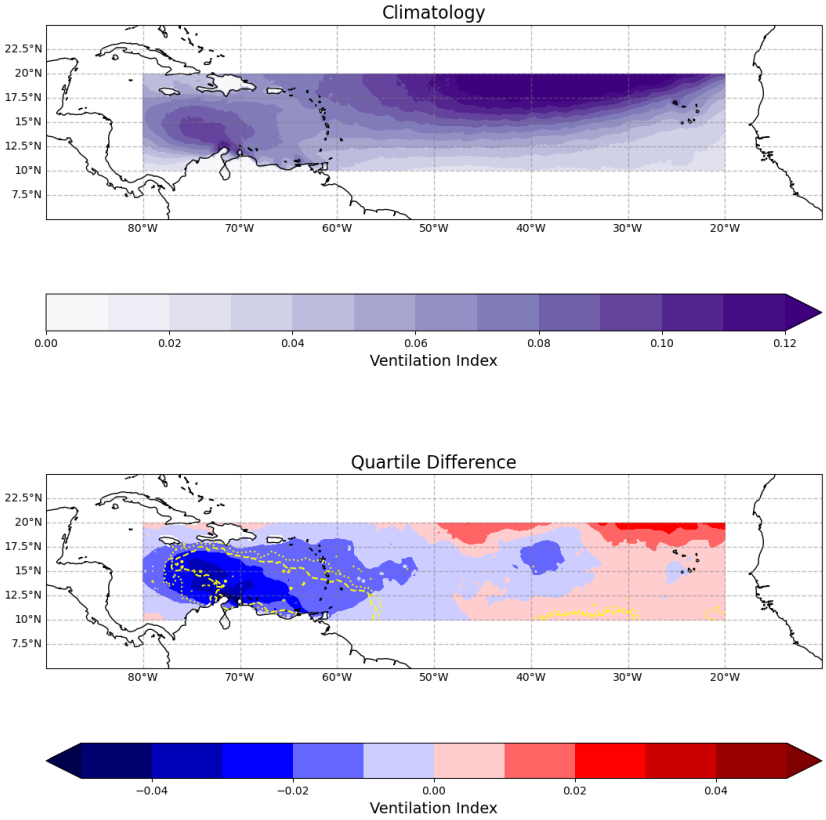

Figure 4.8: As fig. 4.5, but showing ventilation index in the MDR. The 99% confidence level is omitted to make the figure easier to read.

trough (TUTT, Fitzpatrick et al. (1995)). This, however, is not necessarily always the case. A quantification of how often an underlying feature controls $\overline{\Phi}_{TP}$ on both isentropic surfaces is not provided here, and speculation concerning such a quantification is intentionally avoided, as it is not deemed necessary for the following analysis. In light of these circumstances, $\overline{\Phi}_{TP}$ on the 350 K and 360 K isentropic surfaces could be at least partially redundant when used to predict the square root of ACE.

Multiple linear regression analysis is again used to assess whether using both isentropic surfaces is superior to the use of only one. The square root of ACE is predicted instead of ACE to detrend the residuals of the regression. This is necessary to ensure that the regression properly captures the relation between the dependent variable and the predictors. The latitudes where the correlation coefficient of $\overline{\Phi}_{TP}$ with seasonal ACE is maximal during September, as denoted in table 4.1, are used for this analysis. The results are summarized in table 4.4.

Using the 360 K isentropic surfaces yields a far larger R^2 value than using the 350 K isentropic surface (R^2=0.50 vs. R^2=0.32). When both isentropic surfaces are used, the R^2 value only increases very slightly. Further, the p value associated with the 350 K isentropic surface as a predictor is rather large (p>0.2). There is thus no tangible benefit to using both isentropic surfaces, and the 360 K isentropic surface appears to be the superior predictor.

4.5 Impact on Storm Number and Lifetime

From the definition of ACE, it follows that not only a reduced intensification via environmental variables can impact ACE, but also a reduction in named storm number or hurricane lifetime. This section assesses whether changes in September $\overline{\Phi}_{TP}$ on the 350 K and 360 K isentropic sur-

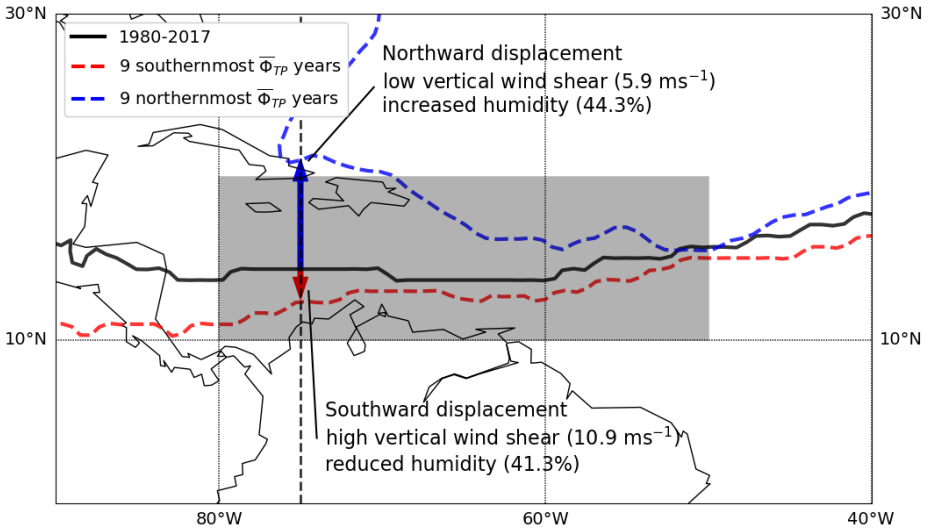

Figure 4.9: September mean 2 PVU contour position for 1980–2017 (solid black), the years with the 9 most equatorward September mean $\overline{\Phi}_{TP,360}$ (dashed red) and the 9 most poleward September mean $\overline{\Phi}_{TP,360}$ (dashed blue) using ERA5 data, and the WMDR (gray region). Arrows indicate poleward (blue) and equatorward (red) displacements of the 2 PVU contours relative to the 1980–2017 climatological 2 PVU contour at 75°W (the vertical dashed black line denotes the 75°W longitude line). WMDR mean 200–850 hPa vertical wind shear and 500 hPa relative humidity are given as text in the figure.

faces are linked to changes in named storm number or hurricane lifetime. Further, the number and ratio of TCs that make landfall is assessed, as this is when TCs pose the greatest and most immediate threat.

Table 4.5 summarizes the correlation coefficients of September $\overline{\Phi}_{TP}$ with the number of storm days, hurricane days, and named storms, the average hurricane lifetime, the number of TCs that make landfall, and the ratio of TCs that make landfall to the number of named storms throughout the entire North Atlantic hurricane season. The entire season is considered for these variables instead of only September, as this avoids the need for an arbitrary definition of how to treat systems that cross from one month into another, and because most of the climatological seasonal activity (>85% of ACE) occurs from August to October.

For all metrics, the difference from one isentropic surface to the other is generally rather small, with the ratio of TCs that make landfall showing the largest increase in correlation coefficient from 0.26 to 0.36. As all coefficients are positive, a more poleward $\overline{\Phi}_{TP}$ is favorable for TC formation and intensification for all considered metrics. Zhang et al. (2016) found that Rossby wave breaking frequency correlates with the North Atlantic hurricane frequency (r=-0.47) and the tropical storm frequency (r=-0.39). The correlation coefficients of $\overline{\Phi}_{TP}$ on both the 350 K and 360 K isentropic surfaces with the number of named storms are stronger in magnitude, as expected from the stronger correlation of $\overline{\Phi}_{TP}$ with ACE. Zhang et al. (2017) found that Rossby wave breaking frequency is correlated with hurricane count (r=-0.67) and the number of named storms (r=-0.48). They further found that Rossby wave breaking frequency correlates strongly with ACE (r=-0.73), which is close to the value found using September $\overline{\Phi}_{TP}$. The correlation with named storms is therefore stronger when using $\overline{\Phi}_{TP}$ instead of Rossby wave breaking frequency, but this does not appear to affect the correlation with ACE.

Table 4.4: As table 4.2, but predicting the square root of ACE with September mean $\overline{\Phi}_{TP}$ on the 350 K and 360 K isentropic levels, and using HURDAT2 to calculate ACE.

Model	β_1	p_{β_1}	β_2	p_{β_2}	adj. R^2	p(F)
$\sqrt{ACE} = \beta_1 \cdot \overline{\Phi}_{TP,350}$	21.5	$< 10^{-3}$			0.316	$< 10^{-3}$
$\sqrt{ACE} = \beta_1 \cdot \overline{\Phi}_{TP,360}$	16.4	$< 10^{-3}$			0.498	$< 10^{-3}$
$\sqrt{ACE} = \beta_1 \cdot \overline{\Phi}_{TP,350} + \beta_2 \cdot \overline{\Phi}_{TP,360}$	7.1	0.221	13.5	$< 10^{-3}$	0.506	$< 10^{-3}$

Table 4.5: Correlation coefficients of September mean $\overline{\Phi}_{TP}$ on the 350 K and 360 K isentropic surfaces (as per subscript) with storm days (SD), hurricane days (HD), number of named storms (NS), the lifetime of hurricanes (LT_{HU}), the number of TCs that make landfall (LF), and the ratio of TCs that make landfall to the number of named storms (q_{LF}). A single asterisk denotes significance at the 95% level, and two asterisks denote significance at the 99% level.

	SD	HD	NS	LT_{HU}	LF	q_{LF}
$\overline{\Phi}_{TP,350}$	0.67**	0.60**	0.64**	0.45**	0.61**	0.26
$\overline{\Phi}_{TP,360}$	0.66**	0.69**	0.61**	0.37*	0.68**	0.36*

The change in correlation coefficient with the ratio of TCs that make landfall is of particular note, as the associated p value decreases from 0.11 on the 350 K isentropic surface to 0.02 on the 360 K isentropic surface. The change in the number of TCs that make landfall is therefore not only a result of there being more named storms when $\overline{\Phi}_{TP}$ is more poleward, but TCs are also more likely to make landfall.

The number of storm days and hurricane days can also be considered for September only, as these metrics do not cross from one month into the next. On both considered isentropic surfaces, the correlation coefficients are reduced slightly. On the 350 K isentropic surface, they are reduced to 0.58 and 0.52 for storm days and hurricane days, respectively, down from 0.67 and 0.60 for the entire North Atlantic hurricane season. On the 360 K isentropic surface, they are similarly reduced to 0.55 and 0.66 for storm days and hurricane days, respectively, from 0.66 and 0.69 for the entire North Atlantic hurricane season. The number of storm days and hurricane days are linked to the intensity of cyclones, which in turn is linked to the response of vertical wind shear and relative humidity patterns to $\overline{\Phi}_{TP}$. As this response also exists in months other than September, as already mentioned for August, and because $\overline{\Phi}_{TP}$ is autocorrelated, it is concluded that autocorrelation aids in producing the high correlation between September $\overline{\Phi}_{TP}$ and seasonal mean number of storm days and hurricane days.

The lifetime of hurricanes can be affected by the location of their genesis. The northernmost and southernmost $\overline{\Phi}_{TP}$ quartiles on the 360 K isentropic surface years are compared in their respective genesis location distributions. The difference in seasonal genesis location density is shown in fig. 4.10 in the top panel. Differences in genesis location density are rather small throughout the EMDR (32% of TCs formed in the EMDR for both quartiles), while the WMDR is more active for more poleward $\overline{\Phi}_{TP}$ (29% of TCs in the northernmost $\overline{\Phi}_{TP}$ quartile and 18% of TCs in the southernmost $\overline{\Phi}_{TP}$ quartile formed in the WMDR). A more equatorward $\overline{\Phi}_{TP}$ favors

Table 4.6: Number of storm days (SD), hurricane days (HD), and named storms (NS), the lifetime of hurricanes (LT_{HU}, in number of synoptic time steps), the number of TCs that make landfall (LF), and the ratio of TCs that make landfall to the number of named storms (q_{LF}) for the northernmost $\overline{\Phi}_{TP}$ quartile ($\overline{\Phi}^N_{TP}$) and the southernmost $\overline{\Phi}_{TP}$ quartile ($\overline{\Phi}^S_{TP}$).

	SD	HD	NS	LT_{HU}	LF	q_{LF}
$\overline{\Phi}^N_{TP}$	76.4	41.7	17.4	36.3	10.2	0.59
$\overline{\Phi}^S_{TP}$	42.7	18.7	10.8	29.0	4.4	0.41

the region north of the WMDR, i.e. cyclogenesis at a more poleward location.

The bottom panel of fig, 4.10 shows the difference in the equivalent genesis location density using only TCs that were formed in September. The favored cyclogenesis location to the north of the MDR for more equatorward $\overline{\Phi}_{TP}$ years is present in September genesis locations as well. The EMDR is a slightly favored genesis location for more poleward $\overline{\Phi}_{TP}$ (42% of TCs in the northernmost $\overline{\Phi}_{TP}$ quartile and 38% of TCs in the southernmost $\overline{\Phi}_{TP}$ quartile formed in the EMDR), with the central EMDR in particular being favored in the northernmost $\overline{\Phi}_{TP}$ quartile. TCs therefore show a tendency to be generated not only closer to the extratropics, but on average also closer to the North American coastline in years with a more equatorward $\overline{\Phi}_{TP}$. The differences in genesis location density are consistent with a reduced lifetime for a more equatorward $\overline{\Phi}_{TP}$. While a pattern emerges, it is not exceptionally strong, which is consistent with the comparatively low correlation coefficient of $\overline{\Phi}_{TP}$ with hurricane lifetime (see table 4.5).

Table 4.6 shows the metrics used for correlations in table 4.5, with the absolute numbers listed for the northernmost and southernmost $\overline{\Phi}_{TP}$ quartiles. The corresponding tracks are shown in fig. 4.11. In total, the southernmost $\overline{\Phi}_{TP}$ years produced 41 TCs starting in September, and the northernmost $\overline{\Phi}_{TP}$ years produced 42 TCs starting in September. While the difference seems small, the number of produced hurricanes is 22 and 32, respectively. This is consistent with the forecast failure of 2013 and the analysis of Zhang et al. (2016), which indicated that while TCs are generated in the presence of high Rossby wave breaking activity, their intensification is impeded. Note that table 4.6 provides numbers for the entire season, so while the number of TCs in September is similar in both quartiles, the number of TCs throughout the season still differs substantially. For a more northern $\overline{\Phi}_{TP}$, there is an increase in landfall events particularly in the Gulf of Mexico, but there appears to be a reduction of events along the eastern coast of North America. This is consistent with genesis being favored in the region north of the MDR for the southernmost September $\overline{\Phi}_{TP}$ positions, as TCs generated in that region do not typically enter the Gulf of Mexico, but preferentially make landfall along the eastern coast of North America. The reduction in landfall opportunities is consistent with the lower number of landfall events and the reduced landfall ratio for the southernmost $\overline{\Phi}_{TP}$ quartile in table 4.6. The northernmost $\overline{\Phi}_{TP}$ quartile shows an increase in cyclogenesis in the EMDR, as also seen in fig. 4.10. Although the ratio of TCs that make landfall is increased in the northernmost $\overline{\Phi}_{TP}$ quartile, many of the TCs originating in the EMDR recurve without making landfall, which increases their lifetime compared to TCs forming further west which make landfall, as also reflected in the increased hurricane lifetime in table 4.6. It is thus visible that changes in genesis location density affect landfall location and frequency, as well as hurricane lifetime.

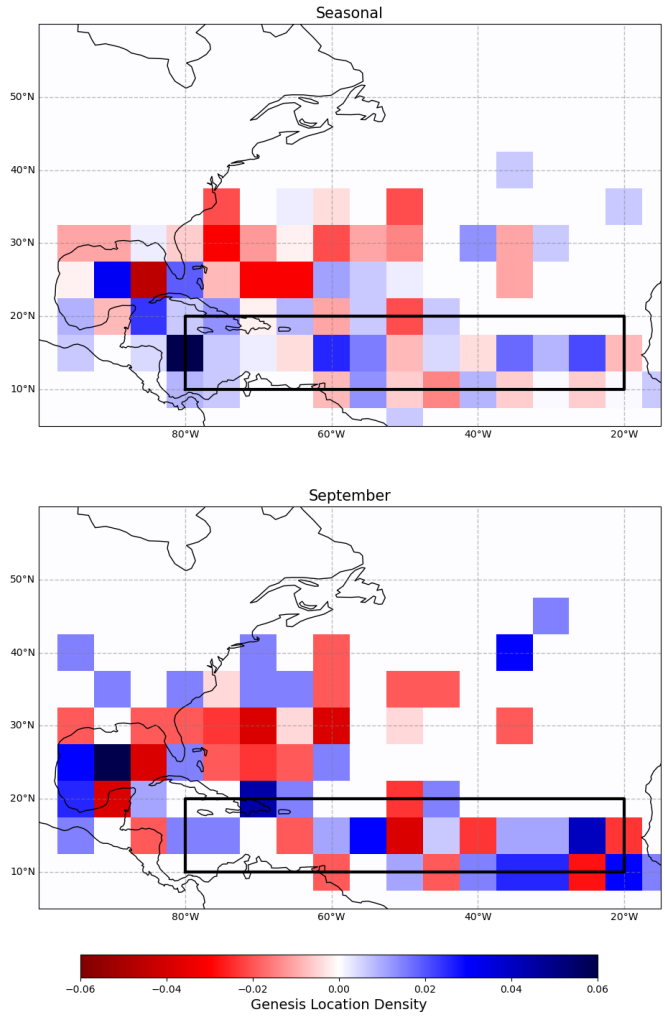

Figure 4.10: Difference in genesis location density of the northernmost $\overline{\Phi}_{TP}$ quartile and the southernmost $\overline{\Phi}_{TP}$ quartile for all TCs within the North Atlantic hurricane season (top) and TCs formed in September (bottom). The region outlined in black is the MDR.

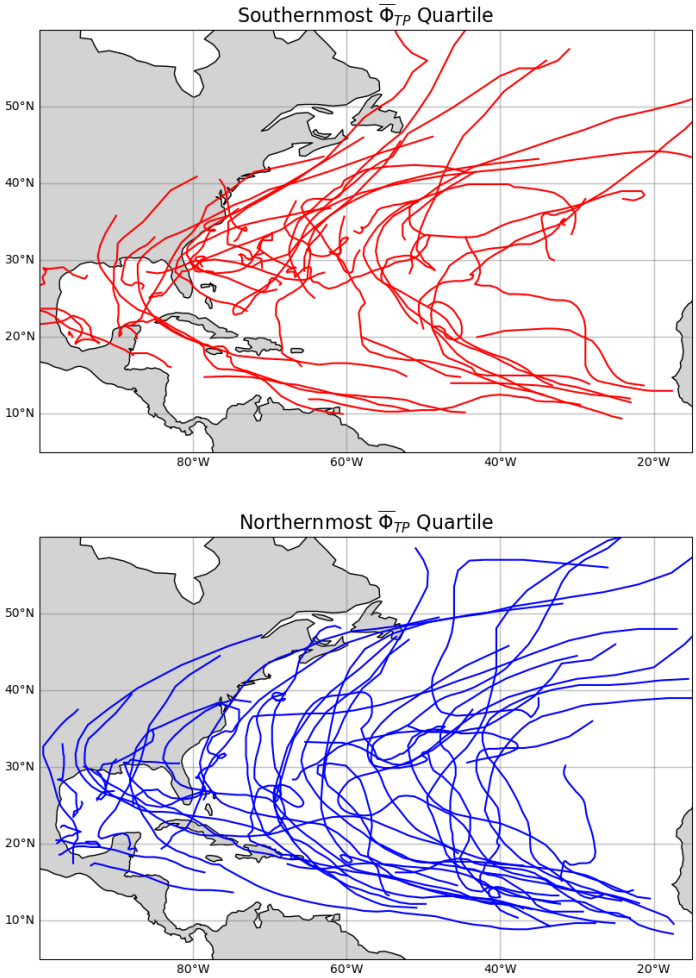

Figure 4.11: Tracks of TCs generated in September for the 9 southernmost September $\overline{\Phi}_{TP}$ years (top) and the 9 northernmost September $\overline{\Phi}_{TP}$ years (bottom).

4.6 Summary and Conclusions

$\overline{\Phi}_{TP}$ was introduced as a metric to describe the influence of the latitude of the 2 PVU contour on an isentropic surface on TC activity. Using ERA5 and HURDAT2 data, the correlation of monthly mean $\overline{\Phi}_{TP}$ with TC activity as quantified by ACE was found to vary greatly from month to month, and strongly depends on the longitude of $\overline{\Phi}_{TP}$, as well as the isentropic surface. Particularly strong correlations of $\overline{\Phi}_{TP}$ on the 350 K and 360 K isentropic surfaces with ACE were found during the month of September in the western North Atlantic basin. Weaker but still substantial correlation was found during the month of June throughout the central North Atlantic basin for $\overline{\Phi}_{TP}$ on the 350 K isentropic surface. It is thus concluded that September $\overline{\Phi}_{TP}$ on the 360 K isentropic surface shows potential as a useful predictor for seasonal ACE in mid-season hybrid-approach forecasting (i.e., a combination of statistical and dynamical forecasting). This, however, depends on the capability to predict $\overline{\Phi}_{TP}$ with a lead time of about two months, which is not addressed here. June $\overline{\Phi}_{TP}$ on the 350 K isentropic surface has some potential to be a useful predictor in pre-season forecasting, though not to the same extent as September $\overline{\Phi}_{TP}$ for mid-season forecasting.

Multiple linear regression analysis was used to assess the link between September $\overline{\Phi}_{TP}$, 200 hPa - 850 hPa vertical wind shear and 850–200 hPa precipitable water in several sub-regions of the North Atlantic basin. It was found that $\overline{\Phi}_{TP}$ on the 350 K isentropic surface affects vertical wind shear in the MDR and in the HIR, but that there is no tangible effect on precipitable water in the MDR. $\overline{\Phi}_{TP}$ on the 360 K isentropic surface affects mainly vertical wind shear in the western MDR, but also has a tangible effect on vertical wind shear in the eastern MDR and the HIR. In the western MDR, there is a substantial effect on precipitable water. It was argued that this change is due to a region of high PV streamer frequency on the 360 K isentropic surface intruding into the western MDR from August to September. It is concluded that these impacts allow September $\overline{\Phi}_{TP}$ to influence ACE by changing environmental factors relevant to TC intensification.

The northernmost and southernmost quartiles of $\overline{\Phi}_{TP}$ on the 360 K isentropic surface were compared to each other. The comparison shows a significant increase in 600 hPa relative humidity in parts of the WMDR, and a significant decrease in vertical wind shear throughout most of the WMDR for the northernmost $\overline{\Phi}_{TP}$ quartile. As a consequence, the ventilation index is significantly decreased throughout a large section of the WMDR for the northernmost $\overline{\Phi}_{TP}$ quartile.

Finally, the correlation of September $\overline{\Phi}_{TP}$ with a number of metrics related to TC activity and lifetime was assessed. In particular, September $\overline{\Phi}_{TP}$ substantially correlates with the number of storm days, hurricane days, and named storms throughout the entire season. Further, there is substantial correlation of $\overline{\Phi}_{TP}$ on the 360 K isentropic surface with the ratio of TCs making landfall to the number of named storms. $\overline{\Phi}_{TP}$ on the 350 K isentropic surface shows much weaker correlation. September $\overline{\Phi}_{TP}$ is further correlated with the average lifetime of hurricanes throughout the season. A reason for this was presented in the form of a shift of cyclogenesis location, as a more equatorward September $\overline{\Phi}_{TP}$ on the 360 K isentropic surface shows a tendency for cyclones to form closer to coastlines and closer to the extratropics in the western North Atlantic, and fewer to form in the eastern MDR during September. It is concluded that September $\overline{\Phi}_{TP}$ influences seasonal ACE not only by affecting cyclone intensity via environmental factors, but also by affecting TC genesis locations and thereby their lifetimes. September $\overline{\Phi}_{TP}$, in particular on the 360 K isentropic surface, is therefore concluded to show possible potential for use as a predictor for a number of TC activity metrics.

We recommend to conduct further research on how specifically the $\overline{\Phi}_{TP}$ metric can be integrated into existing seasonal and sub-seasonal prediction frameworks. Also, due to the link of $\overline{\Phi}_{TP}$ to Rossby wave breaking frequency, it is speculated that changes in $\overline{\Phi}_{TP}$ could lead to changes in the relative frequency of different tropical cyclogenesis pathways. This has ramifications for the predictability of tropical cyclogenesis with varying $\overline{\Phi}_{TP}$.

Chapter 5

The Mean Tropopause Latitude in Numerical Simulations

Abstract

The September mean tropopause latitude on the 360 K isentropic surface in the western North Atlantic region is linked to both seasonal and September accumulated cyclone energy in the North Atlantic basin. The regional variant of the ICON model is used to assess whether this link is present in numerical simulations. The simulations do not reproduce the interannual variability of tropical cyclone activity and the mean tropopause latitude in the western North Atlantic region very well, and underestimate tropical cyclone activity. However, a clear and significant link between the tropopause latitude and accumulated cyclone energy is found. Further, variations in tropopause latitude are found to be linked to significant changes in vertical wind shear that are qualitatively consistent with the corresponding changes found in ERA5 reanalysis data. Significant changes in ventilation index are also found, are partially consistent with the corresponding changes in ERA5 data, and are of an appropriate magnitude.

5.1 Introduction

Tropical cyclones (TCs) are powerful weather systems that can lay waste to coastlines upon making landfall. The potential damage they cause is projected to increase as coasts become more populated and the concentration of wealth increases (Pielke Jr. et al., 2008). In a warming climate, hurricanes of categories 4 and 5 are projected to become more frequent(Bender et al., 2010) and more destructive (Grinsted et al., 2019). It is therefore of interest to predict the impact of TCs ahead of time, both as individual TCs become acutely dangerous in short-term forecasts, and on a seasonal scale, where mitigation and relief can be planned on a longer time scale.

Seasonal predictions were first attempted by Nicholls (1979) for the Australian region. In the North Atlantic region, Gray (1984a,b) made first attempts at seasonal prediction by relating the number of hurricanes and hurricane days to El Niño events, the quasi-biennial oscillation, and Caribbean sea level pressure anomalies during spring. This approach, where a statistical connection between any phenomenon and TC activity is used to produce forecasts, is termed statistical forecasting, and has since been continuously developed (e.g., Klotzbach and Gray (2004); Saunders and Lea (2005); Klotzbach (2007)).

Another method of forecasting is to use dynamical models, within which TC activity can be assessed. While numerical models can produce TC-like systems even at low resolutions, these are typically larger and weaker than observed TCs (Manabe et al., 1970; Bengtsson et al., 1982). However, even unrealistic TC-like systems can be used to derive useful information on the geographical and seasonal distribution of TCs (Bengtsson et al., 1995). Murakami et al. (2015)

found that a horizontal resolution of 25 km or higher is required for numerical models to adequately represent very intense TCs, and Gentry and Lackmann (2010) showed in a case study that even at very high resolutions, a further increase from 8 km to 1 km can reduce the minimum pressure of a TC by 30 hPa. As an increase in resolution comes at a high computational cost, regional models can be used to limit the domain of the simulation. Knutson et al. (2007) used a regional model to simulate North Atlantic TCs with a regional modeling where they nudged the large scale environment towards reanalysis data. They underestimated TC intensity, but made use of an empirical relation between central surface pressure and maximum wind speeds to reproduce TC activity based on central surface pressure. Patricola et al. (2014) performed regional simulations with a horizontal resolution of 27 km and without nudging. They produced TCs that were too weak, but overestimated the accumulated cyclone energy (ACE, Bell et al. (2000)) by almost 20%, as they generated too many TCs.

Dynamical forecasting can be combined with statistical forecasting to form a hybrid approach. The hybrid approach uses numerical models not to predict TCs directly, but to predict the future state of the atmosphere, i.e. the environment within which TCs will exist, and base their predictions on these environmental variables. Dynamical and hybrid forecasting has been shown to be skillful (e.g., Thorncroft and Pytharoulis (2001); Vitart et al. (2007); Vecchi et al. (2014); Zhang et al. (2019)). Operational TC forecasts have generally been found to not only have skill in predicting the number of TCs, but also have the capability to provide information on landfall locations and regional activity (Klotzbach et al., 2019).

The 2013 North Atlantic hurricane season was forecast to be above average in activity by various forecasting agencies. In reality, only two category one hurricanes occurred, and no major hurricanes, which is far below average. The total number of TCs was adequately forecast, though, which implies that forecasts underestimated the intensity of storms, and not their number. Zhang et al. (2016) proposed that an abundance of anticyclonic Rossby wave breaking events caused a decrease in mid-tropospheric humidity and an increase in vertical wind shear. These two quantities work in tandem to increase the ventilation of the TC, which mixes relatively dry air into the system and thereby impede intensification (Riemer et al., 2010; Tang and Emanuel, 2010, 2012; Riemer and Laliberté, 2015). Zhang et al. (2016) draw special attention to the very equatorward position of the August mean 2 potential vorticity unit (PVU) contour on the 350 K isentropic surface. The 2 PVU contour can be used to identify Rossby wave breaking by identifying potential vorticity (PV) streamers, which are elongated filaments emerging from the high-PV stratosphere into the low-PV troposphere. PV streamers can be used as a proxy for anticyclonic Rossby wave breaking (Wernli and Sprenger, 2007; Béguin et al., 2013; Sprenger et al., 2017).

PV streamers can be reliably identified (e.g., Bowley et al. (2019); Papin et al. (2020)), and Rossby wave breaking has been studied extensively in reanalysis data (e.g., Postel and Hitchman (1999); Scott and Cammas (2002); Abatzoglou and Magnusdottir (2006); Wernli and Sprenger (2007)). Predictions of Rossby wave breaking in numerical models, however, show biases in frequency and location(Barnes and Hartmann, 2012). Béguin et al. (2013) found that the bias in Rossby wave breaking frequency in the largest in the North Atlantic region, and that the bias of the 2 PVU contour latitude is lower than that of the Rossby wave breaking latitude. They thus conclude that the bias in Rossby wave breaking location is not exclusively a result of the bias in the 2 PVU contour location, but of where along the contour wave breaking occurs.

The link between Rossby wave breaking and PV streamer behaviour and TC activity has been the subject of recent scientific attention. Li et al. (2018) found that on a short time scale of 8 days, Rossby wave breaking is essentially uncorrelated with ACE when they use their entire dataset from 1985 to 2013. However, there is significant correlation during a few individual years, which may be due to interannual variability of the correlation. On a seasonal time scale,

TC activity has been shown to significantly correlate negatively with Rossby wave breaking frequency and and the area of the breaking wave (Zhang et al., 2017), as well as with a metric that combines the frequency, size and magnitude of the anomaly of PV streamers (Papin et al., 2020). The link between TC activity and Rossby wave breaking is generally limited to Rossby wave breaking on the 350 K isentropic surface. The impact of PV streamers on TC activity is not exclusively negative, as their presence can enable tropical cyclogenesis via tropical transition (Takemura and Mukougawa, 2021), a process where a precursor cyclone attains characteristics of a TC, such as axisymmetry and a warm core (Davis and Bosart, 2003). TCs formed via tropical transition account for over one third of North Atlantic TCs (McTaggart-Cowan et al., 2013), but tropically transitioned TCs are less predictable than TCs that did not undergo tropical transition (Wang et al., 2018). While PV streamers affect TC activity in different ways, their overall effect is a reduction in TC activity (Zhang et al., 2017).

Chapter 4 of this thesis has demonstrated that the latitude of the 2 PVU contour in the western North Atlantic region can potentially be used instead of a quantification of PV streamer activity to predict TC activity, and that the 360 K isentropic surface can be used instead of the more commonly used 350 K isentropic surface to make these predictions. A requirement for this is that numerical models can reproduce the results found in reanalysis and observational data. This chapter thus aims to use the numerical model ICON (Zängl et al., 2015) to assess its capability in reflecting the results of chapter 4.

The remainder of this chapter is structured as follows. Section 5.2 describes the data and methods used within this chapter. Section 5.3 validates the simulations results, specifically in the capability of the numerical model to reproduce ACE, relevant physical fields, and $\overline{\Phi}_{TP}$. Section 5.4 assesses the link of $\overline{\Phi}_{TP}$ to ACE, and section 5.5 assesses the link to environmental variables, in the numerical simulations. Section 5.6 summarizes the results and conclusions.

5.2 Data and Methods

The numerical model used in this chapter is ICON (Zängl et al., 2015) version 2.6.4 in limited area mode (ICON-LAM). The years 1980 to 2021 are simulated from August 1 to October 4, with the analysis of the results being focused on September. This is done because September is the most active month, and because it was shown in chapter 4 of this thesis that the link between the 2 PVU contour position and ACE is strongest in September. The horizontal resolution is R03B07, which corresponds to about 13 km. 50 vertical levels are used, with the lowest level at 10 m, the model top at 23 km, and the distance between levels increasing with height. A time step of 100 s is used. Both shallow and deep convection parametrizations are used (Bechtold et al., 2008). The simulation domain is from the equator to 70°N and from 120°W to 15°W, as shown in fig. 5.1.

For each year, three ensemble simulations are performed. All simulations use ERA5 (Hersbach et al., 2020) data to provide forcing for sea surface temperature and sea ice cover, which are both available as monthly means for the individual years and interpolated to individual time steps.

ERA5 ensemble data assimilation (ENDA) members 0–2 are used to provide the initial conditions and lateral boundary conditions. ENDA members correspond to the ensemble members produced by ICON, i.e. ICON member 0 uses ENDA member 0 initial and lateral boundary conditions, ICON member 1 uses ENDA member 1 initial and lateral boundary conditions, etc. Lateral boundary data are available in 6-hourly time steps, and prescribe zonal, meridional and vertical wind, the logarithm of sea level pressure, temperature, specific humidity, cloud liquid water content, cloud ice water content, rain water content, snow water content, and surface geopotential. They are interpolated to individual time steps. To further perturb the simulations,

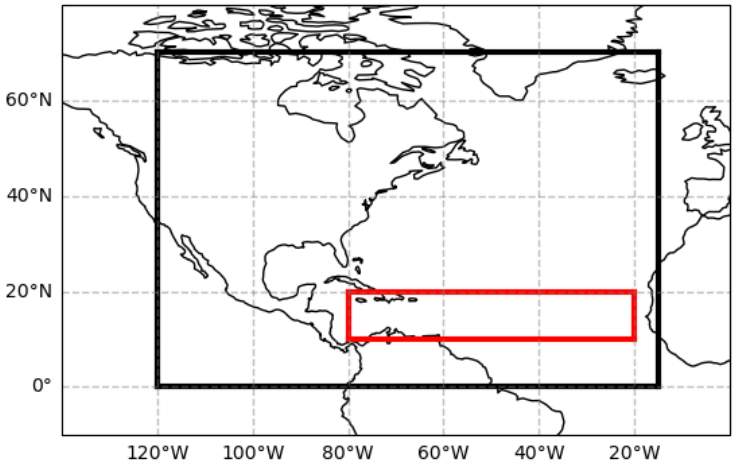

Figure 5.1: Numerical simulation domain (black) and the main development region of North Atlantic TCs (red).

the physical parametrizations are perturbed. The perturbation is applied randomly, depending on the ensemble member number.

The 2 PVU contour is identified using the algorithm of Sprenger et al. (2017), both for ERA5 and ICON data. ICON data are remapped to a 1°x1° grid. The algorithm detects the 2 PVU contour in evenly spaced intervals of 75 km distance. The 2 PVU contour is detected on the 360 K isentropic surface in September monthly mean PV fields. $\overline{\Phi}_{TP}$ is defined as the mean latitude of the 2 PVU contour within a longitudinal window of 5° half-width, i.e. as a longitudinal running mean of the 2 PVU contour latitude.

ACE is defined as

$$ACE = \sum_{i=1}^{k} v_{max,i}^2 \tag{5.1}$$

where $i = 1$ is the initial time, k is the final time, and v_{max} is the maximum wind speed of any given TC at a given time. 6-hourly data are used, and only the month of September is considered, as motivated above. Within ICON data, a TC is defined as any system detected by the tracking algorithm of chapter 3 of this thesis, that at the given time step has at least the intensity of a tropical storm (TS), i.e. a maximum wind speed of at least 17 ms^{-1}. HURDAT2 observational data (Landsea and Franklin, 2013) are used as a reference. Any system that is denoted as TS or HU (hurricane) at a given time in HURDAT2 data is included in ACE. Only the month of September is considered for ACE. Within ICON data, TS days are defined as the number of days on which a TC with a maximum wind speed of at least 17 m/s was present in the North Atlantic basin. This includes TCs at hurricane strength. Hurricane days are defined likewise, but only include TCs with a maximum wind speed of at least 33 m/s. Within HURDAT2 data, TS days and hurricane days are defined similarly, but instead of maximum wind speed use the provided TS and HU designation to determine whether a system is at TS or HU strength. As with ACE, only the month of September is considered for TS days and hurricane days. For storms that begin in August and persist into September, or begin in September and persist into October,

only the portion that falls into September is considered.

Vertical wind shear (VWS) is defined as the magnitude of the vector difference of the horizontal wind between 200 hPa and 850 hPa, i.e.:

$$VWS = \sqrt{(u_{200} - u_{850})^2 + (v_{200} - v_{850})^2} \tag{5.2}$$

where u is the zonal wind, v is the meridional wind, and the indices denote the pressure level in hPa. Precipitable water (PW) is calculated within the same pressure interval as VWS. VWS is calculated for 6-hourly time steps for the month of September, and then averaged to form a monthly mean. PW is calculated from September monthly mean data.

The ventilation index (VI) of Tang and Emanuel (2012) is used to quantify the combined effect of vertical wind shear and mid-tropospheric humidity. It is defined as

$$VI = \frac{VWS \cdot \chi_m}{u_{PI}} \tag{5.3}$$

where u_{PI} is the potential intensity as defined by Bister and Emanuel (2002), and χ_m is the entropy deficit, defined as:

$$\chi_m = \frac{s_m^* - s_m}{s_{SST}^* - s_b} \tag{5.4}$$

where s_m^* is the saturation entropy at 600 hPa, s_m is the entropy at 600 hPa, s_{SST}^* is the saturation entropy at the sea surface, and s_b is the entropy in the boundary layer. Entropy is calculated according to the pseudo-adiabatic entropy calculation in Bryan (2008). VI is calculated from monthly means, following Tang and Emanuel (2012), based on 6-hourly data.

The main development region (MDR, Goldenberg and Shapiro (1996)), as shown in fig. 5.1, spans from 10°N to 20°N and from 80°W to 20°W. It is further differentiated into the eastern and western MDR (EMDR and WMDR, respectively), with the boundary being at 50°W.

5.3 Validation of Simulation Results

The performance of the numerical simulations must be assessed. This is done only for the month of September, as the link between ACE and $\overline{\Phi}_{TP}$ is strongest in September (see chapter 4). Figure 5.2 shows the capability of the numerical simulations to reproduce TC related metrics and $\overline{\Phi}_{TP}$ during September. While ACE, $\overline{\Phi}_{TP}$, the number of TS days and the number of hurricane days are all within a reasonable range, some issues arise. The numerical simulations do not seem to be able to produce very high values of ACE, which is a strong deviation from HURDAT2 data in 2004 and 2017. It may be unexpected that the year 2004 has a very high ACE value, and the year 2005 does not, but it should be pointed out that Katrina (2005) occurred entirely in August, and that Wilma (2005), the second most intense TC in the western hemisphere, occurred entirely in October, and are therefore not included. While the simulations did produce a few category 5 hurricanes, i.e. TCs with a maximum wind speed of 70 m/s or higher, these are very rare, not sustained for longer than one time step, and did not occur in the 2004 or 2017 simulations during September. The simulations therefore underestimate the intensity of the most intense TCs. This is likely due to the horizontal resolution of 13 km, which is sufficient to produce major hurricanes, but insufficient to reproduce the most extreme cases (e.g., Gentry and Lackmann (2010)). ACE for the year 2017 is grossly underestimated despite being very active

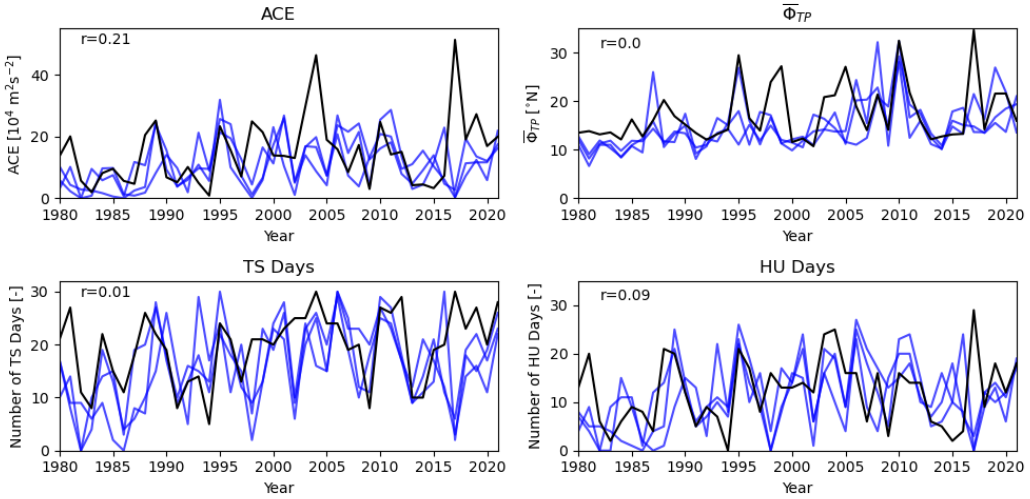

Figure 5.2: 1980–2021 ACE (top left), $\overline{\Phi}_{TP}$ on the 360 K isentropic surface (top right), TS days (bottom left) and hurricane days (bottom right). Black lines show HURDAT2-based data (ERA5 for $\overline{\Phi}_{TP}$), and blue lines show ICON-based data of individual ensemble members. r denotes the correlation coefficient of HURDAT2 and ERA5 data with the ensemble mean of the ICON data. Only the month of September is considered.

in observations, though more ensemble members would be required to conclude that there is a systematic issue with this specific year. The simulations produce an average ACE of 10.9 m^2s^{-2}, while HURDAT2 data show an average of 14.8 m^2s^{-2}. The simulations thus produce only about 74% of the observed ACE, which is the opposite of the results of Patricola et al. (2014), who used a horizontal resolution of 27 km and overestimated ACE by 20%. The simulation ensemble mean ACE shows weak correlation with HURDAT2 ACE, which is not significant at the 90% level. The interannual variability of September ACE is thus not reproduced adequately.

Simulated $\overline{\Phi}_{TP}$ on the 360 K isentropic surface is roughly within the same range as ERA5 $\overline{\Phi}_{TP}$ on the 360 K isentropic surface. However, the mean temporal average $\overline{\Phi}_{TP}$ of the numerical simulations is still slightly too far equatorwards at 14.6°N, compared to the temporal average $\overline{\Phi}_{TP}$ in ERA5 data at 17.4°N. This is similar to the results of Béguin et al. (2013), who found the 2 PVU contours too far equatorward in their numerical simulations, though on other isentropic surfaces. The correlation between the ensemble mean simulated $\overline{\Phi}_{TP}$ and ERA5 $\overline{\Phi}_{TP}$ is essentially zero, so it is concluded that the interannual variability of $\overline{\Phi}_{TP}$ on the 360 K isentropic surface is not reproduced in the simulations.

The number of TS days and the number of hurricane days are generally within an adequate range. The average number of TS days in the simulations is 16.0, compared to 19.7 in HURDAT2, and the average number of hurricane days are 11.2 and 12.1, respectively. The occurrence of TCs is thus generally underestimated, which, in conjunction with not being able to produce the most extreme TC intensities, explains the reduced average ACE of the numerical simulations compared to observations. The correlation coefficients of the numerical simulation results with observations are very weak in both cases, because the interannual variability of TS and hurricane days is not adequately reproduced, even though ERA5 data are used to prescribe the simulation domain boundaries and sea surface temperature.

In summary, the numerical simulations do not reproduce the interannual variability of TC related metrics and $\overline{\Phi}_{TP}$, produce a too low TC activity, and place $\overline{\Phi}_{TP}$ slightly too far equatorwards. A likely cause for this is the low number of ensemble members, as Roberts et al. (2020) found that an increase in ensemble size can greatly improve the correlation with observations for TC related metrics, with the improvement being largest at low ensemble size. They further find

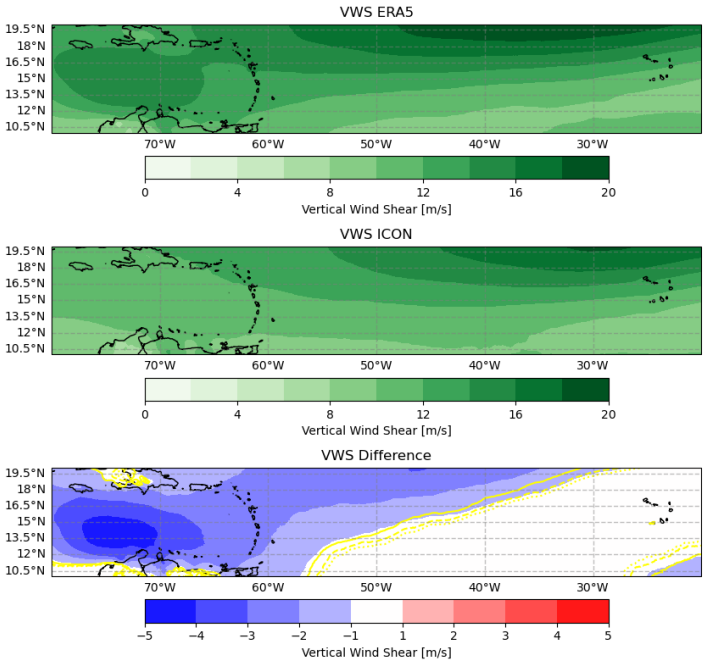

Figure 5.3: 1980–2021 September monthly mean vertical wind shear in the MDR in ERA5 data (top,), the ICON ensemble mean (center), and the difference between ICON and ERA5 data (bottom). Yellow contours denote p-values indicating 99% (solid), 95% (dashed) and 90% (dotted) significance.

a very large spread in correlations of individual ensemble members with observations, which is also the case in the numerical simulations presented here.

Even though interannual variability is not reproduced adequately, it is still possible for the link between $\overline{\Phi}_{TP}$ and ACE, and the link between $\overline{\Phi}_{TP}$ and vertical wind shear, precipitable water and ventilation index in the WMDR, to be reproduced. Figure 5.3 shows a comparison of vertical wind shear in the MDR for ERA5 and for the ICON ensemble mean. The numerical simulations reproduce vertical wind shear reasonably well in the EMDR, with values increasing polewards, but underestimating shear at the northern boundary. In the WMDR, vertical wind shear is significantly underestimated almost everywhere, and, notably, the local maximum to the north of South America is absent in the numerical simulations. The magnitude of this local maximum is significantly linked to the $\overline{\Phi}_{TP}$ position on the 360 K isentropic surface in ERA5 data (see chapter 4). Section 5.5 will show that this link is still significant in the numerical simulation data, even though the climatological local maximum is absent.

Figure 5.4 shows the precipitable water in the MDR within ERA5 and the ICON ensemble mean data. Qualitatively, the results are similar, as precipitable water increases westwards and equatorwards within the MDR in both cases. However, with the exception of a small region at the eastern boundary of the MDR, the ICON ensemble mean exhibits increased precipitable water. The increase is about 5% to 10% relative to ERA5 data, but significant at the 99% level. The ICON ensemble mean mid-tropospheric humidity is thus overestimated.

The ventilation index is shown in fig. 5.5. Throughout most of the WMDR, the ventilation index is underestimated by the numerical simulations, which is a result of the reduced vertical wind shear and the increased mid-tropospheric humidity. Consequently, the difference in ventilation index is the largest north of the South American coast, where the local maximum in vertical wind shear is not reproduced in the numerical simulations. The reduced ventilation of TCs in the WMDR is likely to have a positive impact on ACE, as TCs can attain higher intensity with less ventilation. Consequently, ACE would be underestimated even more if vertical wind shear, and thus ventilation index, were reproduced better. However, with only the western third of the

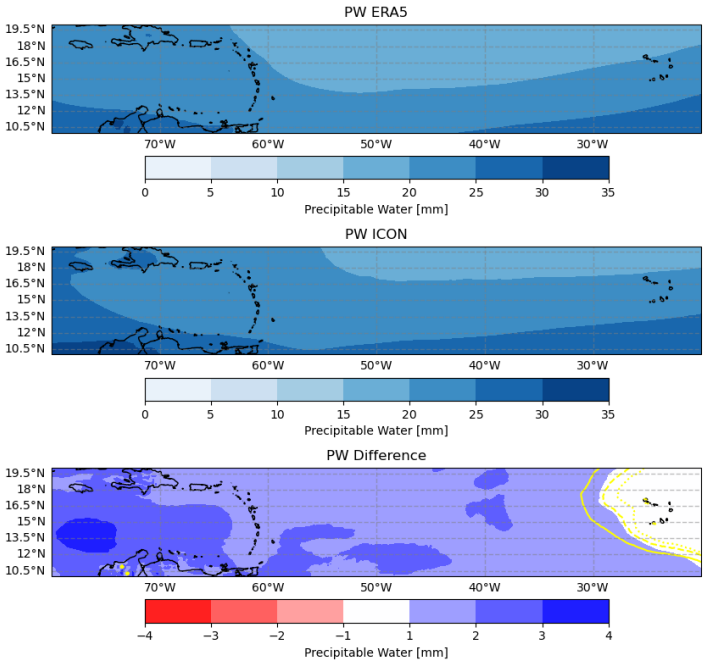

Figure 5.4: As fig 5.3, but showing precipitable water.

MDR being particularly affected, it is difficult to estimate how large the impact would be.

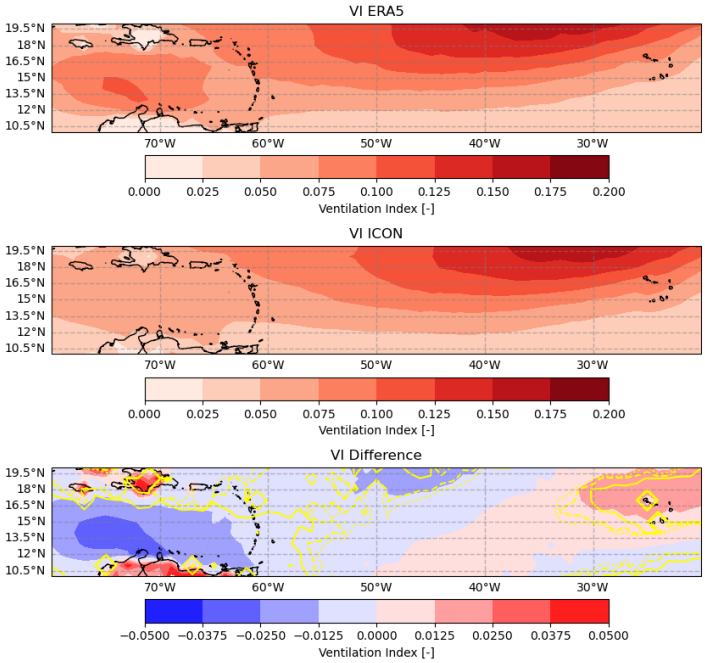

Figure 5.5: As fig 5.3, but showing ventilation index.

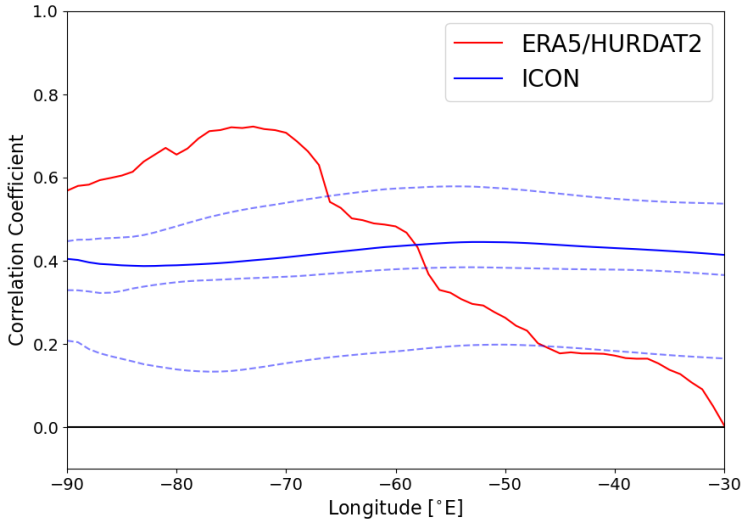

Figure 5.6: Correlation coefficient of 1980–2021 September mean $\overline{\Phi}_{TP}$ on the 360 K isentropic surface per longitude with 1980–2021 basin wide ACE during the month of September. ERA5 data (red), the ICON ensemble mean (blue, solid) and individual ICON ensemble members (blue, dashed) are shown.

5.4 Mean Tropopause Latitude Link to ACE

In chapter 4, it was shown that $\overline{\Phi}_{TP}$ on the 360 K isentropic surface correlates quite well with seasonal ACE. Figure 5.6 shows the correlation of $\overline{\Phi}_{TP}$ on the 360 K isentropic surface per longitude with basin wide ACE, but unlike in chapter 4, ACE is only calculated for September, and four more years are included (2018–2021). The results presented here for ERA5 and HURDAT2 data are very similar to those in chapter 4 (see fig. 4.2), but the maximum in correlation coefficient is at 73°W, as opposed to 74°W in chapter 4. The ICON results differ strongly from the ERA5 and HURDAT2 results. First, the difference in correlation coefficient between ensemble members is very large. As only three ensemble members are used, the results are naturally sensitive to the inclusion or exclusion of individual members, and a larger ensemble size would provide more robust results. Second, the dependency of the correlation coefficient on the longitude is not reproduced. Instead, the correlation coefficient is somewhat steady throughout the zonal extent of the considered range, especially for the ensemble mean, and peaks between 60°W and 50°W. However, the ensemble mean correlation coefficient at 73°W is still about 0.4, and significant at the 95% level. Therefore, a link between $\overline{\Phi}_{TP}$ on the 360 K isentropic surface and basin wide ACE during September is reproduced by the model simulations.

The weak dependence of the correlation coefficient on longitude in fig. 5.6 for ICON data is likely due to zonal autocorrelation of $\overline{\Phi}_{TP}$. The zonal autocorrelation is shown in fig. 5.7, which shows that within the considered longitudinal range, the ensemble mean $\overline{\Phi}_{TP}$ on the 360 K isentropic surface at 73°W correlates very strongly (r>0.95) with all other longitudes. This is not the case in the ERA5 data. The cause for the zonal autocorrelation is not known, and this feature is not present in previous global simulations with ICON (not shown).

In conclusion, the link between September mean $\overline{\Phi}_{TP}$ on the 360 K isentropic surface and basin wide September ACE is partially reproduced in numerical simulations. The correlation coefficients gained from the numerical simulations are far lower than those gained from ERA5 and HURDAT2 data, and the longitudinal dependence is not reproduced. However, a clear and significant correlation has been found nevertheless.

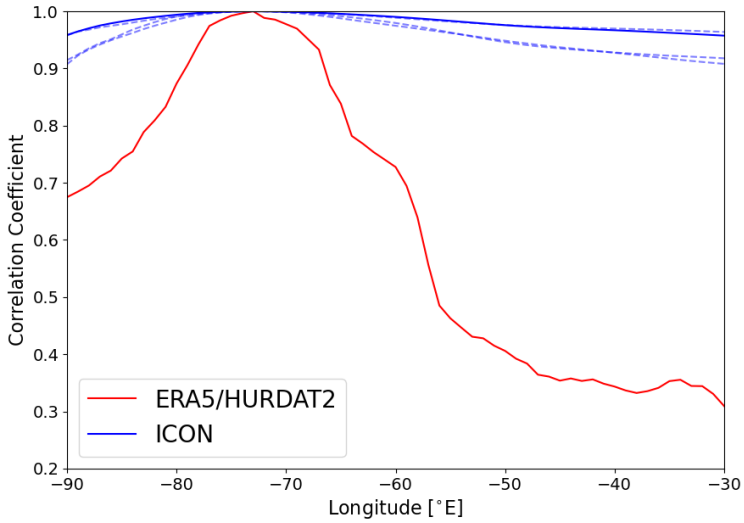

Figure 5.7: Correlation coefficient of 1980–2021 September mean $\overline{\Phi}_{TP}$ on the 360 K isentropic surface per longitude with itself at 73°W. ERA5 data (red), the ICON ensemble mean (blue, solid) and individual ICON ensemble members (blue, dashed) are shown.

5.5 Mean Tropopause Latitude Link to Environmental Variables

The numerical simulations produced data for 42 years. The ten years with the southernmost and the ten years with the northernmost $\overline{\Phi}_{TP}$ on the 360 K isentropic surface at 73°W in the simulation ensemble mean, henceforth called the southernmost and northernmost $\overline{\Phi}_{TP}$ quartile, respectively, are investigated further. The aim is to detect differences in the ventilation index between the two quartiles, as shown in fig. 5.8. As vertical wind shear and 600 hPa humidity are included in the ventilation index, they are also shown separately, with humidity being quantified by relative humidity.

The quartile difference shows that variations in $\overline{\Phi}_{TP}$ on the 360 K isentropic surface are linked to significant changes in vertical wind shear throughout large parts of the MDR. Vertical wind shear is reduced in the WMDR, in particular where ERA5 data show a climatological local maximum, even though this maximum is not present in the numerical simulation data. This is consistent with the results of chapter 4, which show significant changes in this region as well. Further consistent is the reduction in vertical wind shear in the northern half of the EMDR in the northernmost $\overline{\Phi}_{TP}$ quartile. Differences arise in a small region in the south-eastern WMDR, where vertical wind shear is slightly increased, and to the south of the central MDR, where vertical wind shear is also increased, which is not the case in ERA5 data (see fig. 4.7). Overall, the size of the region where vertical wind shear is significantly reduced in the northernmost $\overline{\Phi}_{TP}$ quartile in the WMDR is underestimated, and the magnitude of the quartile difference is underestimated as well. However, the results of chapter 4 are qualitatively reproduced within most of the MDR.

In the results of chapter 4, 600 hPa relative humidity shows significant changes between quartiles only in a comparatively small region at around 60°W (see fig. 4.5). The quartile difference in the ICON ensemble mean data presented here overestimates the difference, as they show a significant difference throughout most of the MDR. This has ramifications for the ventilation index, where a significant difference between quartiles is detected throughout most of the MDR, whereas this was only detected north of the coast of South America for ERA5 data in chapter 4 (see fig. 4.8). As the vertical wind shear quartile difference is reproduced at least qualitatively, the underestimation of the ventilation index in the numerical simulation data is likely caused by

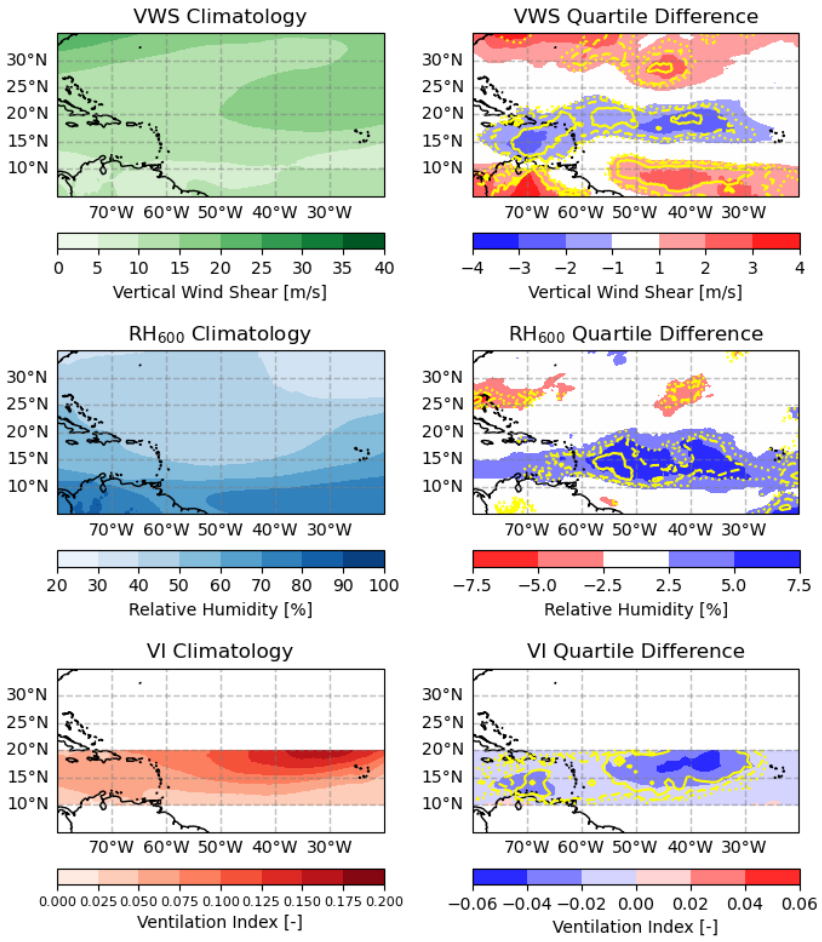

Figure 5.8: 1980–2021 simulation ensemble mean climatology (left) and difference between the northernmost and southernmost $\overline{\Phi}_{TP}$ quartile (right) vertical wind shear (top), relative humidity at 600 hPa (center) and ventilation index (bottom). The 600 hPa relative humidity quartile difference panel uses a reversed color scale.

this large change in relative humidity quartile difference. To the north off the coast of South America, the magnitude of the quartile difference in ventilation index is consistent with that found in chapter 4, as the quartile difference in 600 hPa relative humidity is reproduced adequately in this region.

In summary, the numerical simulations reproduce the quartile difference in ventilation index that was found in chapter 4 in the region north of the coast of South America quite well, but underestimate the ventilation index throughout other parts of the MDR. The reason for this is that the quartile difference in 600 hPa relative humidity is overestimated.

5.6 Summary and Conclusions

Numerical simulations were performed to assess how well the ICON model can reproduce the results of chapter 4 of this thesis. While the inclusion of only three ensemble members complicates the interpretation of the results, some valuable information can still be gained. An expansion to an ensemble size of ten members is therefore highly recommended, and currently pending.

ACE, $\overline{\Phi}_{TP}$ on the 360 K isentropic surface, and the number of TS and hurricane days are all underestimated by the numerical simulations. $\overline{\Phi}_{TP}$ on the 360 K isentropic surface being too far equatorward is consistent with the simulations of Béguin et al. (2013), who found similar

behavior on lower isentropic surfaces. ACE and the number of TS and hurricane days are likely underestimated due to a too coarse horizontal resolution, which is exacerbated by limiting the data to the month of September. As September is within the peak of the North Atlantic hurricane season, it is liable to exhibit extremely intense TCs. The numerical simulations are not able to sustain TCs with maximum wind speeds of over 70 m/s (i.e., category 5 hurricanes) for longer than one 6-hourly time step, which would constitute large contributions to ACE if they existed for a prolonged time. The interannual variability of ACE, $\overline{\Phi}_{TP}$ on the 360 K isentropic surface, and TS and hurricane days is not reproduced well, but this does not mean that the numerical simulations are unable to reproduce the link between $\overline{\Phi}_{TP}$ on the 360 K isentropic surface and ACE.

It is found that there is a significant link between $\overline{\Phi}_{TP}$ on the 360 K isentropic surface and ACE in the numerical simulation data. In contrast to the results of chapter 4, this link persists throughout a very wide zonal range, but the correlation coefficient is far lower (r≈0.4) than that found in ERA5 and HURDAT2 data in chapter 4. The difference in ventilation index between the northernmost $\overline{\Phi}_{TP}$ quartile and the southernmost $\overline{\Phi}_{TP}$ quartile is adequately reproduced north of the coast of South America, but is overestimated throughout large sections of the MDR. The reason for this is that the quartile difference in 600 hPa relative humidity is overestimated in large sections of the MDR.

Chapter 6

Conclusion and Outlook

6.1 Summary

6.1.1 Validation of the Tropical Cyclone Tracking Algorithm

A tropical cyclone tracking algorithm was developed for use with the ICON model. The algorithm uses parameter threshold variation to enable the detection of weak systems and weak stages of intense systems while still being sufficiently restrictive to not have false positives significantly impact the accumulated cyclone energy.

The algorithm successfully detects TCs, has the capability to begin tracking during the aggregation stage of TCs, and terminates TCs when they interact strongly with extratropical flow or their warm core dissipates. The algorithm can also track systems that do not intensify to TS strength, which is of use for applications that distinguish intensifying from non-intensifying disturbances. ACE was shown to not be significantly impacted by faulty tracking, and thus the algorithm is concluded to adequately represent the ACE value of the underlying data.

6.1.2 Influence of Potential Vorticity Structure on North Atlantic Tropical Cyclone Activity

The latitude of the 2 PVU contour on the 360 K isentropic surface in the western North Atlantic region was shown to correlate strongly with seasonal ACE. Similar to the impact of Rossby wave breaking influence on ACE, it was shown that the 2 PVU contour position impacts ACE via changes to vertical wind shear and mid-tropospheric humidity in the MDR, but limited to the western half of the MDR. The geographical location of Rossby wave breaking was shown to be less important than the frequency and area of Rossby wave breaking events in impacting ACE, even when the highest frequency of Rossby wave breaking is located outside of the MDR. It is thus concluded that the 2 PVU contour position has potential for use in seasonal and subseasonal TC forecasting.

Importantly, the 2 PVU contour latitude does not only hold information on ACE. The geographical distribution of cyclogenesis and landfall locations, as well as the probability of landfall, are also linked to the 2 PVU contour latitude. The regional damage potential along the coastline of North America is therefore also impacted, which is directly relevant to disaster relief preparation and mitigation work.

6.1.3 The Mean Tropopause Latitude in Numerical Modeling

The ICON atmosphere model was used to produce regional ensemble simulations covering the North Atlantic basin. While the interpretation of results is frustrated by the small ensemble size of only three members, useful information was still gained. The numerical simulations do not reproduce the interannual variability of basin-wide September TC activity and the September

mean tropopause latitude in the western North Atlantic region well, and generally underestimate TC activity. Regardless, a significant link between the September mean tropopause latitude on the 360 K isentropic surface and basin-wide September ACE is shown to be present.

The September mean tropopause latitude on the 360 K isentropic surface is shown to be linked to significant changes in vertical wind shear and ventilation index, which are partially consistent with the results of chapter 4. Changes in mid-tropospheric humidity are not reproduced well, as significant changes in 600 hPa relative humidity cover a very large area in the numerical simulation data, which is not the case in ERA5 data. As a result, significant changes in ventilation index also cover an area that is substantially larger than found in ERA5 data. The numerical simulations still show promise, as the link between the September mean tropopause latitude and September mean ventilation index is clearly demonstrated.

6.2 Outlook

While the performance of the TC tracking algorithm is adequate, improvements can be made. First, the use of weak constraints successfully detects TC tracks during their aggregation phase in many cases. The OWZ parameter is particularly useful in achieving the same goal, and a comparison of the two methods would reveal whether including the OWZ parameter in the current tracking algorithm would be beneficial. Second, the maximum allowed translational velocity is currently responsible for terminating many storms that interact with extratropical flow. The maximum translational velocity is tailored towards merging detected TCs in individual time steps into tracks, and can thus not be optimized for its use in TC termination. An explicit treatment of extratropical transition would aid in terminating TCs more consistently, and would allow for more control over algorithm behavior.

A unified tracking scheme for tropical and extratropical cyclones could be developed based on the current framework. This scheme would primarily track surface pressure minima, use the detection of a warm core to distinguish between tropical and extratropical cyclones, and would allow for both tropical and extratropical transition. The resulting scheme would be beneficial for any research that aims to investigate the transition processes in particular. As these transition processes are highly relevant, the continues development of the tracking scheme is recommended.

The 2 PVU contour latitude on the 360 K isentropic surface in the western North Atlantic region correlates strongly with seasonal ACE, but no attempt to implement this metric in actual forecasting has been made. A sensible next step is therefore to either test the 2 PVU contour latitude as an initial sole predictor for TC activity, and to build a prediction framework from this, or to implement the 2 PVU contour latitude into existing prediction frameworks. As vertical wind shear and mid-tropospheric humidity are already used as predictors in some frameworks, special attention would have to be given to assessing the redundancy of predictors, and their specific role, as the 2 PVU contour also holds relevant information on the geographical distribution of TCs and landfall locations. While not stated in the chapter itself, there is no relevant correlation between the 2 PVU contour position in the western North Atlantic and the 30 hPa and 50 hPa QBO index. This implies that the change in wind direction described in chapter 4 is not directly linked to the QBO (which is consistent with the findings of Shapiro (1989)). However, there may still be a link between the 2 PVU contour position and the QBO that is more difficult to detect, and further research in this direction may be warranted.

A hybrid forecasting framework using the 2 PVU contour could be constructed. The use of hybrid forecasting would not require high horizontal resolution, as TCs would not need to be represented directly. Therefore, the focus of the framework would be to accurately incorporate and predict large scale features which are statistically linked to TC activity. This, in principle, includes any large scale feature that has predictive power, such as North Atlantic SST, QBO, or

teleconnection patterns, provided that they are not found to be redundant.

The results of the numerical simulations can be improved in different ways. First, an increase in ensemble size to ten members would likely improve the representation of ACE, and make the results more robust. An increase in horizontal resolution might also be required to improve the representation of ACE, which would come at a considerable computational cost. However, this appears necessary to sustain extremely intense TCs. Alternatively, it is possible to forgo the production of intense TCs entirely, and to instead reduce horizontal resolution to expand the domain to a global one without drastically increasing the computational cost. This would likely result in a reduced zonal autocorrelation in the September mean tropopause latitude in the North Atlantic region, and could improve the link between the September mean tropopause latitude and the September mean ventilation index, bringing it more in line with the ERA5 results. However, a direct link to ACE may not be possible at a reduced horizontal resolution. In light of the long time series and large ensemble size that are required to produce viable and robust results, the latter option seems to be more attractive in the near future.

List of Symbols and Abbreviations

$-V_T^L$	Extratropical Transition Thermal Wind Metric, page 8
χ_m	Entropy Deficit, page 3
η	Absolute Vorticity, page 10
$\nabla\theta$	Gradient of Potential Temperature, page 10
$\overline{\Phi}_{TP}$	Mean Tropopause Latitude, page 48
ρ	Density, page 5
$\mathbf{V}$	Wind Vector, page 3
ζ	Vertical Relative Vorticity, page 3
B	Storm-Relative Thickness Asymmetry, page 7
C_E	Surface Latent Heat Flux Transfer Coefficient, page 3
E	Stretching Deformation, page 10
F	Shearing Deformation, page 10
f	Coriolis Parameter, page 3
F_{q_v}	Surface Latent Heat Flux, page 3
h	Extratropical Transition Onset Hemisphere Indicator, page 7
M	Angular Momentum, page 4
p	Pressure, page 5
q_s	Saturation Specific Humidity, page 3
q_v	Specific Humidity, page 3
r	Radius from Cyclone Center, page 4
s_b	Boundary Layer Entropy, page 4
s_m	Entropy at 600 hPa, page 4
s_m^*	Saturation Entropy at 600 hPa, page 4
s_{SST}^*	Saturation Entropy at the Sea Surface, page 4
u	Zonal Wind, page 49
u_{PI}	Potential Intensity, page 3
V	Tangential Wind Speed, page 4
v	Meridional Wind, page 49
VWS	Vertical Wind Shear, page 49
Z	Geometric Height, page 7
Z_{MAX}	Maximum Isobaric Height, page 8
Z_{MIN}	Minimum Isobaric Height, page 8
AEW	African easterly wave, page 3
AO	Arctic Oscillation, page 9
CAPE	Convectively Available Potential Energy, page 17
DWD	German Weather Service, page 15
ECMWF	European Centre for Medium-Range Weather Forecasts, page 9
EMDR	Eastern Main Development Region, page 49
ENDA	Ensemble Data Assimilation, page 71
ENSO	El Niño-Southern Oscillation, page 8
HIR	High Intensity Region, page 49
ICON	Icosahedral Nonhydrostatic Atmosphere Model, page 15
ITCZ	Intertropical Convergence Zone, page 57
LES	Large Eddy Simulation, page 15

MDR	Main Development Region, page 6
MPI-M	Max-Planck-Institute for Meteorology, page 15
n mi	nautical mile, page 14
NAO	North Atlantic Oscillation, page 9
NASH	North Atlantic subtropical high-pressure system, page 7
NHC	National Hurricane Center, page 14
NICAM	Nonhydrostatic ICosahedral Atmosphere Model, page 15
OW	Okubo-Weiss parameter, page 10
OWZ	Okubo-Weiss-Zeta Parameter, page 10
PNA	Pacific-North-American Pattern, page 9
PV	Potential Vorticity, page 10
PVU	Potential Vorticity Unit, page 10
PW	Precipitable Water, page 73
QBO	Quasi-Biennial Oscillation, page 8
RCL	Recurving Landfall, page 7
RCO	Recurving Ocean, page 7
RRTM	Rapid Radiation Transfer Model, page 16
SM	Straight Moving, page 6
SST	Sea Surface Temperature, page 3
TC	Tropical Cyclone, page 1
TKE	Turbulent Kinetic Energy, page 17
TUTT	Tropical Upper-Tropospheric Trough, page 61
UTC	Coordinated Universal Time, page 14
VHT	Vortical Hot Tower, page 4
VI	Ventilation Index, page 3
WMDR	Western Main Development Region, page 49

List of Figures

List of Tables

Bibliography

Abatzoglou, J. T. and Magnusdottir, G.: Planetary wave breaking and nonlinear reflection: Seasonal cycle and interannual variability, Journal of Climate, 19, 6139–6152, https://doi.org/10.1175/JCLI3968.1, 2006.

Aiyyer, A. R. and Thorncroft, C.: Climatology of vertical wind shear over the tropical Atlantic, Journal of Climate, 19, 2969–2983, https://doi.org/10.1175/JCLI3685.1, 2006.

Barnes, E. A. and Hartmann, D. L.: Detection of Rossby wave breaking and its response to shifts of the midlatitude jet with climate change, Journal of Geophysical Research: Atmospheres, 117, https://doi.org/10.1029/2012JD017469, 2012.

Bechtold, P., Chaboureau, J.-P., Beljaars, A., Betts, A. K., Köhler, M., Miller, M., and Redelsperger, J.-L.: The simulation of the diurnal cycle of convective precipitation over land in a global model, Quarterly Journal of the Royal Meteorological Society, 130, 3119–3137, https://doi.org/10.1256/qj.03.103, 2004.

Bechtold, P., Köhler, M., Jung, T., Doblas-Reyes, F., Leutbecher, M., Rodwell, M. J., Vitart, F., and Balsamo, G.: Advances in simulating atmospheric variability with the ECMWF model: From synoptic to decadal time-scales, Quarterly Journal of the Royal Meteorological Society, 134, 1337–1351, https://doi.org/10.1002/qj.289, 2008.

Befort, D. J., Hodges, K. I., and Weisheimer, A.: Seasonal prediction of tropical cyclones over the North Atlantic and Western North Pacific, Journal of Climate, 35, 1385–1397, https://doi.org/10.1175/JCLI-D-21-0041.1, 2022.

Bell, G. D., Halpert, M. S., Schnell, R. C., Higgins, R. W., Lawrimore, J., Kousky, V. E., Tinker, R., Thiaw, W., Chelliah, M., and Artusa, A.: Climate Assessment for 1999, Bulletin of the American Meteorological Society, 81, S1–S50, https://doi.org/10.1175/1520-0477(2000)81[s1:CAF]2.0.CO;2, 2000.

Bell, S. S., Chand, S. S., Tory, K. J., and Turville, C.: Statistical Assessment of the OWZ Tropical Cyclone Tracking Scheme in ERA-Interim, Journal of Climate, 31, 2217–2232, https://doi.org/10.1175/JCLI-D-17-0548.1, 2018.

Bender, M. A., Knutson, T. R., Tuleya, R. E., Sirutis, J. J., Vecchi, G. A., Garner, S. T., and Held, I. M.: Modeled impact of anthropogenic warming on the frequency of intense Atlantic hurricanes, Science, 327, 454–458, https://doi.org/10.1126/science.1180568, 2010.

Bengtsson, L., Böttger, H., and Kanamitsu, M.: Simulation of hurricane-type vortices in a general circulation model, Tellus, 34, 440–457, https://doi.org/10.1111/j.2153-3490.1982.tb01833.x, _eprint: https://onlinelibrary.wiley.com/doi/pdf/10.1111/j.2153-3490.1982.tb01833.x, 1982.

Bengtsson, L., Botzet, M., and Esch, M.: Hurricane-type vortices in a general circulation model, Tellus A, 47, 175–196, https://doi.org/10.1034/j.1600-0870.1995.t01-1-00003.x, 1995.

Bieli, M., Sobel, A. H., Camargo, S. J., Murakami, H., and Vecchi, G. A.: Application of the cyclone phase space to extratropical transition in a global climate model, Journal of Advances in Modeling Earth Systems, 12, e2019MS001 878, https://doi.org/10.1029/2019MS001878, 2020.

Bister, M. and Emanuel, K. A.: Low frequency variability of tropical cyclone potential intensity 1. Interannual to interdecadal variability, Journal of Geophysical Research: Atmospheres, 107, ACL 26–1–ACL 26–15, https://doi.org/10.1029/2001JD000776, 2002.

Bourdin, S., Fromang, S., Dulac, W., Cattiaux, J., and Chauvin, F.: Intercomparison of four tropical cyclones detection algorithms on ERA5, https://doi.org/10.5194/egusphere-2022-179, 2022.

Bowley, K. A., Gyakum, J. R., and Atallah, E. H.: A new perspective toward cataloging northern hemisphere Rossby wave breaking on the dynamic tropopause, Monthly Weather Review, 147, 409–431, https://doi.org/10.1175/MWR-D-18-0131.1, 2019.

Bryan, G. H.: On the Computation of Pseudoadiabatic Entropy and Equivalent Potential Temperature, Monthly Weather Review, 136, 5239–5245, https://doi.org/10.1175/2008MWR2593.1, 2008.

Béguin, A., Martius, O., Sprenger, M., Spichtinger, P., Folini, D., and Wernli, H.: Tropopause level Rossby wave breaking in the Northern Hemisphere: a feature-based validation of the ECHAM5-HAM climate model, International Journal of Climatology, 33, 3073–3082, https://doi.org/https://doi.org/10.1002/joc.3631, _eprint: https://rmets.onlinelibrary.wiley.com/doi/pdf/10.1002/joc.3631, 2013.

Camargo, S. J. and Zebiak, S. E.: Improving the detection and tracking of tropical cyclones in atmospheric general circulation models, Weather and Forecasting, 17, 1152 – 1162, https://doi.org/10.1175/1520-0434(2002)017<1152:ITDATO>2.0.CO;2, 2002.

Chauvin, F., Royer, J.-F., and Déqué, M.: Response of hurricane-type vortices to global warming as simulated by ARPEGE-Climat at high resolution, Climate Dynamics, 27, 377–399, https://doi.org/10.1007/s00382-006-0135-7, 2006.

Colbert, A. J. and Soden, B. J.: Climatological variations in North Atlantic tropical cyclone tracks, Journal of Climate, 25, 657–673, https://doi.org/10.1175/JCLI-D-11-00034.1, 2012.

Davis, C. A. and Bosart, L. F.: Baroclinically Induced Tropical Cyclogenesis, Monthly Weather Review, 131, 2730–2747, https://doi.org/10.1175/1520-0493(2003)131<2730:BITC>2.0.CO;2, 2003.

Davis, C. A. and Bosart, L. F.: The TT Problem: Forecasting the Tropical Transition of Cyclones, Bulletin of the American Meteorological Society, 85, 1657–1662, publisher: American Meteorological Society, 2004.

Dorel, L., Ardilouze, C., Déqué, M., Batté, L., and Guérémy, J.-F.: Documentation of the Météo-France pre-operational seasonal forecasting system, Météo France, 2017.

Durden, S. L.: Observed tropical cyclone eye thermal anomaly profiles extending above 300 hPa, Monthly Weather Review, 141, 4256–4268, https://doi.org/10.1175/MWR-D-13-00021.1, 2013.

Emanuel, K.: Divine Wind: The History and Science of Hurricanes, Oxford University Press, Oxford, New York, 2005.

Emanuel, K., DesAutels, C., Holloway, C., and Korty, R.: Environmental Control of Tropical Cyclone Intensity, Journal of the Atmospheric Sciences, 61, 843–858, https://doi.org/10.1175/1520-0469(2004)061<0843:ECOTCI>2.0.CO;2, 2004.

Emanuel, K. A.: An air-sea interaction theory for tropical cyclones. Part I: Steady-state maintenance, Journal of the Atmospheric Sciences, 43, 585–605, https://doi.org/10.1175/1520-0469(1986)043<0585:AASITF>2.0.CO;2, 1986.

Evans, J. L. and Hart, R. E.: Objective indicators of the life cycle evolution of extratropical transition for atlantic tropical cyclones, Monthly Weather Review, 131, 909–925, https://doi.org/10.1175/1520-0493(2003)131<0909:OIOTLC>2.0.CO;2, 2003.

Fitzpatrick, P. J., Knaff, J. A., Landsea, C. W., and Finley, S. V.: Documentation of a Systematic Bias in the Aviation Model's Forecast of the Atlantic Tropical Upper-Tropospheric Trough: Implications for Tropical Cyclone Forecasting, Weather and Forecasting, 10, 433–446, https://doi.org/10.1175/1520-0434(1995)010<0433:DOASBI>2.0.CO;2, 1995.

France, M.: Météo-France seasonal forecast system 5 for Eurosip, Météo France Tech. Rep., 2015.

Frank, W. M. and Ritchie, E. A.: Effects of Vertical Wind Shear on the Intensity and Structure of Numerically Simulated Hurricanes, Monthly Weather Review, 129, 2249–2269, https://doi.org/10.1175/1520-0493(2001)129<2249:EOVWSO>2.0.CO;2, 2001.

Fröhlich, K., Dobrynin, M., Isensee, K., Gessner, C., Paxian, A., Pohlmann, H., Haak, H., Brune, S., Früh, B., and Baehr, J.: The German Climate Forecast System: GCFS, Journal of Advances in Modeling Earth Systems, 13, e2020MS002 101, https://doi.org/10.1029/2020MS002101, 2021.

Gentry, M. S. and Lackmann, G. M.: Sensitivity of simulated tropical cyclone structure and intensity to horizontal resolution, Monthly Weather Review, 138, 688 – 704, https://doi.org/10.1175/2009MWR2976.1, 2010.

Gettelman, A., Collins, W. D., Fetzer, E. J., Eldering, A., Irion, F. W., Duffy, P. B., and Bala, G.: Climatology of Upper-Tropospheric Relative Humidity from the Atmospheric Infrared Sounder and Implications for Climate, Journal of Climate, 19, 6104–6121, https://doi.org/10.1175/JCLI3956.1, 2006.

Goldenberg, S. B. and Shapiro, L. J.: Physical Mechanisms for the association of El Niño and West African rainfall with Atlantic major hurricane activity, Journal of Climate, 9, 1169–1187, 1996.

Gray, W. M.: Global view of the origin of tropical disturbances and storms, Monthly Weather Review, 96, 669–700, https://doi.org/10.1175/1520-0493(1968)096<0669:GVOTOO>2.0.CO;2, 1968.

Gray, W. M.: Tropical cyclone genesis, Dept. of Atmos. Sci. Paper No. 234, Colo. State Univ., Ft. Collins, CO, p. 121 pp., 1975.

Gray, W. M.: Atlantic seasonal hurricane frequency. Part I: El Niño and 30 mb Quasi-Biennial Oscillation influences, Monthly Weather Review, 112, 1649–1668, https://doi.org/10.1175/1520-0493(1984)112<1649:ASHFPI>2.0.CO;2, 1984a.

Gray, W. M.: Atlantic seasonal hurricane frequency. Part II: Forecasting its variability, Monthly Weather Review, 112, 1669–1683, https://doi.org/10.1175/1520-0493(1984)112<1669:ASHFPI>2.0.CO;2, 1984b.

Gray, W. M., Landsea, C. W., Mielke, P. W., and Berry, K. J.: Predicting Atlantic Seasonal Hurricane Activity 6–11 Months in Advance, Weather and Forecasting, 7, 440–455, https://doi.org/10.1175/1520-0434(1992)007<0440:PASHAM>2.0.CO;2, 1992a.

Gray, W. M., Sheaffer, J. D., and Knaff, J. A.: Effect of stratospheric QBO on ENSO variability, Journal of the Meteorological Society of Japan. Ser. II, 70, 975–995, https://doi.org/10.2151/jmsj1965.70.5_975, 1992b.

Grinsted, A., Ditlevsen, P., and Christensen, J. H.: Normalized US hurricane damage estimates using area of total destruction, 19002018, Proceedings of the National Academy of Sciences, 116, 23 942–23 946, https://doi.org/10.1073/pnas.1912277116, 2019.

Gualdi, S., Borrelli, A., Cantelli, A., Davoli, G., del Mar Chaves Montero, M., Masina, S., Navarra, A., Sanna, A., and Tibaldi, S.: The new CMCC Operational Seasonal Prediction System, CMCC Tech. Rep., p. 34 pp., https://doi.org/10.25424/CMCC/SPS3.5, 2020.

Hart, R. E. and Evans, J. L.: A climatology of the extratropical transition of Atlantic tropical cyclones, Journal of Climate, 14, 546–564, https://doi.org/10.1175/1520-0442(2001)014<0546:ACOTET>2.0.CO;2, 2001.

Haurwitz, B.: The height of tropical cyclones and of the "eye" of the storm, Monthly Weather Review, 63, 45–49, 1935.

Hendricks, E. A., Peng, M. S., Fu, B., and Li, T.: Quantifying Environmental Control on Tropical Cyclone Intensity Change, Monthly Weather Review, 138, 3243–3271, https://doi.org/10.1175/2010MWR3185.1, 2010.

Hersbach, H., Bell, B., Berrisford, P., Hirahara, S., Horányi, A., Muñoz-Sabater, J., Nicolas, J., Peubey, C., Radu, R., Schepers, D., Simmons, A., Soci, C., Abdalla, S., Abellan, X., Balsamo, G., Bechtold, P., Biavati, G., Bidlot, J., Bonavita, M., De Chiara, G., Dahlgren, P., Dee, D., Diamantakis, M., Dragani, R., Flemming, J., Forbes, R., Fuentes, M., Geer, A., Haimberger, L., Healy, S., Hogan, R. J., Hólm, E., Janisková, M., Keeley, S., Laloyaux, P., Lopez, P., Lupu, C., Radnoti, G., de Rosnay, P., Rozum, I., Vamborg, F., Villaume, S., and Thépaut, J.-N.: The ERA5 global reanalysis, Quarterly Journal of the Royal Meteorological Society, 146, 1999–2049, https://doi.org/https://doi.org/10.1002/qj.3803, 2020.

Hodges, K. I.: Adaptive Constraints for Feature Tracking, Monthly Weather Review, 127, 1362–1373, https://doi.org/10.1175/1520-0493(1999)127<1362:ACFFT>2.0.CO;2, 1999.

Holland, G. J.: Tropical cyclone motion: Environmental interaction plus a beta effect, Journal

of the Atmospheric Sciences, 40, 328–342, https://doi.org/10.1175/1520-0469(1983)040<0328:TCMEIP>2.0.CO;2, 1983.

Horn, M., Walsh, K., Zhao, M., Camargo, S. J., Scoccimarro, E., Murakami, H., Wang, H., Ballinger, A., Kumar, A., Shaevitz, D. A., Jonas, J. A., and Oouchi, K.: Tracking scheme dependence of simulated tropical cyclone response to idealized climate simulations, Journal of Climate, 27, 9197 – 9213, https://doi.org/10.1175/JCLI-D-14-00200.1, 2014.

Johnson, S. J., Stockdale, T. N., Ferranti, L., Balmaseda, M. A., Molteni, F., Magnusson, L., Tietsche, S., Decremer, D., Weisheimer, A., Balsamo, G., Keeley, S. P. E., Mogensen, K., Zuo, H., and Monge-Sanz, B. M.: SEAS5: the new ECMWF seasonal forecast system, Geoscientific Model Development, 12, 1087–1117, https://doi.org/10.5194/gmd-12-1087-2019, publisher: Copernicus GmbH, 2019.

Kaplan, J. and DeMaria, M.: Large-scale characteristics of rapidly intensifying tropical cyclones in the North Atlantic basin, Wea. Forecasting, 18, 1093–1108, 2003.

Kleppek, S., Muccione, V., Raible, C. C., Bresch, D. N., Koellner-Heck, P., and Stocker, T. F.: Tropical cyclones in ERA-40: A detection and tracking method, Geophysical Research Letters, 35, n/a–n/a, https://doi.org/10.1029/2008GL033880, 2008.

Klotzbach, P., Blake, E., Camp, J., Caron, L.-P., Chan, J. C. L., Kang, N.-Y., Kuleshov, Y., Lee, S.-M., Murakami, H., Saunders, M., Takaya, Y., Vitart, F., and Zhan, R.: Seasonal Tropical Cyclone Forecasting, Tropical Cyclone Research and Review, 8, 134–149, https://doi.org/https://doi.org/10.1016/j.tcrr.2019.10.003, 2019.

Klotzbach, P. J.: Recent developments in statistical prediction of seasonal Atlantic basin tropical cyclone activity, Tellus A: Dynamic Meteorology and Oceanography, 59, 511–518, https://doi.org/10.1111/j.1600-0870.2007.00239.x, 2007.

Klotzbach, P. J. and Gray, W. M.: Updated 6–11-month prediction of Atlantic basin seasonal hurricane activity, Weather and Forecasting, 19, 917 – 934, https://doi.org/10.1175/1520-0434(2004)019<0917:UMPOAB>2.0.CO;2, 2004.

Knapp, K. R., Kruk, M. C., Levinson, D. H., Diamond, H. J., and Neumann, C. J.: The International Best Track Archive for Climate Stewardship (IBTrACS), Bulletin of the American Meteorological Society, 91, 363–376, https://doi.org/10.1175/2009BAMS2755.1, publisher: American Meteorological Society, 2010.

Knutson, T. R., Sirutis, J. J., Garner, S. T., Held, I. M., and Tuleya, R. E.: Simulation of the recent multidecadal increase of atlantic hurricane activity using an 18-km-grid regional model, Bulletin of the American Meteorological Society, 88, 1549–1565, https://doi.org/10.1175/BAMS-88-10-1549, 2007.

Krueger, A. F.: The weather and circulation of October 1954, Monthly Weather Review, pp. 296–300, 1954.

Landsea, C. W. and Franklin, J. L.: Atlantic Hurricane Database Uncertainty and Presentation of a New Database Format, Monthly Weather Review, 141, 3576–3592, https://doi.org/10.1175/MWR-D-12-00254.1, 2013.

Li, W., Wang, Z., Zhang, G., Peng, M. S., Benjamin, S. G., and Zhao, M.: Subseasonal variability of Rossby wave breaking and impacts on tropical cyclones during the North Atlantic warm season, Journal of Climate, 31, 9679–9695, https://doi.org/10.1175/JCLI-D-17-0880.1, 2018.

MacLachlan, C., Arribas, A., Peterson, K. A., Maidens, A., Fereday, D., Scaife, A. A., Gordon, M., Vellinga, M., Williams, A., Comer, R. E., Camp, J., Xavier, P., and Madec, G.: Global Seasonal forecast system version 5 (GloSea5): a high-resolution seasonal forecast system, Quarterly Journal of the Royal Meteorological Society, 141, 1072–1084, https://doi.org/10.1002/qj.2396, 2015.

Manabe, S., Holloway, J. L., and Stone, H. M.: Tropical circulation in a time-integration of a global model of the atmosphere, Journal of Atmospheric Sciences, 27, 580 – 613, https://doi.org/10.1175/1520-0469(1970)027<0580:TCIATI>2.0.CO;2, 1970.

McTaggart-Cowan, R., Galarneau, T. J., Bosart, L. F., Moore, R. W., and Martius, O.: A Global Climatology of Baroclinically Influenced Tropical Cyclogenesis, Monthly Weather Review, 141, 1963–1989, https://doi.org/10.1175/MWR-D-12-00186.1, 2013.

McTaggart-Cowan, R., Davies, E. L., Fairman, J. G., Galarneau, T. J., and Schultz, D. M.: Revisiting the 26.5°C sea surface temperature threshold for tropical cyclone development, Bulletin of the American Meteorological Society, 96, 1929 – 1943, https://doi.org/10.1175/BAMS-D-13-00254.1, 2015.

Mellor, G. L. and Yamada, T.: Development of a turbulence closure model for geophysical fluid problems, Reviews of Geophysics, 20, 851–875, https://doi.org/10.1029/RG020i004p00851, 1982.

Mlawer, E. J., Taubman, S. J., Brown, P. D., Iacono, M. J., and Clough, S. A.: Radiative transfer for inhomogeneous atmospheres: RRTM, a validated correlated-k model for the longwave, Journal of Geophysical Research: Atmospheres, 102, 16 663–16 682, https://doi.org/10.1029/97JD00237, 1997.

Montgomery, M. T. and Smith, R. K.: Paradigms for tropical cyclone intensification, Australian Meteorological and Oceanographic Journal, pp. 37–66, 2014.

Montgomery, M. T. and Smith, R. K.: Recent Developments in the Fluid Dynamics of Tropical Cyclones, Annual Review of Fluid Mechanics, 49, 541–574, https://doi.org/10.1146/annurev-fluid-010816-060022, _eprint: https://doi.org/10.1146/annurev-fluid-010816-060022, 2017.

Murakami, H., Vecchi, G. A., Underwood, S., Delworth, T. L., Wittenberg, A. T., Anderson, W. G., Chen, J.-H., Gudgel, R. G., Harris, L. M., Lin, S.-J., and Zeng, F.: Simulation and prediction of category 4 and 5 hurricanes in the high-resolution GFDL HiFLOR coupled climate model, Journal of Climate, 28, 9058 – 9079, https://doi.org/10.1175/JCLI-D-15-0216.1, 2015.

Nicholls, N.: A possible method for predicting seasonal tropical cyclone activity in the Australian region, Monthly Weather Review, 107, 1221–1224, https://doi.org/10.1175/1520-0493(1979)107<1221:APMFPS>2.0.CO;2, 1979.

Okubo, A.: Horizontal dispersion of floatable particles in the vicinity of velocity singularities such as convergences, Deep Sea Research and Oceanographic Abstracts, 17, 445–454, https://doi.org/10.1016/0011-7471(70)90059-8, 1970.

Ooyama, K.: Numerical Simulation of the Life Cycle of Tropical Cyclones, Journal of Atmospheric Sciences, 26, 3 – 40, https://doi.org/10.1175/1520-0469(1969)026<0003:NSOTLC>2.0.CO;2, 1969.

Palmen, E.: On the formation and structure of tropical hurricanes, Geophysica, 3, 26–38, 1948.

Palmén, E.: Vertical Circulation and Release of Kinetic Energy during the Development of Hurricane Hazel into an Extratropical Storm, Tellus, 10, 1–13, https://doi.org/10.3402/tellusa.v10i1.9222, 1958.

Papin, P. P., Bosart, L. F., and Torn, R. D.: A feature-based approach to classifying summertime potential vorticity streamers linked to Rossby wave breaking in the North Atlantic basin, Journal of Climate, 33, 5953–5969, https://doi.org/10.1175/JCLI-D-19-0812.1, 2020.

Pasch, R. J., Avila, L. A., and Jiing, J.-G.: Atlantic tropical systems of 1994 and 1995: A comparison of a quiet season to a near-record-breaking one, Monthly Weather Review, 126, 1106–1123, https://doi.org/10.1175/1520-0493(1998)126<1106:ATSOAA>2.0.CO;2, 1998.

Patricola, C. M., Saravanan, R., and Chang, P.: The impact of the El Niño–Southern Oscillation and Atlantic Meridional Mode on seasonal atlantic tropical cyclone activity, Journal of Climate, 27, 5311–5328, https://doi.org/10.1175/JCLI-D-13-00687.1, 2014.

Persing, J., Montgomery, M. T., McWilliams, J. C., and Smith, R. K.: Asymmetric and axisymmetric dynamics of tropical cyclones, Atmospheric Chemistry and Physics, 13, 12 299–12 341, https://doi.org/10.5194/acp-13-12299-2013, 2013.

Pielke Jr., R. A., Gratz, J., Landsea, C. W., Collins, D., Saunders, M. A., and Musulin, R.: Normalized hurricane damage in the United States: 1900–2005, Nat Hazards Rev, 9, 29–42, https://doi.org/10.1061/(ASCE)1527-6988(2008)9:1(29), 2008.

Postel, G. A. and Hitchman, M. H.: A Climatology of Rossby Wave Breaking along the Subtropical Tropopause, Journal of the Atmospheric Sciences, 56, 359–373, https://doi.org/10.1175/1520-0469(1999)056<0359:ACORWB>2.0.CO;2, 1999.

Prill, F., Reinert, D., Rieger, D., Zängl, G., Schröter, J., Förstner, J., Werchner, S., Weimer, M., Ruhnke, R., and Vogel, B.: ICON model tutorial April 2019, 2019.

Raschendorfer, M.: The new turbulence parameterization of LM, COSMO News Letter No. 1, pp. 89–97, 2001.

Riemer, M. and Laliberté, F.: Secondary Circulation of Tropical Cyclones in Vertical Wind Shear: Lagrangian Diagnostic and Pathways of Environmental Interaction, Journal of the Atmospheric Sciences, 72, 3517–3536, https://doi.org/10.1175/JAS-D-14-0350.1, 2015.

Riemer, M., Montgomery, M. T., and Nicholls, M. E.: A new paradigm for intensity modification of tropical cyclones: thermodynamic impact of vertical wind shear on the inflow layer, Atmospheric Chemistry and Physics, 10, 3163–3188, https://doi.org/10.5194/acp-10-3163-2010, publisher: Copernicus GmbH, 2010.

Roberts, M. J., Camp, J., Seddon, J., Vidale, P. L., Hodges, K., Vanniere, B., Mecking, J., Haarsma, R., Bellucci, A., Scoccimarro, E., Caron, L.-P., Chauvin, F., Terray, L., Valcke, S., Moine, M.-P., Putrasahan, D., Roberts, C., Senan, R., Zarzycki, C., and Ullrich, P.: Impact of Model Resolution on Tropical Cyclone Simulation Using the HighResMIP–PRIMAVERA Multimodel Ensemble, Journal of Climate, 33, 2557 – 2583, https://doi.org/10.1175/JCLI-D-19-0639.1, 2020.

Rossby, C.-G. and collaborators: Relation between variations in the intensity of the zonal circulation of the atmosphere and the displacements of the semi-permanent centers of action, Journal of Marine Research, 2, 38–55, https://doi.org/10.1357/002224039806649023, 1939.

Rotunno, R. and Emanuel, K. A.: An air–sea interaction theory for tropical cyclones. Part II: Evolutionary study using a nonhydrostatic axisymmetric numerical model, Journal of the Atmospheric Sciences, 44, 542–561, https://doi.org/10.1175/1520-0469(1987)044<0542:AAITFT>2.0.CO;2, 1987.

Saffir, H. S.: Hurricane wind and storm surge, The Military Engineer, 65, 4–5, 1973.

Satoh, M., Matsuno, T., Tomita, H., Miura, H., Nasuno, T., and Iga, S.: Nonhydrostatic icosahedral atmospheric model (NICAM) for global cloud resolving simulations, J. Comput. Phys., 227, 3486 – 3514, https://doi.org/http://dx.doi.org/10.1016/j.jcp.2007.02.006, 2008.

Satoh, M., Tomita, H., Yashiro, H., Miura, H., Kodama, C., Seiki, T., Noda, A. T., Yamada, Y., Goto, D., Sawada, M., Miyoshi, T., Niwa, Y., Hara, M., Ohno, T., Iga, S.-i., Arakawa, T., Inoue, T., and Kubokawa, H.: The Non-hydrostatic Icosahedral Atmospheric Model: description and development, Prog Earth Planet Sci, 1, 18, https://doi.org/10.1186/s40645-014-0018-1, 2014.

Saunders, M. A. and Lea, A. S.: Seasonal prediction of hurricane activity reaching the coast of the United States, Nature, 434, 1005–1008, https://doi.org/10.1038/nature03454, 2005.

Scott, R. K. and Cammas, J.-P.: Wave Breaking and Mixing at the Subtropical Tropopause, Journal of the Atmospheric Sciences, 59, 2347–2361, https://doi.org/10.1175/1520-0469(2002)059<2347:WBAMAT>2.0.CO;2, 2002.

Shapiro, L. J.: The relationship of the Quasi-biennial Oscillation to Atlantic tropical storm activity, Monthly Weather Review, 117, 1545–1552, https://doi.org/10.1175/1520-0493(1989)117<1545:TROTQB>2.0.CO;2, 1989.

Smith, R. K. and Montgomery, M. T.: Toward clarity on understanding tropical cyclone intensification, Journal of the Atmospheric Sciences, 72, 3020–3031, https://doi.org/10.1175/JAS-D-15-0017.1, 2015.

Sprenger, M., Fragkoulidis, G., Binder, H., Croci-Maspoli, M., Graf, P., Grams, C. M., Knippertz, P., Madonna, E., Schemm, S., Škerlak, B., and Wernli, H.: Global Climatologies of Eulerian and Lagrangian Flow Features based on ERA-Interim, Bulletin of the American Meteorological Society, 98, 1739–1748, https://doi.org/10.1175/BAMS-D-15-00299.1, _eprint: https://journals.ametsoc.org/bams/article-pdf/98/8/1739/3748210/bams-d-15-00299_1.pdf, 2017.

Stern, D. P. and Nolan, D. S.: On the Height of the Warm Core in Tropical Cyclones, Journal of the Atmospheric Sciences, 69, 1657–1680, https://doi.org/10.1175/JAS-D-11-010.1, 2012.

Strachan, J., Vidale, P. L., Hodges, K., Roberts, M., and Demory, M.-E.: Investigating Global Tropical Cyclone Activity with a Hierarchy of AGCMs: The Role of Model Resolution, Journal of Climate, 26, 133 – 152, https://doi.org/10.1175/JCLI-D-12-00012.1, place: Boston MA, USA Publisher: American Meteorological Society, 2013.

Takemura, K. and Mukougawa, H.: Tropical Cyclogenesis Triggered by Rossby Wave Breaking over the Western North Pacific, Sola, advpub, 2021–029, https://doi.org/10.2151/sola.2021-029, 2021.

Tang, B. and Emanuel, K.: Midlevel Ventilation's Constraint on Tropical Cyclone Intensity, Journal of the Atmospheric Sciences, 67, 1817–1830, https://doi.org/10.1175/2010JAS3318.1, 2010.

Tang, B. and Emanuel, K.: A Ventilation Index for Tropical Cyclones, Bulletin of the American Meteorological Society, 93, 1901–1912, https://doi.org/10.1175/BAMS-D-11-00165.1, 2012.

Thorncroft, C. and Pytharoulis, I.: A dynamical approach to seasonal prediction of Atlantic tropical cyclone activity, Weather and Forecasting, 16, 725 – 734, https://doi.org/10.1175/1520-0434(2002)016<0725:ADATSP>2.0.CO;2, 2001.

Tory, K. J., Dare, R. A., Davidson, N. E., McBride, J. L., and Chand, S. S.: The importance of low-deformation vorticity in tropical cyclone formation, Atmospheric Chemistry and Physics, 13, 2115–2132, https://doi.org/10.5194/acp-13-2115-2013, 2013.

Tsutsui, J.-i. and Kasahara, A.: Simulated tropical cyclones using the National Center for Atmospheric Research community climate model, Journal of Geophysical Research: Atmospheres, 101, 15 013–15 032, https://doi.org/10.1029/95JD03774, 1996.

Ullrich, P. A. and Zarzycki, C. M.: TempestExtremes: a framework for scale-insensitive pointwise feature tracking on unstructured grids, Geoscientific Model Development, 10, 1069–1090, https://doi.org/10.5194/gmd-10-1069-2017, publisher: Copernicus GmbH, 2017.

Vecchi, G. A., Delworth, T., Gudgel, R., Kapnick, S., Rosati, A., Wittenberg, A. T., Zeng, F., Anderson, W., Balaji, V., Dixon, K., Jia, L., Kim, H.-S., Krishnamurthy, L., Msadek, R., Stern, W. F., Underwood, S. D., Villarini, G., Yang, X., and Zhang, S.: On the seasonal forecasting of regional tropical cyclone activity, Journal of Climate, 27, 7994–8016, https://doi.org/10.1175/JCLI-D-14-00158.1, 2014.

Vitart, F., Huddleston, M. R., Déqué, M., Peake, D., Palmer, T. N., Stockdale, T. N., Davey, M. K., Ineson, S., and Weisheimer, A.: Dynamically-based seasonal forecasts of Atlantic tropical storm activity issued in June by EUROSIP, Geophysical Research Letters, 34, https://doi.org/https://doi.org/10.1029/2007GL030740, _eprint: https://agupubs.onlinelibrary.wiley.com/doi/pdf/10.1029/2007GL030740, 2007.

Walsh, K., Lavender, S., Scoccimarro, E., and Murakami, H.: Resolution dependence of tropical cyclone formation in CMIP3 and finer resolution models, Climate Dynamics, 40, 585–599, https://doi.org/10.1007/s00382-012-1298-z, 2012.

Walsh, K. J. E., Fiorino, M., Landsea, C. W., and McInnes, K. L.: Objectively Determined Resolution-Dependent Threshold Criteria for the Detection of Tropical Cyclones in Climate Models and Reanalyses, Journal of Climate, 20, 2307–2314, https://doi.org/10.1175/JCLI4074.1, 2007.

Wang, X. and Jiang, H.: A 13-Year Global Climatology of Tropical Cyclone Warm-Core Structures from AIRS Data, Monthly Weather Review, 147, 773–790, https://doi.org/10.1175/MWR-D-18-0276.1, 2019.

Wang, Z., Li, W., Peng, M. S., Jiang, X., McTaggart-Cowan, R., and Davis, C. A.: Predictive Skill and Predictability of North Atlantic Tropical Cyclogenesis in Different Synoptic Flow Regimes, Journal of the Atmospheric Sciences, 75, 361–378, https://doi.org/10.1175/JAS-D-17-0094.1, 2018.

Weiss, J.: The dynamics of enstrophy transfer in two-dimensional hydrodynamics, Physica D: Nonlinear Phenomena, 48, 273–294, https://doi.org/10.1016/0167-2789(91)90088-Q, 1991.

Wernli, H. and Sprenger, M.: Identification and ERA-15 Climatology of Potential Vorticity Streamers and Cutoffs near the Extratropical Tropopause, Journal of the Atmospheric Sciences, 64, 1569–1586, https://doi.org/10.1175/JAS3912.1, 2007.

Willoughby, H. M.: The Dynamics of the Tropical Cyclone Core, Aust. Meteorol. Mag., 36, 183–191, 1988.

Wu, L., Su, H., Fovell, R. G., Wang, B., Shen, J. T., Kahn, B. H., Hristova-Veleva, S. M., Lambrigtsen, B. H., Fetzer, E. J., and Jiang, J. H.: Relationship of environmental relative humidity with North Atlantic tropical cyclone intensity and intensification rate, Geophysical Research Letters, 39, https://doi.org/10.1029/2012GL053546, 2012.

Yang, W., Hsieh, T.-L., and Vecchi, G. A.: Hurricane annual cycle controlled by both seeds and genesis probability, Proceedings of the National Academy of Sciences, 118, e2108397 118, https://doi.org/10.1073/pnas.2108397118, 2021.

Zarzycki, C. M. and Ullrich, P. A.: Assessing sensitivities in algorithmic detection of tropical cyclones in climate data, Geophysical Research Letters, 44, 1141–1149, https://doi.org/10.1002/2016GL071606, 2017.

Zhang, G., Wang, Z., Dunkerton, T. J., Peng, M. S., and Magnusdottir, G.: Extratropical Impacts on Atlantic Tropical Cyclone Activity, Journal of the Atmospheric Sciences, 73, 1401–1418, https://doi.org/10.1175/JAS-D-15-0154.1, publisher: American Meteorological Society, 2016.

Zhang, G., Wang, Z., Peng, M. S., and Magnusdottir, G.: Characteristics and impacts of extratropical Rossby wave breaking during the Atlantic hurricane season, Journal of Climate, 30, 2363–2379, https://doi.org/10.1175/JCLI-D-16-0425.1, 2017.

Zhang, G., Murakami, H., Gudgel, R., and Yang, X.: Dynamical Seasonal Prediction of Tropical Cyclone Activity: Robust Assessment of Prediction Skill and Predictability, Geophysical Research Letters, 46, 5506–5515, https://doi.org/https://doi.org/10.1029/2019GL082529, _eprint: https://agupubs.onlinelibrary.wiley.com/doi/pdf/10.1029/2019GL082529, 2019.

Zhao, M., Held, I. M., Lin, S.-J., and Vecchi, G. A.: Simulations of global hurricane climatology, Iinterannual variability, and response to global warming using a 50-km resolution GCM, Journal of Climate, 22, 6653 – 6678, https://doi.org/10.1175/2009JCLI3049.1, 2009.

Zängl, G., Reinert, D., Rípodas, P., and Baldauf, M.: The ICON (ICOsahedral Non-hydrostatic) modelling framework of DWD and MPI-M: Description of the non-hydrostatic dynamical core, Quarterly Journal of the Royal Meteorological Society, 141, 563–579, https://doi.org/10.1002/qj.2378, publisher: John Wiley & Sons, Ltd, 2015.